CORA Cork Open Research Archive
Cartlann Taighde Oscailte Chorcaí

Title	Surface dynamics in III-V epitaxy and its device implications
Authors	Ozcan Atar, Ayse
Publication date	2024
Original Citation	Ozcan Atar, A. 2024. Surface dynamics in III-V epitaxy and its device implications. PhD Thesis, University College Cork.
Type of publication	Doctoral thesis
Rights	© 2024, Ayse Ozcan Atar. - https://creativecommons.org/licenses/by-nc-sa/4.0/
Download date	2026-11-04 09:01:38
Item downloaded from	https://hdl.handle.net/10468/16428

UCC
University College Cork, Ireland
Coláiste na hOllscoile Corcaigh

Surface Dynamics in III-V Epitaxy and Its Device Implications

Ayşe Özcan Atar



Thesis submitted in partial fulfilment of the requirements
of the degree of Doctor of Philosophy

at the
School of Physics,
University College Cork,
National University of Ireland

Supervisor: Emanuele Pelucchi
Co-supervisor: Gediminas Juska
Head of Department: Prof. Paul Callanan

May 2024

Contents

List of Figures iii

List of Tables viii

Declaration of Authorship ix

Acknowledgements x

List of Acronyms xiii

List of Publications xv

1 Introduction 1
- 1.1 Introduction . . . 1
- 1.2 Thesis outline . . . 4

2 Background 5
- 2.1 Overview of the MOVPE Growth Process . . . 5
- 2.2 Doping in III-Vs . . . 12
  - 2.2.1 Zn doping of InP . . . 13
- 2.3 Diffusion of Dopants . . . 15
  - 2.3.1 Diffusion Mechanisms without the Involvement of Point Defects . . . 16
  - 2.3.2 Diffusion Mechanisms Involving Point Defects . . . 17
  - 2.3.3 Literature Overview of the Zn Diffusion Mechanism in InP . . . 20
- 2.4 Surfactants and Surfactant Dopants in MOVPE . . . 22

3 Material Growth and Characterization Methodology 23
- 3.1 Our MOVPE Facilities and Material Growth . . . 23
- 3.2 Characterization Tools . . . 27
  - 3.2.1 Dopant Characterization . . . 27
    - 3.2.1.1 Secondary-Ion Mass Spectrometry (SIMS) . . . 27
    - 3.2.1.2 Capacitance-Voltage Measurement . . . 30
    - 3.2.1.3 Electrochemical Capacitance-Voltage Profiling . . . 32
    - 3.2.1.4 Scanning Spreading Resistance Microscopy (SSRM) . . . 33
  - 3.2.2 Material Characterization . . . 34
    - 3.2.2.1 Atomic Force Microscopy (AFM) . . . 34
    - 3.2.2.2 High-Resolution X-ray Diffraction (HRXRD) . . . 35
  - 3.2.3 Optical Characterization . . . 36
    - 3.2.3.1 Micro Photoluminance (μPL) Measurement . . . 36

4 Zn Concentration Profile of III-V Materials **37**
4.1 Asymmetric Zn concentration profile in III-V phosphide and arsenide layers . . 37
4.1.1 Switching from AsH_3 to PH_3 43
4.2 Electrical characterization of Zn as a dopant 44
4.3 Suppressing the Zn forward-diffusion 47
4.4 Zn Back Diffusion in Different Misoriented Substrates 49
4.5 Photoluminescence of the Doped Layers 51
4.6 Discussion and Conclusion 54

5 Theory of Zn Surfactant Behaviour **58**
5.1 Theoretical model: Coupled equations 58
5.2 Numerical modelling 60
5.2.1 Finite difference methods 60
5.2.2 Settiong up the boundary conditions 67
5.2.3 Two-diffusion constants 71
5.3 Discussion and Conclusion 73

6 Suppressing Oxygen Incorporation in Aluminium Containing Alloys **74**
6.1 Introduction 74
6.1.1 Removing Oxygen in AlInAs with Sb 76
6.1.2 Oxygen Reduction in AlGaAs with Sb 78
6.2 Summary and Conclusion 81

7 Conclusion and Future Work **83**
7.1 Zn surfactant effects 83
7.2 Oxygen Incorporation in Aluminum Containing Alloys 86

Bibliography **88**

List of Figures

2.1 Schematic representation of fundamental steps of a typical MOVPE process [45] 6
2.2 Some of the probable reactions steps during MOVPE growth of GaAs using TMGa and AsH_3 in an H_2 ambient environment. Adapted from Ref. 45 7
2.3 Schematic representation of the three distinct growth regimes depending on the temperature 10
2.4 Schematics diagram of three fundamental growth modes of MOVPE, in the units of coverage vs monolayer (ML). Adapted from Ref. 52 11
2.5 Young's equation describes the wetting angle (ϕ) of a liquid nucleus on a substrate in terms of surface energies. The surface energy of the substrate (γ_B), the surface energy of the film material (γ_A), and the interface energy between the film and the substrate (γ^*) have the following relationship $\gamma_B = \gamma^* + \gamma_A \cos\phi$. 11
2.6 Schematic illustration of two dimensional zinc-blend lattice consisting of group-III and group-V elements. Acceptors like Zn and C have a deficit electron and Si and Te has an excess electron. 13
2.7 Diffusion mechanisms without the involvement of point defects. a) direct interstitial mechanism b) direct exchange (b-left) and ring diffusion (b-right) mechanisms. 17
2.8 Vacancy exchange mechanism. White square depicts the vacancy, black and green circles depict tracer and matrix atoms, respectively 18
2.9 Interstitialcy mechanism of diffusion. A substitutional atom exchanges with a self-interstitial (middle), moving into an interstitial site (right). 18
2.10 Divacancy mechanism of diffusion. A substitutional impurity switch with a divacancy (a vacancy complex formed by combination of two vacancies). 19
2.11 Schematic representation of interstitial-substitutional exchange mechanisms of impurity atom diffusion. a) Frank-Turnbull mechanism b) kick-out mechanism . 20

3.1 Schematic diagram of the major components of the MOVPE system. Metalorganics and hydrides are carried by purified N_2 toward either to the reactor (via run line) or to the exhaust (via vent line). A manifold injector flange, equipped with multiple pneumatic valves, facilitates the introduction of sources, purge, and rotation fluxes into the reactor. A (dry) pump regulates the reactor's operational pressure. 24
3.2 Schematic of the planetary motion of three substrates on a multiwafer MOVPE graphite reactor. Each satellite, as well as the main holder, rotates around the centre, ensuring uniformity of thickness, composition, and doping concentration. 25
3.3 Schematic diagram of the key parts of a metalorganic (MO) bubbler. During the growth the MO stream is either directed to the run line or the reactor chamber. Gas flows are controlled by electronic mass flow controllers (MFCs) and pressure controllers (PCs). 26
3.4 A schematic representation of sequence diagram of the Secondary Ion Mass Spectrometry (SIMS) technique (adapted from [100]) 28

3.5 A schematic illustration of a reverse-biased Schottky diode. 30
3.6 a) Schematic of of InP:Si/InP/InP:Zn layers grown on a nominally perfectly oriented Zn doped substrate for C-V purposes b) Optical microscope image of C-V measurement diodes. The bottom right device has a 1 mm diameter and used for C-V measurements. 32
3.7 A schematic layout of a Scanning Spreading Resistance Microscopy (SSRM) setup 34

4.1 Measured SIMS profile of Zn concentration of MOVPE grown InP epitaxial layers. The substrate choices for these samples were nominally perfectly oriented Fe doped InP wafers. a) Total Zn concentration levels measured with the Zn(lowV) method of the InP(200 nm)/InP:Zn(200 nm)/InP(2 μm) (from bottom to top) layers. The inset figure shows SIMS measurement of the same sample with a faster scan, which allows a better resolution of the low concentration. b) Total Zn concentration levels measured with the Zn(lowV) method of the InP(200 nm)/InP:Zn(200 nm)/InP(500 nm) layers. c) Total Zn concentration levels measured with the Zn(lowV) method of the InP(200 nm)/InP:Zn(500 nm)/InP(500 nm) layers. The Zn flow during the doped layer growth is 10 times lower than the samples in (a) and (b). For (a), (b) and (c), zero nm on the x axis in the depth profiles is the final sample surface. The oxygen peak marks the sample substrate-to-epitaxial layer interface. The dotted lines (A-B) indicates the nominal boundaries between the Zn doped and nominally undoped (NUD) layers. The peak in the Zn profile at point A, at the interface between the intentionally doped/not doped interface is a real effect. d) A zoomed-in comparison of the peak concentration and shape of the samples in (a) and (b). The x-axis is shifted so the samples are aligned at the interface. 40
4.2 Comparison of the three different Zn methodologies applied on the sample shown in Figure 4.1a. The total Zn profile measured with Zn(lowV) (left x-axis) and the conventional Zn(Class) methodology (left x-axis). Zn(ULIE) measures the ZnP_3 complex ion (right x-axis). 41
4.3 a) Total Zn concentration levels measured with the Zn(lowV) method of the GaAs(200 nm)/GaAs:Zn(200 nm)/GaAs(500 nm) (from bottom to top) layers. b) Total Zn concentration levels measured with the Zn(lowV) method of the InGaAs(200 nm)/InGaAs:Zn(200 nm)/InGaAs(500 nm) layers. 42
4.4 Differences in post growth tailing when switching from PH_3 to AsH_3. a) Measured SIMS profile of Zn concentration levels of InP(200 nm)/ InP:Zn(200nm)/ InGaAs(500 nm) (from bottom to top) epitaxial layers grown on nominally perfectly oriented InP wafer b) Comparing the Zn concentration profile of samples (a) and Figure 4.3b where the doped layer is InP or InGaAs. The Zn forward diffusion length is slightly longer (approximately 150 nm) when the Zn-doped layer is InP-based. 43
4.5 Measured SIMS profile of Zn concentration levels of a) InP (200nm)/InP:Zn (200 nm)/AlInAs (500 nm) epitaxial layers grown on nominally perfectly oriented InP wafer. b) InGaP (1 μm)/InGaP:Zn (200 nm)/InGaP (200 nm) grown on 0.2° misoriented towards (111)A crystallographic plane GaAs wafer. 44

4.6 Electrical characterization of InP:Si/InP/InP:Zn layers grown on a nominally perfectly oriented Zn doped substrate. a) SSRM: 2D cross sectional resistance map obtained from a cleaved cross sectional sample surface b) Extracted resistance value of averaged lines through scan direction. The dotted lines indicate the nominal boundaries between the Zn doped, NUD and Si doped InP layers. c) Schematic of epi-structure d) Schematic of SSRM measurement setup e) CV measurements: The extracted $1/C^2$ curve from the device, with curvature indicating non-uniform doping f) Mott-Schottky analysis of (e), yielding the doping profile. g) ECV depth profiling of the sample h) compendium of the different techniques. To be able to obtain a clear comparison, SSRM profile is rescaled from log(R) to $10^{1/R}$. X-axis of ECV depth profile is also reversed so that it is aligned with the CV curve. 45

4.7 Effect of growth interruption on the Zn tailing a) 5 minutes growth interruption with PH_3 overflow reduces the post growth tailing to around 250 nm, measured with a slow Zn(lowV) scan. b) 5 minutes growth interruption with PH_3 and TMSb overflow reduces the post growth tailing to around 100 nm measured with a slow Zn(lowV) scan. An InGaP marker layer was added to identify the first undoped to doped interface and the back diffusion region. A-B markers and red lines are used here as in Figure 4.1. c) Sb assisted AlInAs layer is immediately started (No growth interruption is applied) after the Zn doped InP layer. d) Same structure and growth protocol with sample (c) with half Sb flow. Zn doping profile is almost identical, Sb incorporation is reduced ≈5 times of that in (c) 48

4.8 Effect of substrate misorientation on the background doping. InP/InP:Zn/InP layers grown on a a) 0.4° misoriented towards (111)A crystallographic plane, b) 0.4° misoriented towards (111)B crystallographic plane and c) nominally perfectly oriented d) comparison of all the samples, with the InGaP layer producing a Ga marker facilitating the graphs' alignment. A-B markers and red lines are used here as in Figure 4.1 to identify the InP Zn-doped layers. 50

4.9 Low-temperature PL. (a)-(c) Changes in PL as a result of Zn doping and capping. NUD InP (black) spectrum taken at 10 W/cm^2, all others 1 kW/cm^2. (a) NUD InP (black) exhibits a strong free-excitonic (FX) peak only. This is suppressed in Zn-doped InP (green), which has a spectrum dominated by deep-donor to acceptor (DD-A^0) recombination. (b) After capping of InP:Zn by 200 nm of NUD InP (blue) the DD-A^0 emission is absent, and the spectrum is dominated by e/D-A^0 and DDX emission. (c) Further capping tends to recover the free-excitonic emission, but the e/D- A^0 and DDX PL remain. (d) The excitation intensity dependence of the DD- A^0 emission in an uncapped InP:Zn sample. A blueshift of 65 meV/decade is observed. (e) and (f): Effect of substrate misorientation on the PL. (e) In capped InP:Zn, the intensity is significantly higher for 0.4° misorientation towards (111)B, compared to nominal perfect orientation (p.o.), and less for 0.4° misorientation towards (111)A (250 W/cm^2). (f) In NUD InP no significant differences are observed (10 W/cm^2). r.u.: relative units. 52

4.10 An example PL at 14 K. This sample consists of 200 nm Zn-doping followed by a 2 μm cap. Inset: LO-phonon replicas of the shallow acceptor band. 53

4.11 Effect of substrate misorientation on the PL for a) 200 nm Zn:InP layer grown on (100) perfectly oriented (po) and (100) 0.4° misoriented towards (111)B (4B) samples (15 K, 10 W/cm^2), b) samples shown in Figure 4.8 (14 K, 250 W/cm^2), c) samples (a) measured at 14 K taken with 1 kW/cm^2 and d) samples (a) measured at room temperature (295 K, 3 kW/cm^2) A similar difference in intensity is seen at low temperature (14 K, 1 kW/cm^2) and at room temperature (295 K, 3 kW/cm^2). 54

5.1 Illustration of the finite difference method. a) The mesh is the set of locations where the discrete solution is computed. Each n-index corresponds to a time step and each i-index corresponds to position (depth) into the material. b) The evolution of the concentration function in time. 61
5.2 Computational molecules used in different finite difference methods. a) Forward time- Centred Space b) Backward time- Centred Space and c) Crank-Nicholson. The n-index represents the discretised time points and i-index corresponds to the discretised spatial points. 63
5.3 Modelled Zn concentration profile of InP epitaxial layers compared with measured data. a) Modelling of the measured sample in Figure 4.1a using a single diffusion constant model. The model agrees well with the measured Zn profile. Modelling of Zn profile grown on b) a substrate with 0.4° misoriented towards (111)A crystallographic plane (Figure 4.8a) and c) a substrate with 0.4° misoriented towards (111)B crystallographic plane (Fig 4.8c) by using a single diffusion constant model. d) Modelling of Zn profile grown on nominally perfectly oriented substrate (Fig. 4.8b) by using a double diffusion model with the diffusion constant extracted from (b) and (c). 70
5.4 Simulating the sample in Figure 5.3a by changing the fitting parameters. The details of the changed parameters for a), b), c), d), e) and f) are given in the Supplementary Table 5.1. 72

6.1 Effect of Sb addition on the oxygen incorporation of AlInAs layers (same samples showed in Figure 4.7). Sb assisted AlInAs layer is immediately started after the Zn doped InP layer. a) No oxygen trace is recorded in the layers where Sb is present. b) Same structure and growth protocol with sample (a) with lower Sb flow. The oxygen peak marks the sample substrate-to-epitaxial layer interface. The dotted lines indicates the nominal boundaries between the layers. 77
6.2 SIMS analysis showing the Al and In percentage of AlInAs layers of samples a) in Figure 6.1a and b) in Figure 6.1b. 78
6.3 SIMS depth profiling of AlGaAs:Sb/AlGaAs/GaAs layers. To facilitate the depth profiling a 5 nm GaAs has been grown between AlGaAs and AlGaAs:Sb layers. a) The layers are grown at 700°C thermocouple temperature. b) Same structure grown with same conditions as in (a) expect the temperature was increased to 750°C thermocouple. 79
6.4 AFM images showing the surface morphology of samples shown in a) Figure 6.3b, grown at 750°C, showing a step flow surface organization and b) Figure 6.3a, grown at 700°C, showing an hillock formation surface structure. 80
6.5 Cross-sectional AFM images of layers shown in Figure 6.3a. The sample is prepared by cleaving, and AFM probe is scanned over cleavage on $[1\bar{1}0]$ facet perpendicular across the epi-layers in peak-force mode in air at times 30 min, 60 min, 120 min and 20 hours post-cleaving. AlGaAs layers and AlGaAs:Sb layers exhibit different oxidation behaviors; notably, over time, the AlGaAs layer demonstrates a higher height and roughness compared to the AlGaAs:Sb layer. 81

6.6 Height line scans generated from the AFM images in Figure 6.5 at times 30 min, 60 min, 120 min and 20 hours post-cleaving. For each time step, the lines are extracted from averaged lines across the whole image. The dotted lines (A-B) denote the nominal boundaries between GaAs-AlGaAs and AlGaAs:Sb layers. X axes are shifted so that the layers coincide with each other. 82

List of Tables

5.1 The changed fitting parameters for the sample in Figure 4.1a while dt, dx and dC are kept constant. 71

6.1 Summary of the Al and In percentage as well as Sb and Oxygen incorporation of the samples in Figure 6.1 (and also Figure 6.2) 78
6.2 Summary of the Al and Ga percentage as well as Sb and Oxygen incorporation of the samples in Figure 6.3 for comparison. 79

Declaration

I, **Ayşe Özcan Atar**, hereby declare that, unless otherwise stated, this work is my own, and that it has not been submitted for another degree, either at University College Cork or elsewhere.

Ayşe Özcan Atar

Tyndall National Institute,

University College Cork,

May, 2024

Acknowledgements

I am deeply grateful for the support I received and recognize that much of what I achieved was made possible by the collective efforts of many.

First and foremost, I extend my deepest gratitude to my supervisor Dr. Emanuele Pelucchi, for accepting me on this PhD program, for his endless support and for being a good mentor and critic throughout. His constant and remarkable desire to understand the physics of everything has been a joy and motivation for me. Hopefully, I have picked up at least a tiny fraction of his profound knowledge over the years.

I would like to thank my former co-supervisor Dr. Agnieszka Gocalinska, for assisting me at the beginning of this study. Our fruitful conversations about science and life in general have been an inspiration. Thank you very much for your time and patience.

Dr. Pawel P. Michalowski deserves special recognition for his expertise in SIMS, which played a crucial role in the progress of this research. I am deeply grateful for the contribution of Prof. Dimitri D. Vvedensky during the development of the theoretical model regarding Zn surfactant behavior. I would like to thank John O'Hara, Mack Johnson, Adrianna Wojcik, Brendan Sheehan, Kevin Thomas and Enrica Mura for their assistance with various measurements throughout this study. Without their contributions, this study would not be comprehensive. I would like to thank Brian Corbett and Prof. Frank Peters for assisting this work from a device physics point of view.

A PhD has its ups and downs and things are always easier with people who went through the similar things. My friendship with other PhD students in Tyndall and also in PIADS was very valuable. Along with them, I thank all EPN Group members for the great time we have shared.

I thank my friends and family members all around the world for their comforting support despite the long distance. Indeed, they have contributed to this thesis with many different ways.

Lastly, I need to thank my husband, Fatih, for his love and kindness, for taking care of me and our daughter, especially when I was writing this thesis. Thank you very much for always having my back when things were difficult. Undoubtedly, I dedicate this thesis to my family- *my husband Fatih* and *my daughter Zeynep Sare*.

Cork, May 2024 *Ayşe*

This work is supported by Science Foundation Ireland under grants 18/EPSRC-CDT/3585 and 12/RC/2276_P2.

Abstract

Metalorganic vapour phase epitaxy (MOVPE) is a well-established, industry-compatible, compound semiconductor crystal growth technique, allowing for efficient and controllable material deposition. A wide range of semiconductor devices, both from III-V and nitrides families, are commonly fabricated for a broad range of applications in photonics, electronics and related fields, due to the reproducibility, scalability and overall excellent control over the growth process. Nevertheless, despite the technique's popularity, there persists a large number of unresolved issues (mostly related to growth process/dynamic understanding) effectively hindering some of potential developments of III-V devices.

A major unresolved technological issue, is the reported long range "leakage" of the dopant Zn into intrinsic layers during (and post) epitaxy, including the device processing steps. Zn is used as a typical p-type dopant for III-V materials and devices, but it is reportedly highly diffusive and historically very problematic. To bypass the Zn related problems, the large majority of InP based photonic devices, such as lasers and modulators, are fabricated with an n-i-p design, using p-type dopant at the top of the device. This approach essentially limits the design degree of freedom and stands in the way of the novel advanced stacked device architectures.

This work reevaluated the Zn doping issues with unprecedented and surprising findings on Zn dopant behavior. The secondary ion mass spectrometry (SIMS) experiments show that Zn (or its precursors) can behave as a surfactant; accumulating on the sample surface during the growth of intentional doping layer and gradually incorporating into the nominally undoped layers even after the Zn source is shut off. Experimental findings are modelled by combining the surfactant and diffusion behavior with good qualitative agreement. Also, we demonstrated that this phenomenology can be suppressed and controlled either by introducing growth interruption steps or, even more effectively, introducing a competing surfactant species (Sb or its precursors). Our results highlight the relevance of (often overlooked) multi-faceted surface processes during MOVPE epitaxy, and help the implementation of robust solutions for novel device designs, crucially enabling next-generation integrated III-V applications.

List of Acronyms

2D	two-dimensional
AFM	atomic force microscopy
BTCS	backward time-centered space
C-V	capacitance-voltage
DEZn	diethylzinc
ECV	electrochemical capacitance-voltage
ED	ethylenediamine
EDTA	ethylenediamine disodium
FTCS	forward time-centered space
FWHM	full-width-half-maximum
HRXRD	high-resolution X-ray diffraction
LEDs	light emitting diodes
MBE	molecular-beam epitaxy
MO	metal organic
MOVPE	metal organic vapour phase epitaxy
NUD	nominally undoped
PDE	partial differential equation
PL	photoluminescence
RSM	reciprocal space mapping
scr	space-charge region
SIMS	secondary ion mass spectrometry

SSRM scanning spreading resistance measurement

TMAl trimethylaluminum

TMGa trimethylgallium

TMIn trimethylindium

TMSn tetramethyltin

TMSb trimethylantimony

UHV ultra-high vacuum

ULIE ultra-low impact energies

List of Publications

Journal Publications

- **A. Ozcan-Atar**, A. Gocalinska, P. P. Michałowski, M. Johnson, J. O'Hara, B. Corbett, A. Wójcik, F. Peters, D. D. Vvedensky, A. Zangwill, G. Juska, and E. Pelucchi, "Why 'Zn diffusion' is not always diffusion: surface physics and a 40 year-old epitaxy problem", to be submitted
- **A. Ozcan-Atar**, J. O'Hara , L. Colavecchi and E. Pelucchi, "Suppressing oxygen incorporation in Aluminium containing alloys through surfactants" to be submitted

Conferences (poster/oral presentations)

- **A. Ozcan-Atar** (oral), A. Gocalinska, P. P. Michalowski, M. Johnson, J. O'Hara, B. Corbett, A. Wojcik, F. H. Peters, D. Vvedensky and E. Pelucchi, "Surprising Surfactant Properties of Zn in MOVPE Grown III-V Materials" International conference on Crystal growth and epitaxy ICCGE'20, Naples, Italy, Aug 2023
- **A. Ozcan-Atar** (oral), A. Gocalinska, P. P. Michalowski, M. Johnson, J. O'Hara, B. Corbett, A. Wojcik, F. H. Peters, D. Vvedensky and E. Pelucchi, "Surfactant Properties of Zn in MOVPE Grown III-V Materials and Surprising Doping Implications", Compound Semiconductor Week, CSW2023, Jeju, South Korea, June 2023
- **A. Ozcan-Atar** (poster), A. Gocalinska , P.P Michalowski, D. Vvedensky and E. Pelucchi, "Revealing the Zn Dopant Behaviour in MOVPE Grown InP Layers" International Conference on Metal Organic Vapor Phase Epitaxy-ICMOVPE XX, Stuttgart, Germany, July 2022

Contribution to Conference Talks

- S. Mukherjee (oral), J. O'Hara, **A. Ozcan-Atar**, Gediminas Juska, Emanuele Pelucchi "Growth of high-density InGaAs/AlInGaAs quantum dots by MOVPE targeting the 1.3 micron window", XXII 'International Workshop on Physics of Semiconductor Devices (IWPSD) Conference', IIT Madras & Semiconductor Society of India, Chennai, India, 2023

- M. Johnson (oral), **A. Ozcan-Atar**, A. Wojcik, F. H. Peters, P. P. Michalowski and E. Pelucchi, "Electrical characterisation studies of zinc diffusion in metal organic vapor phase epitaxy grown indium phosphide", Compound Semiconductor Week, CSW2023, Jeju, South Korea, June 2023

- E. Pelucchi (invited), A. Ozcan-Atar, A. Gocalinska, "MOVPE of III-V materials: the (neglected) role of surface dynamics and its potentials for next generation devices and integration", Invited talk: Joint AIC-SILS Conference, Trieste, Italy, Sep 2022

- **A. Ozcan-Atar**, A. Gocalinska (oral), P.P Michalowski, D. Vvedensky and E.Pelucchi, "An Unusual Profile of InP During Metal Organic Vapor Phase Epitaxy", Conference: Compound Semiconductor Week , Online, May 2021.

Chapter 1

Introduction

1.1 Introduction

Over the last few decades, extensive research efforts have been directed towards the development and analysis of III-V and III-Nitride compound semiconductor materials and their alloys [1]. These materials have proven to be versatile and high-performing, finding applications in various photonic and optoelectronic devices [2, 3]. Notably, III-V compound semiconductors, such as InP and GaAs along with ternary and quaternary alloys thereof, display direct band-gap properties and are pivotal in the construction of photonic devices designed to operate at specific wavelengths, such as 1.3 μm and 1.55 μm [4]. These semiconductor photonic components serve not only for high-speed internet and data transfer within data centers but also extend through various modern devices and systems, playing a key role in upcoming disruptive technologies such as self-driving cars, advanced medical diagnostics, and emerging quantum technologies and computing [5, 6].

While numerous epitaxial growth technologies have proven successful over the decades, only a handful have been industrially adopted for large-scale, high-volume applications [7, 8]. Metal organic vapour phase epitaxy (MOVPE) stands out as a widely accepted and well-established technology, playing a foundational role in fabricating semiconductor III-V and III-N devices [1]. This method has emerged as a key technique for growing compound semiconductor crystals, gaining prominence for its reproducibility, scalability, and overall excellent control over the growth process [2, 3]. Besides III-Vs and III-Ns, MOVPE finds applications in silicon technologies and emerging materials like nano and atomic-scale engineered 2D materials [9–11].

Nevertheless, despite MOVPE's widespread technological popularity and usage, a considerable number of fundamental issues remain unresolved and a comprehensive insight into the complex physical processes at the atomistic level responsible for the material incorporation is lacking. In other words, there persists a large number of unresolved issues, effectively hindering some of the potential developments of a broad spectrum of cutting-edge devices. One critical challenge in advancing novel semiconductor devices lies in the unpredictable outcome of MOVPE epitaxial growth in new designs or growth regimes. The epitaxial community relies on a 'recipe' approach, lacking a fundamental understanding of the complex surface dynamics influencing the material growth. This deficiency restrains the ability to design growth outcomes, resulting in development strategy of 'trial-and-error'. Historically, the rush to the next technological breakthrough and commercial success overshadowed the pursuit of fundamental knowledge, as a result, in the long term, limiting the development of new technologies.

Within this context, this thesis aims to address some of the knowledge gaps that have been deferred over decades and contribute to a deeper understanding of the physical processes involved. First is an age-old problem i.e., reportedly, the long-range "leakage" of the Zn impurities into the intrinsic layers during (and post) epitaxy, including the device processing steps [12, 13]. Zn is still the most commonly used p-type dopant for the development of III-V based electronic and photonic devices, but it is highly diffusive and historically very problematic [14–19]. To prevent Zn leakage problems, the large majority of InP based devices (such as lasers and modulators) are generally designed with an p-on-n architecture, using the p-type dopant at the top of the device structure (so as to reduce the time for Zn diffusion during growth). It is worth mentioning that published inverted (n-on-p) device structures are exceptionally scarce and primarily limited to highly specialized fields like wafer bonding [20]. This shortage effectively creates a limited guidance for advancing devices that necessitates n-on-p architectures, such as stacking of multiple devices/waveguides for more advanced cost-effective integration [12, 13, 21–23].

The diffusion of Zn is extensively studied in the literature [16, 17, 24–31]. However, published works are often focused on 'back-diffusion' or diffusion through the substrate, which is the opposite of the growth direction, after a layer has been deposited. Reports on the 'forward-diffusion' -the diffusion towards the growth direction (or the opposite direction from the substrate), particularly in relation to the p-on-n device structures- either lacking or the issue is typically addressed as part of a more complex, interplayed effects, making it challenging to disentangle in general [24, 25, 27, 32, 33]. For example, Blaauw and colleagues investigated Zn concentration within the layers of n-p-n-p-n structures, focusing mainly on the effect of varying Si (n-type)

and Zn (p-type) concentration levels [32]. Others focused on piling up dopants near the p-n junction interfaces [33], offering solutions to the problems without further investigating the root cause.

This thesis aims to fill this void through innovative experimental structures, complemented by state-of-the-art secondary ion mass spectrometry (SIMS), electrical, and theoretical analysis. This work presents clear, systematic and comprehensive evidence that the limitations linked with n-on-p devices is not associated only with conventional 'crystallographic' diffusion, but indeed induced by Zn (or its precursor) surfactant behavior. Zn –or its precursor- accumulates and floats on the sample surface during the growth of intentionally doping layer and gradually incorporates into the nominally undoped (NUD) layers after the Zn source is shut off, a typical surfactant dopant behavior.

The second long-standing issue that is discussed in this thesis is also another significant technological interest, i.e. what we call the 'Oxygen-Paradox'. While oxygen incorporation, particularly in aluminum-containing alloys, has been recognized as a potential detriment to device performance [34–36], the complex pathways of its incorporation and the surprising suppressive effects of MOVPE surface progress on oxygen remain unexplored in the literature. Indeed, the dopant-like levels of incorporation are still only a fraction of what they could be expected to be (even with best purification techniques, there is a partial pressure of at least $\approx 10^{-7}$ Torr of oxygen in current reactors, in principle enough to oxidize a monolayer in less than a second) [36–40]. The lack of clarity regarding its origin prevents determining improved paths for elimination of this residual oxygen, as further purification of the reactors and metalorganic sources is difficult.

The motivation behind this thesis is, therefore, addressing two aforementioned critical technological challenges in MOVPE that have persisted for a considerable duration. This research aims to propose effective control measures to these problems, and underscores the significance of surface processes in MOVPE. This thesis will so doing contribute to the implement of robust solutions for novel device designs, crucially enabling the next generation of integrated III-V applications.

1.2 Thesis outline

This dissertation is organized as follows. Following this brief introduction, in Chapter 1, basic background information is given. The Chapter 2 is dedicated to the basis of our fundamental understanding of the experiments conducted in this research. It starts with an overview of the MOVPE process, followed by some literature findings related to the Zn doping and surfactant dopants.

Moving on to Chapter 3, detailed information regarding the sample growths and material characterization methods is provided, covering growth facilities, characterization tools, and methods for material, electrical and optical characterization.

Chapter 4 focuses on the Zn concentration profile of III-V materials along with its incorporation properties. The chapter also addresses the suppression of Zn forward diffusion and explores Zn back diffusion in different misoriented substrates, alongside photoluminescence analysis, leading to a comprehensive discussion and conclusion.

In Chapter 5, a complementing theory of Zn surfactant behavior is presented with coupled equations and numerical modelling with single and two diffusion constants.

Chapter 6 is dedicated to suppressing oxygen incorporation in aluminum-containing alloys, providing a literature summary, insights into removing oxygen in AlInAs with Sb, oxygen reduction in AlGaAs with Sb, cross-sectional AFM results, and a detailed discussion and conclusion.

Finally, in Chapter 7, the thesis concludes with an overall summary, while also outlining avenues for future research.

Chapter 2

Background

This chapter briefly reviews important topics related to this thesis. The aim is not to go into great detail but rather to give a short overview to help grasp the main content in the following chapters. An overview of the MOVPE process, doping in III-V semiconductor and the challenges associated with the Zn doping will be provided. At the end, some background information on the surfactant dopants used in III-V MOVPE will be given.

2.1 Overview of the MOVPE Growth Process

The identification of the first discoverer of MOVPE is a subject of controversy. However, the initial publications of Manesivit in late 1960s and early 1970s are widely acknowledged as laying the foundations of today's MOVPE process [41–44]. Since then, the MOVPE technique has advanced enormously, and today it is the predominant method in commercial manufacturing. This success is achieved due to diligent work on improving the impurities of metalorganic precursors, the advancement of MOVPE equipment for better uniformity and the ability to deposit onto multiple substrates at the same growth cycle [45]. The technique is extensively utilized for the production of various crucial devices, such as semiconductor lasers, light emitting diodes (LEDs), and multi-junction solar cells.

MOVPE is a chemical vapour deposition method for growing single crystalline layers onto a single crystalline substrate via chemical reactions to create complex semiconductor multilayer structures. The MOVPE process simply involves delivering the required group-III and -V elements for the growth of a particular III-V compound or alloy to a heated-substrate crystal

through the vapour phase. While we do not have a complete understanding of the thermodynamic and kinematic principles involved in the method, the MOVPE growth process can be summarised with the following basic steps (Figure 2.1). First, metalorganic precursors and hydrides in vapour-phase are carried via a non-reactive carrier gas such as H_2 or N_2 and mixed just before arriving the reactor chamber. These metalorganics then can react with each other in the gas phase (homogenous reactions) to form intermediate reactants or diffuse directly to the boundary layers of the substrate where they will be adsorbed. The term "boundary layer" is used for convenience to refer to the section of the laminar gas flow next to the substrate, where gas molecules diffuse over a time period of several seconds. It is important to note that an actual stagnant boundary layer does not exist [46, 47]. The absorbed species diffuse on the substrate surface in search for an energetically favourable position. Here, heterogeneous reactions take place (sometimes referred to as the gas-solid interface), leading to the continuous formation of thin films through nucleation, coalescence and growth. Finally, desorbed products and unreacted species are carried away from the reaction chamber. [45, 48]

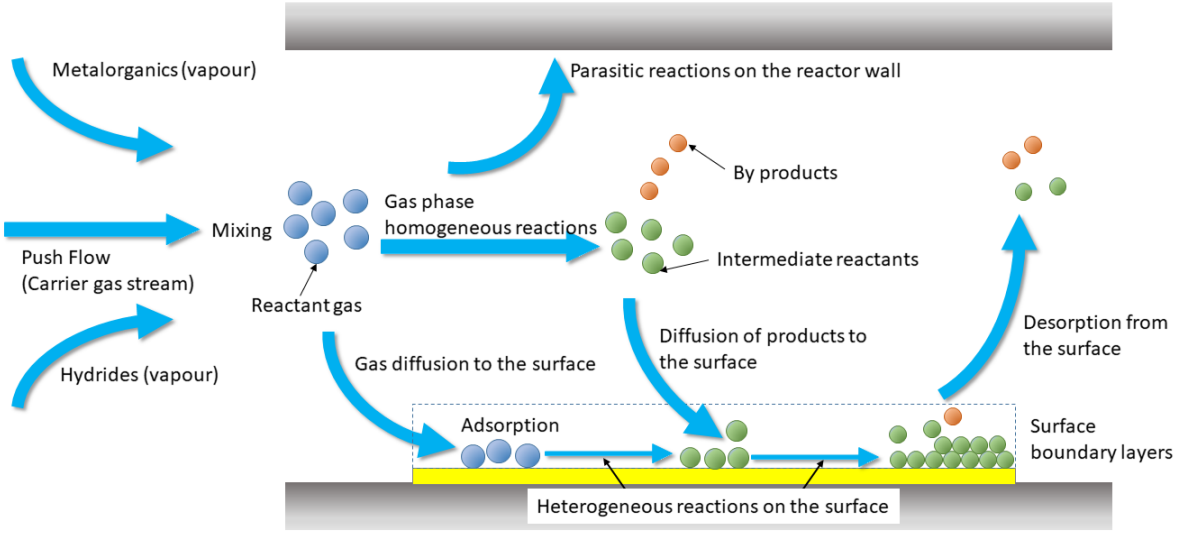


FIGURE 2.1: Schematic representation of fundamental steps of a typical MOVPE process [45]

The stoichiometric reaction equation representing the GaAs growth by using trimethylgallium (TMGa) and arsine (AsH_3) carried by H_2 is as follows:

$$Ga(CH_3)_3 + AsH_3 \xrightarrow{H_2} GaAs + 3CH_4 \tag{2.1}$$

The schematic presented in Figure 2.2 illustrates some of the possible key reaction steps identified for this GaAs reaction, offering valuable insights into the complex nature of reaction kinetics

and alternative reaction paths—a characteristic feature shared by all MOVPE compound semiconductor reactions. [45, 49]

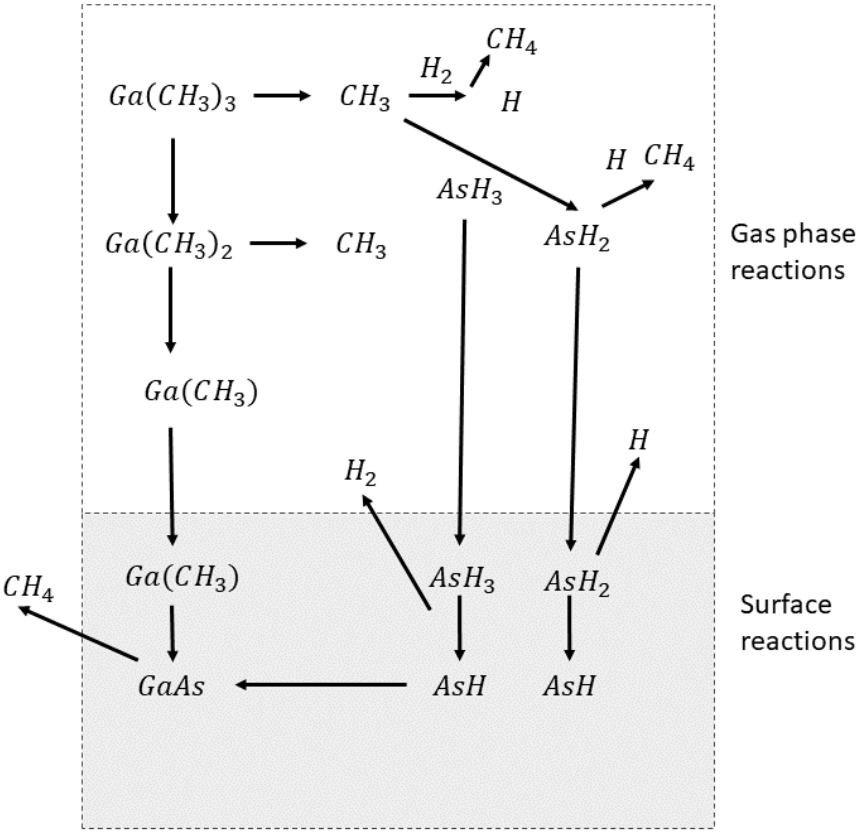


FIGURE 2.2: Some of the probable reactions steps during MOVPE growth of GaAs using TMGa and AsH_3 in an H_2 ambient environment. Adapted from Ref. 45

Besides kinematic reactions, (and surface diffusion and specific advanced surface characteristics), fundamentally, epitaxial growth can be seen in some aspects as a highly controlled phase transition (vapour to solid); therefore, thermodynamic principles (when the kinetic constraints are met) are a strong ingredient of the MOVPE process. Thermodynamics can also, for example, be used to estimate the composition of solid alloys, including dopant incorporation, based on the growth parameters, at least in specific material systems .

As an example, from a contribution by Stringfellow in a 2007 review, the overall (averaging out the processes) reaction of MOVPE growth for GaAs using TMGa and arsine (AsH_3) is as follows [50]:

$$\mathrm{Ga(CH_3)_3(v) + AsH_3(v) = GaAs} \tag{2.2}$$

Here, we assume a complete pyrolysis of TMGa and arsine (AsH_3) in the gas phase to give Ga and As_4. Hence, the kinematics does not constrain the epitaxial growth . The reaction can be

simplified:

$$\mathrm{Ga(v)} + \frac{1}{4}\mathrm{As_4(v)} = \mathrm{GaAs(s)} \tag{2.3}$$

where (v) denotes the vapour phase and (s) denotes the solid phase. It is important to emphasize that Equation 2.3 is a simplified chemical formula and does not fully depict the complex process occurring on the surface. At the surface level, Ga first needs to locate an energetically favourable site for adhesion, followed by the arrival of As (these two events do not happen at the same time and diffusion brings these species together) and, in a solid, each Ga atom is bonded to four As atoms, not one (only on average it is one to one).

For a two-phase, α and β, system the thermodynamic equilibrium condition is expressed in terms of the chemical potential μ_i.

$$\mu_i^\alpha = \mu_i^\beta \tag{2.4}$$

Here, Equation 2.4 implies that moving infinitesimally small number of moles of component in between two phases, α and β, results in no change in the total free energy, which is at its minimum at equilibrium.

The chemical potential of an ideal gas mixture is commonly expressed using the chemical potential in some arbitrary standard state, μ_i^0, indicated by superscript zero.

$$\mu_i = \mu_i^0 + RT \ln\left(\frac{p_i}{p_i^0}\right) \tag{2.5}$$

where p_i is the partial pressure, which is equal to the multiplication of mole fraction x_i and the total pressure P, and the standard state is typically pure component i. Thus, the equilibrium conditions of Equation 2.3 for GaAs (according to Equation 2.5) is then:

$$\mu_{\mathrm{Ga}}^v + \frac{1}{4}\mu_{\mathrm{As_4}}^v = \mu_{\mathrm{GaAs}}^s \tag{2.6}$$

or

$$\mu_{\mathrm{Ga}}^{0v} + \frac{1}{4}\mu_{\mathrm{As_4}}^{0v} + RTp_{\mathrm{Ga}}^e \left(p_{\mathrm{As_4}}^e\right)^{\frac{1}{4}} = \mu_{\mathrm{GaAs}}^{0s} + RT \ln a_{\mathrm{GaAs}}\,, \tag{2.7}$$

where the superscript e indicates the equilibrium value of partial pressure. Then,

$$K_{\mathrm{GaAs}} = \frac{a_{\mathrm{GaAs}}}{p_{\mathrm{Ga}}^e \left(p_{\mathrm{As_4}}^e\right)^{\frac{1}{4}}}\,, \tag{2.8}$$

where K is the equilibrium constant. Equation 2.8 represents the fundamental law of mass

action. When system is not in equilibrium, the thermodynamic driving force required to re-establish equilibrium is:

$$\Delta\mu = \mu^{v}_{\mathrm{Ga}} + \frac{1}{4}\mu^{v}_{\mathrm{As_4}} - \mu^{s}_{\mathrm{GaAs}}\,, \tag{2.9}$$

or

$$\Delta\mu = RT \ln\left(\frac{p_{\mathrm{Ga}} p^{1/4}_{\mathrm{As_4}}}{p^{e}_{\mathrm{Ga}}\left(p^{e}_{\mathrm{As_4}}\right)^{1/4}}\right). \tag{2.10}$$

Equation 2.10 would represent the driving force for deposition and the subsequent epitaxy, at least under the approximations that allow to treat the process as an average thermodynamic ensemble . We can deliberately set up a situation where the vapour pressures of the reactants are higher than the equilibrium. This somehow forces the system to create the desired GaAs solid. The maximum amount of GaAs solid that can be grown is simply the right amount (supersaturation) needed to reach equilibrium. This limit is mainly determined by thermodynamics and how much reactant gas goes through the MOVPE reactor [1, 50]. This description of the growth was based on macroscopic quantities, where thermodynamics predicting the system direction, but often it does not provide the complete picture. In most cases, crystal growth still can occur when the system is far from equilibrium. For example, the formation of nanostructures during MOVPE growth on patterned GaAs substrates, where the segregation in a pyramid structure is not the result of thermodynamic equilibrium; instead, the surface kinematics play an important role where the epitaxy is the result of local differences in adatom diffusion lengths [51]. Similarly, in our cases thermodynamic principles do not explain the complex surface behaviour of Zn dopant, resulting in the asymmetric concentration profile.

Depending on the growth temperature, the epitaxial growth process is generally categorised in three distinct regimes (Figure 2.3), each corresponding to a different mechanism limiting the growth rate. First is the surface-kinetics (or kinetically) limited regime, where the growth temperatures are low ($\leq$550°C). The growth rate is primarily confined by the surface reactions, where the limiting factor for overall growth rate is not the quantity of source material introduced into the reactor; rather, it is the rate at which surface kinetics (e.g. precursor decomposition) occur on the substrate. Thus, increasing the temperature accelerates the kinetics, resulting in higher growth rates.

The second is the mass-transport limited regime, which is observed at higher temperatures (typically between 550°C to 800°C). In this scenario, the growth rate is not constrained by surface kinetics since the kinetics is fast enough to not to hinder any decomposition and incorporation

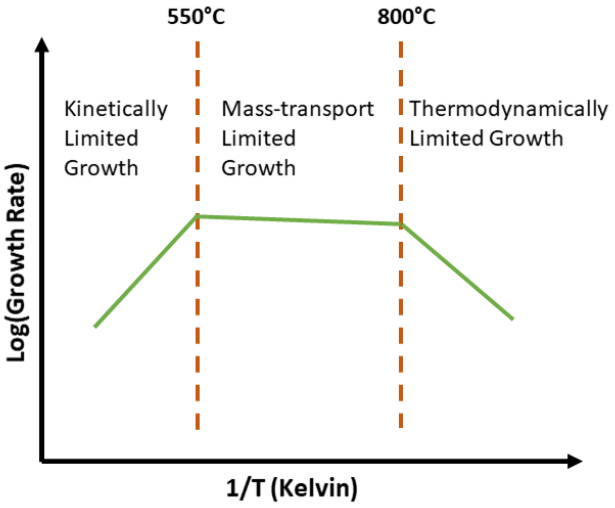


FIGURE 2.3: Schematic representation of the three distinct growth regimes depending on the temperature

process. However, the growth rate is instead proportionally influenced by the quantity of precursors reaching into the substrate. Notably, the temperature becomes less of a limiting factor in this regime, and the growth rate is quite independent of the temperature. Because of this independence, mass-transport limited regime is particularly advantageous and mostly adapted condition for the growth of III-V semiconductor structures. In other words, most MOVPE epitaxial growths occur in that growth regime, as it is easier to control the growth rate and modern reactor designs are optimised to be operated in that regime.

The third and final regime is the thermodynamically limited regime, characterized by specific conditions where neither surface kinetics nor mass transport dominates the growth rate. In this regime, thermodynamic constraints become the primary factors influencing the epitaxial growth process, although alternative factors, like the depletion of reactants on the reactor walls upstream from the substrate, should also be taken into account when examining this regime. In this regime, the growth rate is inversely proportional with the temperature, as it decreases by increasing the temperature. An excellent and more detailed development of the growth process can be found in Stringfellow's book [1].

Growth takes places through step propagation or the formation and propagation of two and/or three-dimensional islands, depending on the interaction energies of the substrate atoms and deposited film atoms. The formation of the layers on a suitable substrate can be distinguished into three fundamental growth modes, as illustrated in Figure 2.4: layer-by-layer growth (Frank-Van der Merwe mode), island growth (Volmer-Weber mode) and Stranski-Krastanov mode [52].

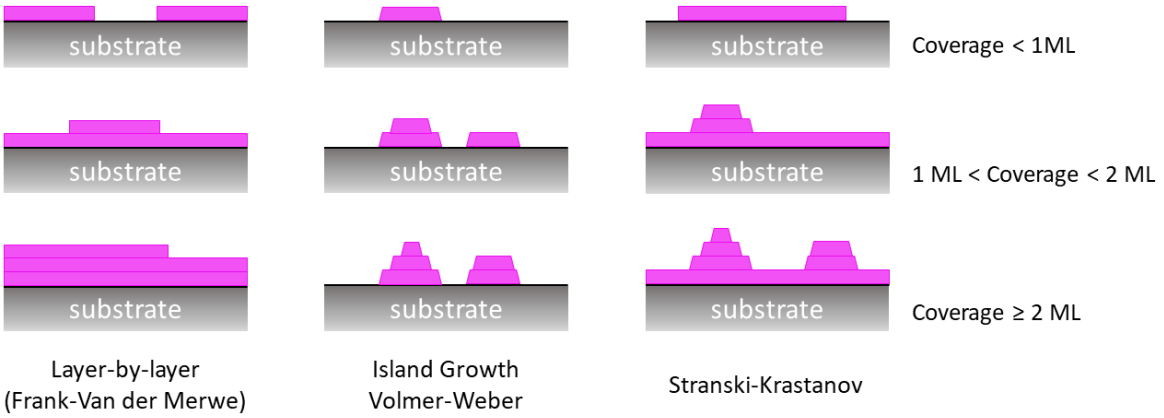


FIGURE 2.4: Schematics diagram of three fundamental growth modes of MOVPE, in the units of coverage vs monolayer (ML). Adapted from Ref. 52

The choice of mode depends on the wetting angle ϕ between the film and the substrate (Figure 2.5). Layer-by-layer growth is observed when the wetting angle is near zero, indicating that the interaction between surrounding atoms is smaller than the interaction between substrate and film atoms. In that growth mode, deposition occurs through the formation of two-dimensional nuclei or monoatomic steps. This growth mode is predominantly observed mostly in homoepitaxial or heteroepitaxial systems when the lattice mismatch between the deposited material and substrate is insignificant. Island growth mode occurs when the wetting angle is positive. In this scenario, the interaction between film atoms is stronger than between adjacent film and substrate atoms, leading to the formation of three dimensional nucleus islands. Stranski–Krastanov mode combines both two-dimensional layer-by-layer growth and three-dimensional island growth. This mode occurs when the stress affects the two-dimensional growth process.

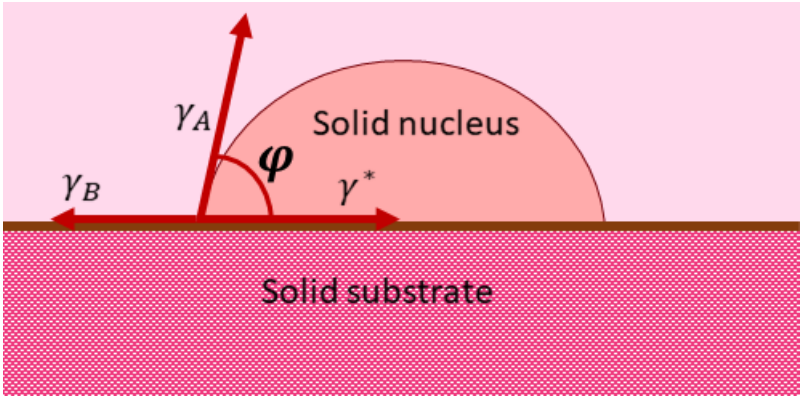


FIGURE 2.5: Young's equation describes the wetting angle (ϕ) of a liquid nucleus on a substrate in terms of surface energies. The surface energy of the substrate (γ_B), the surface energy of the film material (γ_A), and the interface energy between the film and the substrate (γ^*) have the following relationship $\gamma_B = \gamma^* + \gamma_A \cos\phi$.

2.2 Doping in III-Vs

The introduction of impurities into a semiconductor is called doping. A dopant is a foreign element with a different valance electron configuration than the atom it replaces. Specific impurities can significantly influence the electronic characteristics of an intrinsic semiconductor, by moving its Fermi energy level, thereby making the semiconductor extrinsic. For example, incorporating one boron (B) atom for every 10^5 silicon (Si) atoms increases the conductivity of pure (Si) at room temperature by a factor of 10^5 [53]. Mainly there are two dopant types: p-type and n-type. N-type dopants provide one more electron as the majority carrier. P-type dopants provide one less electron and generate holes as the majority carriers. Doping is essential for semiconductor device technologies, being widely applied in almost all semiconductor materials including III-Vs. Through delicate control of the doping concentration and distribution, semiconductor properties such as electrical conductivity, carrier concentration, and mobility can be tailored to meet the specific requirements of various device applications.

III-V semiconductors are exceptionally stable solids composed of cations in Group 13 (formerly Group IIIA) and anions in Group 15 (formerly Group VA) of the periodic table. These compound semiconductors crystallize in a zinc-blende structure (except III-Ns) with a tetrahedral symmetry, characterized by mainly covalent sp^3 bonds. In this structure, each atom forms four covalent bonds, one with each of its nearest neighbours. Dopants incorporated into a III-V compound semiconductor lattice predominantly occupy substitutional lattice sites, where the lattice site can be either a cation or an anion site. The preference for one site over the other depends on factors such as valance electron correlation, bond strength, and dopant size including strain effects [54]. Figure 2.6 illustrates schematic representation of impurities incorporated into a III-V lattice.

Dopants can be incorporated into the semiconductor lattice through three primary techniques: doping during epitaxial growth, doping via implantation, and doping through diffusion. In this thesis, the focus will be on the first technique -doping during epitaxial growth, specifically by MOVPE- as it is the sole method employed in our research.

In the context of MOVPE, doping involves introducing specific doping precursors into the reaction chamber during the epitaxial growth process of the III-V semiconductors. These precursors can be either inorganic, e.g. silane (SiH_4) and disilane (Si_2H_6), or organometallic, e.g. diethylzinc (DEZn) and tetramethyltin (TMSn). The requirements for a dopant precursor is as follows:

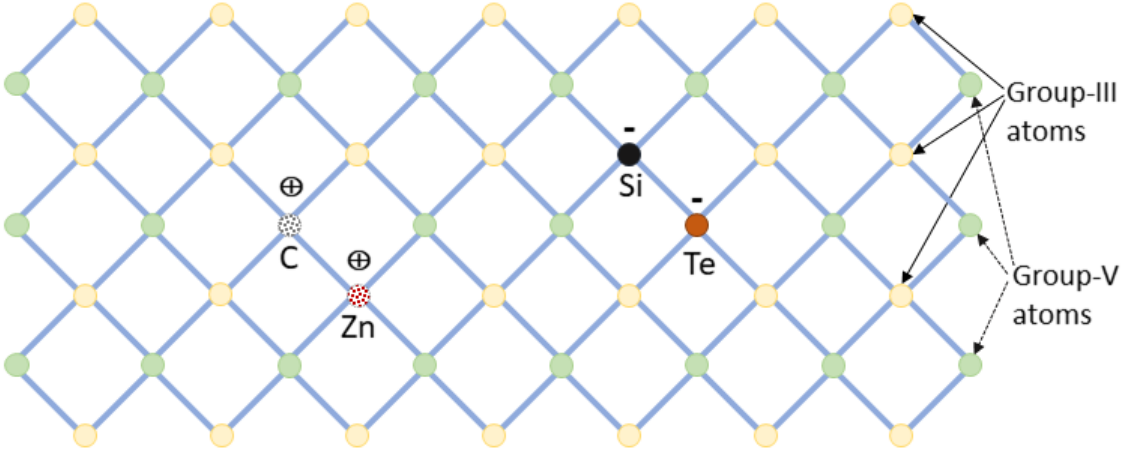


FIGURE 2.6: Schematic illustration of two dimensional zinc-blend lattice consisting of group-III and group-V elements. Acceptors like Zn and C have a deficit electron and Si and Te has an excess electron.

- Should have a sufficiently high vapour pressure at or near room temperature
- Should not react in the gas phase of MOVPE system before reaching the substrate.
- Fully decompose at or near the growing crystal surface
- Should be electrically activated when incorporated into the semiconductor
- Should not exhibit a reactor memory effect.

For most dopants, the dopant concentration incorporated into the solid is typically directly proportional to their concentration in the vapour phase for low dopant concentration values. Tuning the dopant concentration in the solid can be easily achieved by proportionally adjusting the vapour phase doping concentration [35].

2.2.1 Zn doping of InP

InP is one of the most investigated III-V compound semiconductor material and is composed of combining In (Indium, group-III) and P (Phosphorous, group-V) elements from the periodic table. It is the material of choice for many photonic and electronic devices, and it is of major interest in integrated photonics. This preference is due to the availability of "cheap" substrates and its being lattice-matched with ternary and quaternary alloys, allowing devices to operate efficiently at the crucial optical communication wavelengths of 1.3 μm and 1.55 μm.

One of the challenges regarding the fabrication of InP devices stem from the lack of "absolutely good" elements for p-doping of the semiconductor and the properties of the available ones. Zn is the most commonly used p-type dopant in MOVPE grown InP semiconductors, with the precursors either dimethylzinc (DMZn, $(CH_3)_2Zn$) or diethylzinc (DEZn, $(C_2H_5)_2Zn$).

The Zn incorporation mechanism into InP layers during MOVPE growth has been extensively studied [29–31, 55–57]. Generally, Zn is believed to sit substantially within the In (III-group) sites within the InP lattice [29], where it has a shallow acceptor level. The saturation concentration of Zn doping in InP is usually reported to be around mid-10^{18} cm^{-3} range [1, 29, 57–60]. This is one of the main constraints employing Zn as a p-type dopant in InP, where additional increases in Zn concentration fail to increase the hole concentration further. Several potential reasons are suggested for this phenomenon, including but not limited to: increase in the interstitial Zn concentration, phase segregation and the forming of other compensating defects, specifically phosphorus vacancies and its complexes with Zn [61, 62].

The typical incorporation efficiency of Zn is generally very low [29, 30], around 0.2% or less. This means that less than 0.2% of the molecules injected into the reactor could be incorporated into the crystal matrix with a molar ratio of TMIn/DEZn $\approx$ 50 [63]. A linear relationship between the precursors flow rate and hole concentration is obtained until the saturation levels [57, 64].

Recent studies have revealed a more intricate process about Zn incorporation into the InP layers during the MOVPE growth, in which, Zn incorporation is suggested to occur at defect sites [29, 30]. An adsorption-desorption-trapping model is used to describe Zn incorporation into the growing epi-layers. The incorporation process starts with the adsorption of Zn atoms at the surface defect sites. As the layer growth continues, the adsorbed Zn species are subsequently trapped into the bulk lattice. Depending on the type of the surface defect, Zn can be substitutional, interstitial and neutral. If Zn is incorporated as a substitutional atom, it eventually occupies indium sites (III-group sites) and bonds with P (V-group sites) [29]. This incorporation mechanism is the optimal mechanism for ionizing the Zn dopants. Early studies established the ionization energy of Zn acceptors in III-V semiconductors to be between 25 and 30 meV, indicating that at room temperature, Zn impurities (occupying the III-group sites) are fundamentally activated. [18, 65]

As this aforementioned incorporation process continues, the dopants keep leaking through the grown layers and a joint diffusion-incorporation mechanism needs to be used to model the

doping behaviour. The next section gives a brief summary of the diffusion mechanism.

2.3 Diffusion of Dopants

When a concentration gradient is present and at sufficiently high temperatures, atoms undergo *diffusion*, i.e., atoms move within material from high to low concentration. The diffusion is a desired phenomenon in some cases, as in doping by ion implantation. Other times, it is detrimental, such that diffusion alters the abruptness of interfaces in heterostructures and the spatial distribution of defects, which can result undesired consequences for semiconductor devices.

Diffusion of atoms is a complex system as atoms can diffuse via various diffusion mechanisms and diffusion paths, governed by temperature, material composition and defect concentration. Mathematically, a flux equation, known as Fick's first law, is an (historically) phenomenological description of diffusion assuming the concentration gradient as the main source of diffusion, similarly to Einstein diffusion equations (or Fourier temperature flow equation). The one-dimensional flux low is expressed as:

$$j = -D\frac{\partial C}{\partial x} \tag{2.11}$$

where j denotes the flux, D represents the diffusivity, C is the concentration of the diffusing substance, and x is the spatial coordinate. And the one-dimensional diffusion equation, known as Fick's second law is defined by the flowing equation [66]:

$$\frac{\partial C}{\partial t} = -D\frac{\partial^2 C}{\partial x^2}. \tag{2.12}$$

One of the solutions of Equation 2.12, for instance, in the case of in-diffusion of a species from the surface (at x=0) of an semi-infinite solid, where the surface concentration remains constant at C_s, is the complementary error function

$$C(x,t) = C_S \ \mathrm{erfc}\left(\frac{x}{\sqrt{4Dt}}\right). \tag{2.13}$$

if D is constant [67]. This is the simplistic solution and most diffusion processes are more complex than that. For more complicated cases, such as when there is more than one diffusing species or for some other boundary conditions, numerical methods are necessary to solve the diffusion equations.

Atoms diffuse within a crystalline solid by hopping between lattice sites. When an atom vacates a lattice site, it must be substituted to maintain the overall number of lattice sites within the solid. This substitution does not always involve another atom; it can also involve a vacancy, as will be explained in the following sections. Various atomic diffusion mechanisms within crystals are classified into two main categories: those involving point defects and those not involving them [68, 69]. The following sections outline some of these mechanisms.

2.3.1 Diffusion Mechanisms without the Involvement of Point Defects

- **Interstitial Mechanism**

Conceptually, this is the most straightforward diffusion mechanism. Some impurity atoms, generally those considerably smaller than the host atoms, are incorporated on interstitial sites of the host lattice. An interstitial impurity can diffuse by jumping from one interstitial site to a neighbouring interstitial site as shown in Figure 2.7a. Considering the atomic movement during a jump, the mechanism occurs with the following steps: The interstitial atom initially resides at an equilibrium position, then transitions to a saddle-point configuration where the lattice experiences maximum straining. Subsequently, it settles onto an adjacent interstitial site. During this transition, neighbouring matrix atoms must temporarily move aside to accommodate the solute atom's passage. However, once the jump is complete, there are no lasting displacements of the matrix atoms [70]. No native defects are necessary to initiate the jump and none are involved during the process.

Generally, the diffusivity is considered to be fairly high compared to those of substitutional atoms for several reasons. No significant bond breaking is needed in this mechanism. There are more empty interstitial sites than vacancies, so jumping is easy. The interstitial impurities does not need to wait for a defect to perform the jump.

This mechanism is particularly relevant for the diffusion of small foreign atoms, e.g., H, O, Cu, Ni, and Fe, etc in Si, as this atoms can fit snugly into interstitial sites without significantly displacing the host atoms from their regular lattice positions [67, 70].

- **Ring Mechanism**

Impurities with similar sizes to the host atoms typically occupy substitutional lattice site, requiring a mechanism different from interstitial diffusion. In the 1940s, there was a common

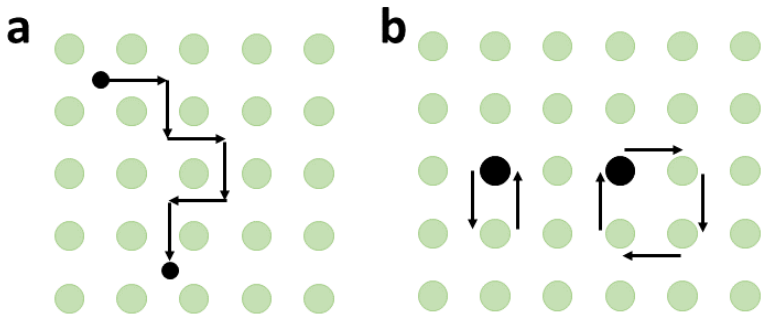


FIGURE 2.7: Diffusion mechanisms without the involvement of point defects. a) direct interstitial mechanism b) direct exchange (b-left) and ring diffusion (b-right) mechanisms.

misconception about atomic diffusion suggesting that it occurs via a direct exchange mechanism. In that mechanism, diffusion of self-atoms and substitutional solutes in metals occurs through a direct exchange of neighbouring atoms (Figure 2.7b-left), involving the simultaneous movement of two atoms [70]. However, in a close-packed lattice, this movement requires significant distortion to accommodate atoms, resulting in a high activation barrier and making the process energetically unfavourable. Sophisticated theoretical calculations later led to the conclusion that 'direct exchange' mechanism at least in close-packed structure was unlikely to be a possible mechanism [71, 72].

For substitutional impurities, the only possible mechanisms without the involvement of point defects is the ring mechanism (Figure 2.7b-right) [67]. The ring mechanism involves the rotational movement of a group of at least three atoms by a distance of one atom [73]. This mechanism usually, linked to a very large enthalpy of migration (too many bonds needs to be breaking at the same time) and it was not previously recognised as a diffusion phenomenon in any semiconductor crystalline solid. Some more recent studies show the concerted-exchange mechanism, which is a specific type of ring-mechanism, can have contribution to diffusion in Si [67, 74].

2.3.2 Diffusion Mechanisms Involving Point Defects

- **Vacancy Exchange Mechanism**

It is widely accepted that the dominant mechanism for the diffusion of matrix atoms and of substitutional impurities in metals is the vacancy mechanism. In that mechanism an atom diffuses by jumping into a neighbouring vacancy (Figure 2.8). The limitation that constrains the motion of an adjacent atom into a vacancy in a close-packed lattice is smaller than the

limitation in the direct or ring diffusion mechanism. Each atom moves through the crystal lattice through a sequence of exchanges with nearby vacancies that occasionally come into its vicinity [70].

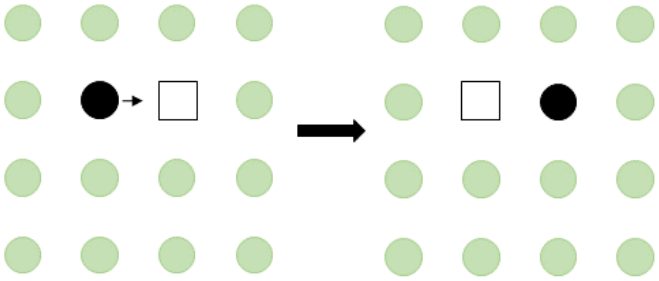


FIGURE 2.8: Vacancy exchange mechanism. White square depicts the vacancy, black and green circles depict tracer and matrix atoms, respectively

- **Interstitialcy Mechanism**

Diffusion may occur through the interstitialcy mechanism, also known as the indirect interstitial mechanism, when an interstitial atom closely matches the size of the lattice atoms (or the lattice atoms within a specific sublattice in a compound). Self-interstitials, which are additional atoms positioned between lattice sites, serve as vehicles for diffusion. In that mechanism, a substitutionally located atom undergoes an exchange with a self-interstitial, subsequently being displaced into an interstitial site. From there, it transitions to a neighbouring lattice site by displacing the lattice atom (Figure 2.9) [70].

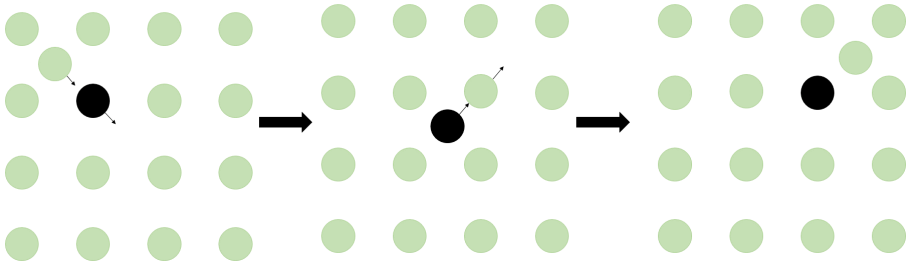


FIGURE 2.9: Interstitialcy mechanism of diffusion. A substitutional atom exchanges with a self-interstitial (middle), moving into an interstitial site (right).

- **Divacancy Mechanism**

Under thermal equilibrium conditions, single vacancies (or monovacancies) form divacancies by combining together, expressed by the reaction equation:

$$V + V \rightleftharpoons 2V \tag{2.14}$$

Substitutional impurities, then, can diffuse through divacancies as shown in the Figure 2.10. Due to divacancy binding and the lower defect symmetry, diffusion via divacancies follows slightly modified equations compared to monovacancies. Otherwise, the two mechanisms are quite similar [70].

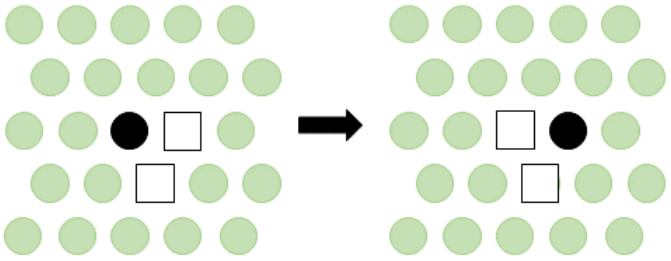


FIGURE 2.10: Divacancy mechanism of diffusion. A substitutional impurity switch with a divacancy (a vacancy complex formed by combination of two vacancies).

- **Interstitial-Substitutional Exchange Mechanism**

Certain impurities (B) can be incorporated into both interstitial (B_i) and substitutional (B_s) sites within a host crystal (A). They may diffuse through one of the interstitial-substitutional exchange mechanisms, as shown in Figure 2.11. Typically, the mechanism involves changing over from interstitial sites to substitutional sites or vice versa, requiring the participation of point defects. Generally, it is observed that the diffusivity of interstitials (D_i) is higher than the diffusivity of substitutionals (D_s). Conversely, the solubility is generally lower in the interstitial state [70].

Mainly, there are two distinct types of interstitial-substitutional exchange mechanism (Figure 2.11). One of these mechanisms (Figure 2.11a), proposed by Frank and Turnbull in 1956 for rapid diffusion of copper in germanium [75], known as Frank-Turnbull or dissociative mechanism. This mechanism involves vacancies (denoted as V) and can be expressed with the following reaction equation [75]:

$$B_i + V \rightleftarrows B_s. \tag{2.15}$$

The second one, known as the kick-out mechanism (Figure 2.11b), was proposed by Gösele et al. to explain the rapid diffusion of Au in Si [76]. In this mechanism, self-interstitials (A_i) are involved by the following reaction equation:

$$B_i \rightleftarrows B_s + A_i. \tag{2.16}$$

In general, in III-V components, the diffusion of impurities are generally described by an interstitial-substitutional mechanism, where diffusion is believed to occur via charged point defects. Therefore, in that case, the charge state of the involved species should be taken into account [77].

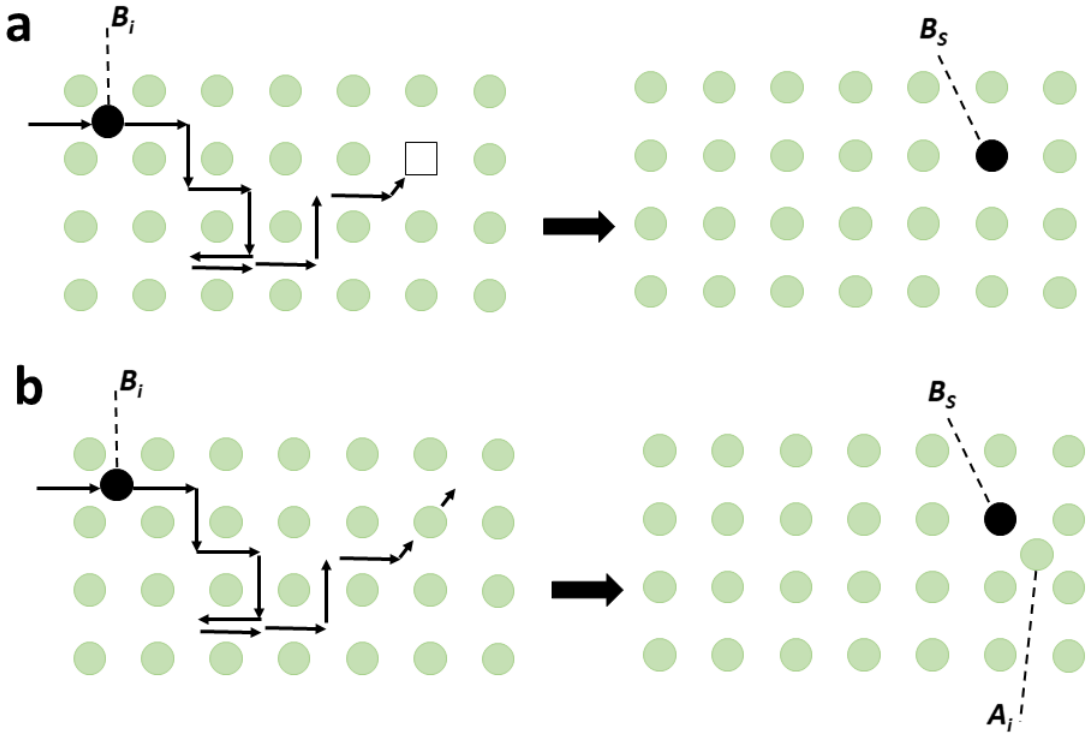


FIGURE 2.11: Schematic representation of interstitial-substitutional exchange mechanisms of impurity atom diffusion. a) Frank-Turnbull mechanism b) kick-out mechanism

2.3.3 Literature Overview of the Zn Diffusion Mechanism in InP

A great deal of effort is put into understanding of Zn diffusion mechanisms in III-V semiconductors for many years [15, 16, 27, 28, 32, 56, 60, 78, 79]. Zn has reportedly a relatively high diffusivity of 6.5×10^{-14} to 1.3×10^{-12} cm^2/s in InP at temperatures in the range of 500°C-650°C [26, 79]. Studies are mainly focused on the Zn diffusion through the substrate (opposite growth direction) [16, 17, 26–31].

The diffusion of Zn in InP (back-diffusion or opposite growth direction, specifically) is thought to be primarily driven by the highly mobile Zn interstitials (Zn_i), which are in chemical equilibrium with substitutional Zn (Zn_s). The overall concentration of interstitial Zn is insignificant compared to the substitutional Zn. As mentioned in the previous section, it is widely accepted that the diffusivity of interstitial Zn is much larger than the diffusivity of substitutional Zn [80].

These fast diffusing Zn interstitials facilitate the movement of Zn atoms from regions of high to low concentration, eventually transforming into substitutional or neutral Zn through chemical reactions involving In vacancies (Frank-Turnbull mechanism) [75], In lattice atoms (kick-out mechanism) [76, 81], or phosphorus vacancies (neutral complex) [15].

The Frank-Turnbull mechanism of Zn in InP can be expressed by the diffusion reaction equation:

$$\mathrm{Zn}_i^{(m+)} + V = \mathrm{Zn}_s^- + (m+1)h, \tag{2.17}$$

where $\mathrm{Zn}_i^{(m+)}$ is an interstitial Zn donor with charge $m+$, Zn_s^- is a singly ionized substitutional Zn acceptor, V is a vacancy on the III sublattice, and h is a hole. The diffusivity of interstitial Zn is assumed to be much larger than that of substitutional Zn or of a lattice vacancy [26].

The kick-out mechanism of Zn in InP can be expressed via the following diffusion reaction equation,

$$\mathrm{Zn}_i^{(m+)} = \mathrm{Zn}_s^- + \mathrm{I}_{\mathrm{In}}(m+1)h, \tag{2.18}$$

where charged $\mathrm{Zn}_i^{(m+)}$ kicks out an In atom from its lattice site (I_{In}) to form substitutional Zn acceptor Zn_s^- [81].

The literature on the diffusion through the growth direction (forward-diffusion) is notably very limited. Reports specifically addressing on Zn profile are either missing or the given as part of more complex interplayed structure, which is difficult to disentangle [24, 25, 27, 32, 33]. For example, Blaauw and co-workers, investigated Zn distribution of the layers in n-p-n-p-n structures, focusing mainly on the effect of varying Si and Zn concentration levels [32]. Others focused on the piling up of the dopants near the p-n junction interface [33].

No reports have specifically investigated the Zn concentration profile within an InP/InP:Zn/InP structure, with only one rare exception [56]. However, in this particular study, Zn does not demonstrate the same asymmetric behaviour observed in our research. One main reason to this disparity can be due to the differences in the SIMS methodology employed. As we will elaborate in detail in Chapter 3.2.1.1, SIMS methodology plays an important role in accurately measuring Zn concentration.

As of today, there has been no report in the literature indicating that Zn exhibits surfactant properties (but it does, as we will demonstrate). The subsequent section will provide background information on the utilization of surfactants in MOVPE and outline the characteristics associated with surfactant dopants.

2.4 Surfactants and Surfactant Dopants in MOVPE

The effort to control and alter surface thermodynamics and kinetics has led to the use of surfactant species in MOVPE growth.

The term 'Surfactant' has a specific description in chemistry: *"A substance which lowers the surface tension of the medium in which it is dissolved, and/or the interfacial tension with other phases, and accordingly is positively adsorbed at the liquid-vapor or other interfaces."* [82]. This term has a much broader content in the crystal growth and epitaxial literature, referring to any species segregated on the growth surface that impacts growth behaviour, composition, or defect structure [83]. Numerous groups has reported the surfactant behaviour in MOVPE highlighting its influence on various aspects such as growth behaviour, impurity incorporation, composition, atomic ordering, surface roughness and defect formation [34, 84–92]. For example, Heckelmann et al. used trimethylantimony (TMSb) to prevent $Ga_{0.51}In_{0.49}P$ from ordering [34]. It has been shown that the addition of Bi during MOVPE growth of InGaP layers significantly increase the step bunching behaviour, eliminating the three-dimensional islanding [84]. Sato and co-workers have reported an enhanced p-doping concentration levels by using Sb during the MOVPE growth of InGaAs layers [87].

Dopants exhibiting surfactant properties such as Te and Bi have been reported to accumulate and float on the epi-surface after reaching the saturation levels [86, 93]. Lee et al. reported that Te effectively reduced the surface roughness by eliminating step bunching in GaAs epitaxial layers [94]. Some authors have shown that the presence of Te dopants in unintentionally doped post-growth layers (layers formed after the dopant source is closed) does not result from desorption or parasitic reactions from the walls. Instead, it originates from the surface itself, different from the classical reactor memory effect [95, 96]. Without explicitly designating Zn as a surfactant, Gocalinska et al. previously demonstrated that Zn dopants notably influence the step organization of InP surface structures in MOVPE-grown InP layers, such as reducing step bunching [63]. When this thesis work started, more experiments were needed to investigate the Zn surfactant properties, specifically by analyzing the Zn concentration profile in post-growth epi layers.

Chapter 3

Material Growth and Characterization Methodology

3.1 Our MOVPE Facilities and Material Growth

For this research, all the samples are grown in a commercial horizontal high-purity Aixtron MOVPE reactor at low pressure (80 mbar) by using purified N_2 as the carrier gas [97]. There are two reactors mounted on this MOVPE system which share the same gas handling system: Aix200-Reactor 1, configured for a single central 2-inch wafer, and Aix200/4-Reactor 2, capable of accommodating a maximum of three 2-inch wafers. Reactor-1 is used for high purity processes while reactor-2 is used for all device growths. Some dopants (including Zn) are not used in reactor-1. To avoid any cross-contamination that can be desorbed during growth from the dopant run-vent lines, the pneumatic valve enabling the dopant path toward the selected reactor is kept forced to exclude reactor-1, thereby ensuring to divert any dopant flow towards reactor-2. This feature was added in-house and is not included in the standard Aixtron system.

To ensure high purity standards in the grown samples two more specific modifications were made to the in-house MOVPE system. First, is the purification process of N_2. The carrier gas (N_2) undergoes a stringent purification process to achieve a purity level in the sub-ppb range. SAES Getters metallic-alloy technology, a zirconium-based getter technology, is used for effective removal of impurities such as O_2, H_2O, CO, CO_2, H_2, and CH_4. Two SAES Getters purifiers in series are used to ensure complete removal; with contamination levels below 1ppb for O_2, H_2O, CO, CO_2, H_2, and CH_4. The second modification is the double purification process of the

group-V sources. AsH_3 and PH_3 used to have contamination levels above the sub-ppb range, mostly related to contaminations related to the cylinder change and their depletion in time. Purging of the hydride lines is carried out periodically, to prevent degradation of contaminants inside the pipe. Each hydride source is equipped with a valve-line configuration that connects two separate purifiers in series, providing the flexibility to use either one or both of them. So that, separate purging procedure can be applied by avoiding the cross contamination during the process.

The key parts and events during the MOVPE process are illustrated in Figure 3.1. The carrier gas (for this research N_2), after being purified, is bubbled through metal organics, co-flowing with the purified hydrides toward the reactor. A Run/Vent switch is installed at the outlet of each hydride and metal organic (MO) source, allowing the flow to be directed either to the run line (leading to the reactor chamber) or to the vent line (leading to the exhaust).

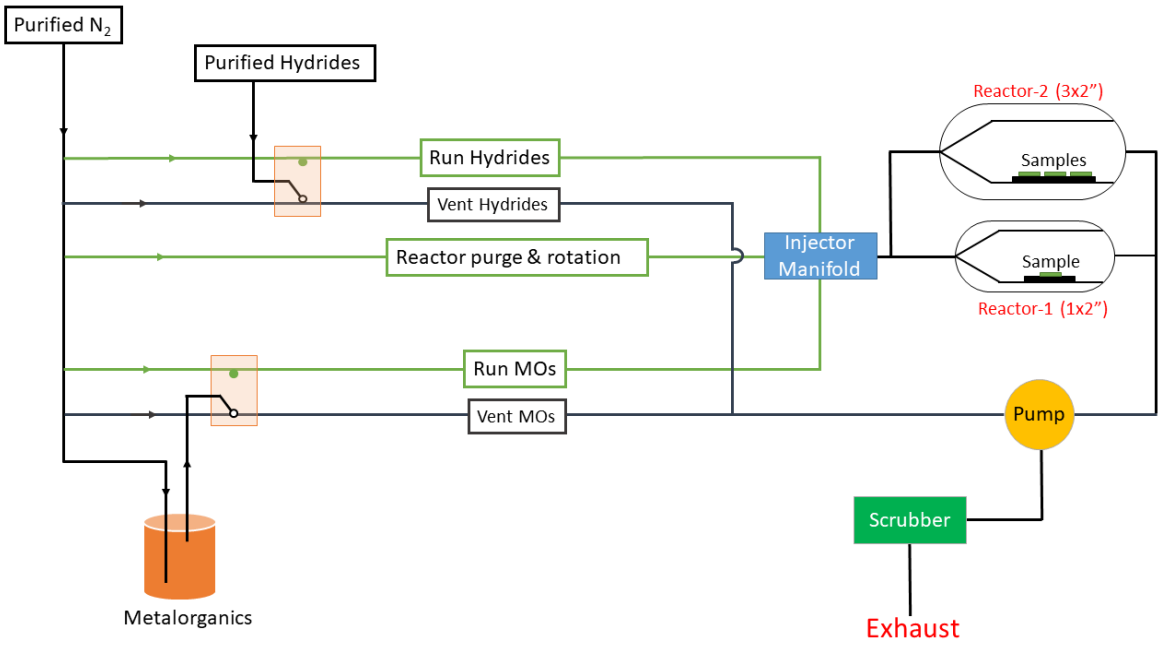


FIGURE 3.1: Schematic diagram of the major components of the MOVPE system. Metalorganics and hydrides are carried by purified N_2 toward either to the reactor (via run line) or to the exhaust (via vent line). A manifold injector flange, equipped with multiple pneumatic valves, facilitates the introduction of sources, purge, and rotation fluxes into the reactor. A (dry) pump regulates the reactor's operational pressure.

The precursor streams enter the reactor through an injector manifold flange in a horizontal reactor setup. Substrates are placed on a rotating graphite satellite, as shown in Figure 3.2, which spins fast enough to ensure uniform thickness, composition, and doping across the substrate wafer. The rotation is facilitated with a laminar N_2 flow through rotation lines underneath the satellite, establishing a uniform boundary layer over the substrate. The reactor is heated by

infrared (IR) lamps, radially arranged under the reactor. When the precursor streams reach the stagnant boundary layer over the substrate, the deposition process starts.

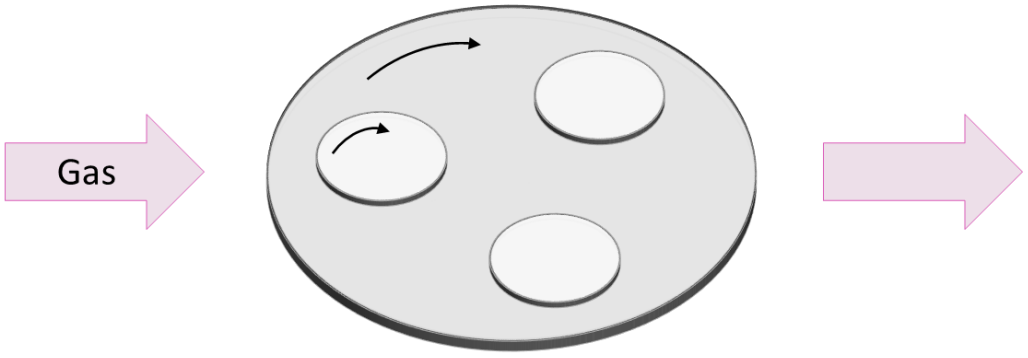


FIGURE 3.2: Schematic of the planetary motion of three substrates on a multiwafer MOVPE graphite reactor. Each satellite, as well as the main holder, rotates around the centre, ensuring uniformity of thickness, composition, and doping concentration.

The MO sources can be either pyrophoric liquids or high vapour pressure solids, stored in stainless steel containers. As mentioned previously, to transport the MO source to the reactor chamber, a controlled flow of carrier gas (high-purity N_2) is introduced into the MO container. Within the container, the MO source occupies the lower part of the vessel, considering that most MOs are in liquid form at the operating temperature. Above the top level of the source, a volume is present, containing a mixture of source gas and carrier gas due to the vapour pressure of the MO source. The carrier gas (N_2) is bubbled inside the liquid source (when the source is liquid) constantly to maintain a constant vapour pressure inside, hence the name "bubbler" for these MO containers. Figure 3 illustrates a schematic representation of an MO bubbler. Bubblers are kept inside thermobaths at constant temperature. Both carrier and source gas flows are controlled by electronic mass flow controllers (MFCs) and pressure controllers (PCs). This ensures the precise delivery of mass flows via run lines to the reactor while minimizing fluctuations of their parameters.

Metalorganics, including trimethylindium (TMIn), trimethylaluminum (TMAl), trimethylgallium (TMGa), diethylzinc (DEZn), trimethylantimony (TMSb); and hydrides such as phosphine (PH_3), arsine (AsH_3) and disilane (Si_2H_6), were used as the main precursors in this research. It is crucial to emphasize that each precursor source is equipped with its dedicated Run/Vent switch. As depicted in Figure 3.3 the Run/Vent switch establishes a connection from the outlet of the MO bubbler (the connection is similar for hydrides) to either the run line, directing gas to the reactor chamber, or the vent line leading to the exhaust. To prevent any turbulence when

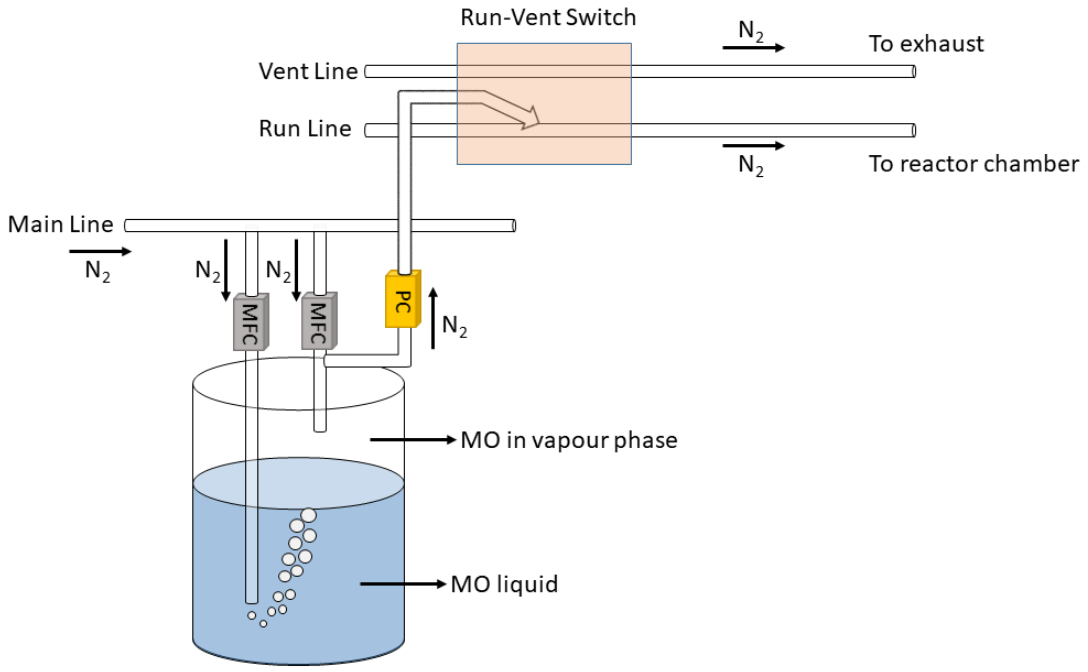


FIGURE 3.3: Schematic diagram of the key parts of a metalorganic (MO) bubbler. During the growth the MO stream is either directed to the run line or the reactor chamber. Gas flows are controlled by electronic mass flow controllers (MFCs) and pressure controllers (PCs).

switching between run line and vent line, their pressure is maintained identical to that in the reactor chamber. The system operates in the following two states:

1. **Run State**: The process gas flows into the run line, while the vent line remains unconnected to the process gas. Simultaneously, an equal flow of carrier gas passes through the vent line.

2. **Vent State**: The process gas is directed to the vent line, bypassing the reactor. Simultaneously, an equal flow of carrier gas passes through the run line.

Note that the flow in the run lines is deliberately kept constant during the growth, which is achieved by providing a compensation to the working Run/Vent switches with carrier gas (N_2) flow. This procedure aims to minimize flow transients and to mitigate the 'start-up effects'. The objective is to achieve abrupt interfaces, which are particularly crucial when, for example, growing multiple quantum well structures.

The substrate loading process into the reactor chamber is executed within a glove box under N_2 flow. Before growing the epi-layers, a de-oxidation procedure at a (thermocouple) temperature around $\simeq$700/800°C under a high hydride flow rate AsH_3 for GaAs substrates, PH_3 for

InP substrates) is applied. Detailed information on other growth conditions, including V/III ratio, growth rate, and growth temperature, is provided for each specific section where the corresponding experimental results are discussed.

3.2 Characterization Tools

Samples grown in the MOVPE reactor underwent various characterization analysis for different purposes. Atomic force microscopy (AFM) is employed for surface characterization. High-resolution X-ray diffraction (HRXRD) is used to measure alloy concentration and strain analysis. Techniques such as secondary ion mass spectrometry (SIMS), Hall effect measurements, capacitance-voltage (C-V) profiling, electrochemical capacitance-voltage (ECV) profiling and scanning spreading resistance measurement (SSRM) are used for the dopant analysis. Additionally, photoluminescence (PL) measurements were conducted to assess energy states. Brief background information regarding these techniques and methodical details of this research will be provided in the subsequent sections.

3.2.1 Dopant Characterization

3.2.1.1 Secondary-Ion Mass Spectrometry (SIMS)

Secondary ion Mass spectrometry (SIMS) is a powerful mass spectrometry technique used to characterize the concentration of atomistic species inside a material through a depth profile. Today, SIMS is extensively used to characterize impurity and dopant level analysis for multi-layered structures due to its excellent detection levels and high spatial resolutions. It is important to emphasize that, SIMS profiling provides concentration values of the atomic dopants -not the electrical carrier concentration- across a depth profile.

The working principle of SIMS is briefly as follows. A sample surface is bombarded with a precisely focused energetic primary ion beam (generally has a kinetic energy between 1 to 30 keV) generated by an ion gun. During the bombardment of these primary ions, an energetic cascade of collisions occurs within the upper layers of the surface. This energy dissipation leads to the breaking of bonds and the emission of secondary particles (mostly in the range of a few monolayers from the surface). Most of the emitted particles are neutral, while a small fraction (less than 1%) carries a positive or negative charge, making them of interest for the

SIMS technique. Depending on the electric field strength applied between the extractor and the sample, these charged particles can be analyzed based on their atomic mass by a mass spectrometer. The output of a SIMS analysis can be a mass spectrum, depth profile and image. The depth profiling information (with resolution down to 1-2 nm) is extracted by recording the secondary ion emission with respect to the sputtering time of the sample. All the process takes place under ultra-high vacuum (UHV) conditions. A schematic representation of SIMS system showing the processing of signal to obtain various analytical results is shown in Figure 3.4. For more in-depth information, please refer to the references [98–100].

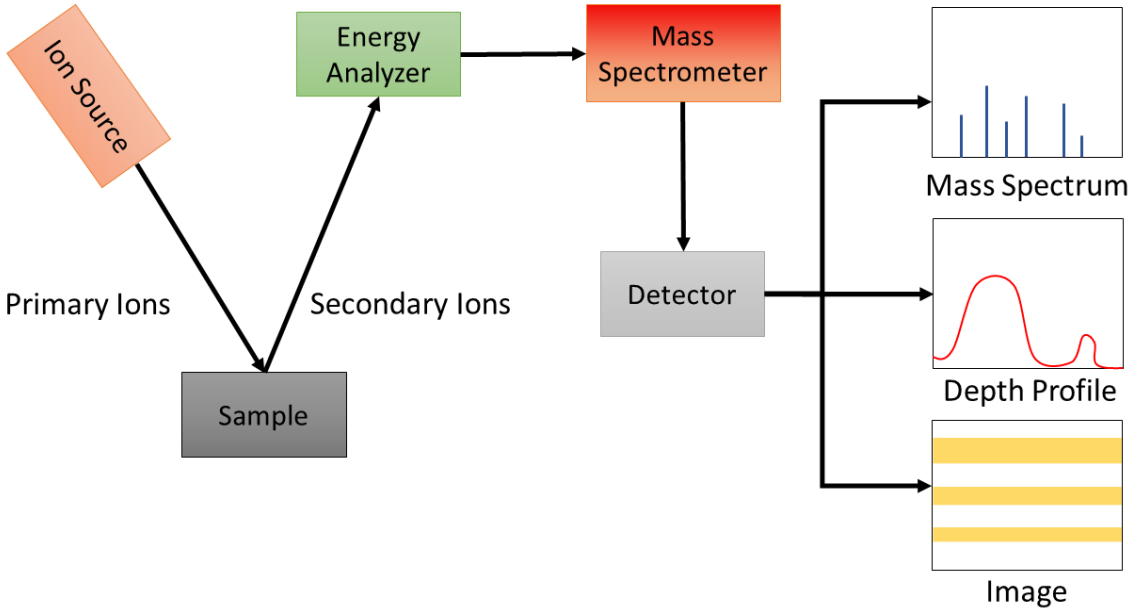


FIGURE 3.4: A schematic representation of sequence diagram of the Secondary Ion Mass Spectrometry (SIMS) technique (adapted from [100])

SIMS measurements were vital for this research, serving as the primary basis and cornerstone for much of the analysis conducted. These measurements were performed by the SIMS expert Dr. Paweł P. Michałowski at Łukasiewicz Research Network Institute of Microelectronics and Photonics based in Warsaw, Poland with the CAMECA IMS SC Ultra instrument.

There are three main SIMS modes conducted in this research: these are denoted as Zn(Class), Zn(lowV) and Zn(ULIE) in the following chapters where the relevant experimental details are discussed. We will compare results obtained by these three approaches and show that different information can be obtained from the different SIMS scanning methodologies.

The Zn signal during SIMS of III-V materials can be obtained by different measurement protocols. The adapted industrial approach relies on sputtering with Cs+ ions and detecting $CsZn^+$ secondary ion signal [78, 101]. This approach (denoted as Zn(Class)) provides relatively

high-count rates and fast scanning capabilities. However, it is important to note that the exact mechanism governing the formation and ionization of this complex ion has not been fully understood, despite a consensus that the sputtering and ionization processes are independent [102, 103].

Here, it is worth mentioning that, in most SIMS experiments, typically, the applied voltage to the sample holder is relatively high, often reaching several kilovolts. Yet, its influence on the ionization probability of $CsZn^+$ remains largely unexplored, potentially differing for layers with differing conductivity. Lowering the voltage presents challenges in the formation of secondary beam, particularly when detecting multiple species. Recently, Michałowski at al. demonstrated a novel approach that the extraction of secondary ions can be performed separately for each measured species during the measurement [104]. This approach enables the measurement of $CsZn^+$ secondary ions at significantly reduced voltages, below 0.5 kilovolts, thereby circumventing potential measurement artifacts associated with the classical approach. This measurement method is SIMS method of choice for this research. When comparing with the other methods, Zn(lowV) notation will be used. Otherwise, it will be denoted as Zn.

It has also been established that using ultra-low impact energies (ULIE) in SIMS allows probing the chemical state during the experiment. A complex ion can be extracted only if the atoms were bonded prior to the experiment [105, 106]. For zinc (Zn) atoms to be active p-type dopants, they must substitute the III-group sites within an A(III)-B(V) lattice and bind with V-group elements. Therefore, ULIE-SIMS measurements targeting ZnP_3 (for Zn doped InP) complex ion provide information specifically into the active part of the total Zn incorporated into the material. This measurement is denoted as Zn(ULIE).

Cs+ primary ions with the impact energy of 150 eV and the beam intensity of 6 nA were used as primary beam in all three modes. For the Zn(Class) approach the voltage applied to the sample holder and the accelerator was 5 kV and 5.15 kV, respectively. For the Zn(lowV) they were reduced to 200 V and 350 V, respectively and the extraction of each measured species was optimized separately for each signal [104]. Zn(ULIE) used the same settings a Zn(lowV) but a complex ZnP_3 signal was monitored. Typically, atoms can be analyzed down to the values 10^{15}-10^{16} cm^{-3} or even below depending on the element type and measurement settings. For this research, in some cases, a faster scan is conducted to be able to get a better resolution down to density (per cubic centimeter) in the 10^{15} range. For the fast scan, the conditions were the same as for the Zn(lowV) but the beam intensity was increased to 40 nA which resulted in

a much higher etching rate.

3.2.1.2 Capacitance-Voltage Measurement

The capacitance-voltage (C-V) measurements or profiling are usually performed to analyse the carrier density of a semiconductor whose structure is in a capacitance form. The C-V technique relies on that, in reverse bias conditions, the width (W) of the depletion region (or space-charge region (scr)) of a semiconductor junction device depends on the applied voltage [107].

Considering the Schottky barrier diode of Figure 3.5, the relation between capacitance and doping concentration can be derived as follows: A dc bias V applied to a p-type semiconductor with doping concentration N_a produces a depletion region of W. The capacitance is then defined as

$$C = -\frac{dQ_S}{dV} = \frac{dQ_m}{dV}, \tag{3.1}$$

where Q_S and Q_m are the charge in semiconductor and metal, respectively. Here, the negative sign indicates that, when the applied reverse bias (V) is increased, more negative ionized acceptors are generated. The depletion region can be extended further into the semiconductor by adding a small positive ac bias (typically with a frequency between 10 kHz to 1 MHz and an amplitude between 10 to 20 mV).

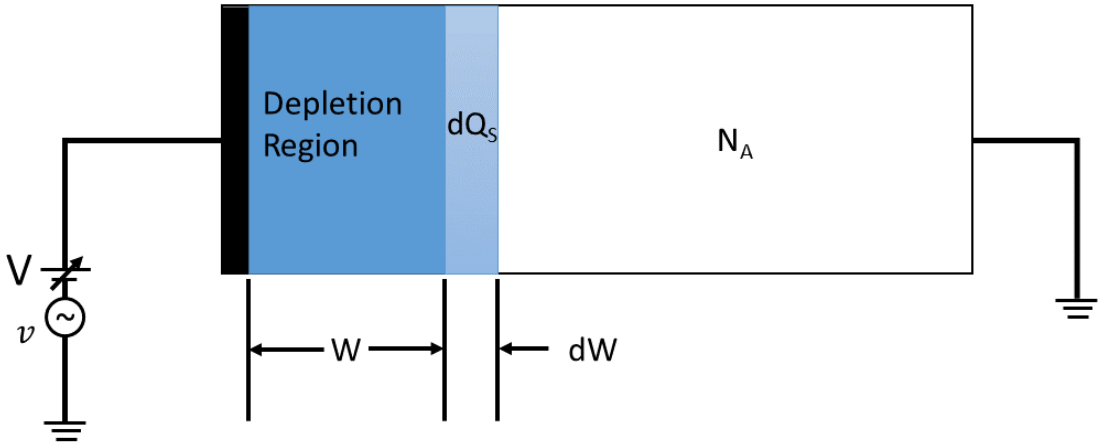


FIGURE 3.5: A schematic illustration of a reverse-biased Schottky diode.

Here let's assume that the diode is under a DC voltage bias V with a sinusoidal AC voltage v, where the AC voltage gradually increases from zero to a small positive voltage, introducing an incremental charge dQ_m to the metal contact. For charge neutrality, this added charge dQ_m is then to be balanced by an equal semiconductor charge increment dQ_S. The semiconductor

charge can be written as

$$Q_S = qA\int_0^w (p - n + N_D^+ - N_A^-)dx \approx -qA\int_0^W N_A dx \tag{3.2}$$

based on the approximation that all acceptors are ionized and for the depletion approximation $N_D = 0$ and $p \approx n \approx 0$.

The charge increment dQ_S can be rewritten as

$$C = -\frac{dQ_S}{dV} = qA\frac{d}{dV}\int_0^W N_A\, dx = qAN_A(W)\frac{dW}{dV}. \tag{3.3}$$

The capacitance of a parallel plate capacitor is given by

$$C = \frac{\varepsilon_0\varepsilon_r A}{W}. \tag{3.4}$$

Differentiating Equation 3.4 with respect to voltage and substituting dW/dV into Equation 3.3 gives

$$N_A(W) = \frac{2}{q\varepsilon_0\varepsilon_r A^2\frac{dC}{dV}} = \frac{2}{q\varepsilon_0\varepsilon_r A^2\frac{d(C^{-2})}{dV}} \tag{3.5}$$

using the identity $d(1/C^2)/dV = (2/C^3)dC/dV$.

Note that from Equation 3.4, the depletion width can be written as follows [108]:

$$W = \frac{\varepsilon_0\varepsilon_r A}{C}. \tag{3.6}$$

For the C-V analysis, a device structure is fabricated from the epi-structure, InP:Si (100 nm)/InP NUD (500 nm)/InP:Zn (200 nm). This epi structure, depicted in Figure 3.6a, is grown on a Zn-doped nominally perfectly oriented (100±0.1°) substrate at a thermocouple temperature of 715°C, V/III (PH_3/In) ratio of 380, and a growth rate of 1 µm/h. 1 mm diameter circular diodes were fabricated on the MOVPE grown wafer stack shown in Figure 3.6b using photolithography and wet etching in HCl:H_3PO_4 1:4 solution. The metal contacts were fabricated using metal lift-off of 35 nm Ti, 350 nm Au on PMGI SF11/AZ5214E for the top side, and the same metal stack was used for the backside. C-V measurements were performed on a cascade prober with an Agilent E4980 LCR meter, using a reverse bias voltage range from 0 to -20 V, with an AC current of 1 MHz and amplitude of 25 mV. The reverse bias sweeps were performed in steps of -20 mV. Using the extracted C-V data, we used the Mott-Schottky

analysis to extract the Zn doping profile using Equation 3.5 and Equation 3.6, where W is the depletion region width, ε_r is the relative permittivity (12.5 for InP), and C is the associated capacitance, q is the electron charge, and A is the device area.

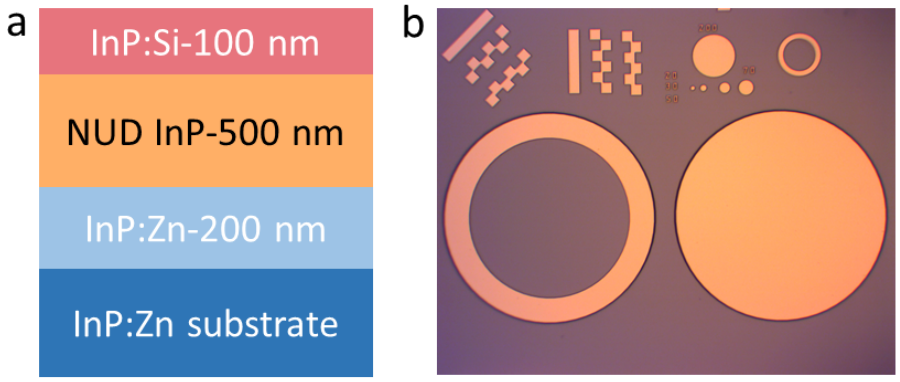


FIGURE 3.6: a) Schematic of of InP:Si/InP/InP:Zn layers grown on a nominally perfectly oriented Zn doped substrate for C-V purposes b) Optical microscope image of C-V measurement diodes. The bottom right device has a 1 mm diameter and used for C-V measurements.

3.2.1.3 Electrochemical Capacitance-Voltage Profiling

Standard SIMS data typically offers information about the overall dopant concentration, while C-V measurement profiling has a limitation regarding the accessible depth especially for highly doped materials [108]. However, there are times when the information about the carrier concentration is necessary, specifically the extent in which these dopants are active for a multi-layered structure. In such scenarios, electrochemical capacitance-voltage profiling (ECV) Profiling proves to be a good option [109]. The measurement principle of ECV is conceptually similar to that of the typical C-V technique, with the key difference being the use of an electrolyte instead of a metal contact to establish the Schottky contact with the semiconductor. Unlike C-V measurements, ECV offers an etching capability with an appropriate electrolyte, enabling nearly unlimited depth profiling. The etch process and measurement are combined into one operation. Depth profiling is simply achieved by repeating C-V measurements after every etching step of the contact area. Thus, it is a destructive technique, leaving a crater on the sample surface.

During an ECV measurement, both p-type and n-type carrier concentration can be characterized. In the case of p-type doping, holes are conducted from the semiconductor contact to the surface. Upon reaching the surface, these holes may release valence electrons of p-type from the semiconductor surface atoms through recombination. If all valance electrons of a semiconductor

atom are removed, the positively ionized atom core dissolves into the electrolyte.

On the other hand, for n-type doping, light can be used to create electron-hole pairs at the surface of the semiconductor. If these holes diffuse to the surface, supported by the intrinsic electrical field of the semiconductor/electrolyte interface, they may release valence atoms of the n-type from semiconductor surface atoms by recombination. Meanwhile, the electrons are conducted to the semiconductor contact. Similar to p-type doping, if all valence electrons of a semiconductor atom are removed, the positively ionized atom core dissolves into the electrolyte fluid.

In this research, the Wafer Profiler CVP21 tool is used to measure the carrier concentration profiles by ECV profiling technique. An ED:EDTA 0.1M -which is a mixture of 220 ml of deionized water, 8.4 g of ethylenediamine disodium (EDTA) and 5 ml of ethylenediamine (ED) 99%- electrolyte is used.

3.2.1.4 Scanning Spreading Resistance Microscopy (SSRM)

Scanning spreading resistance microscop (SSRM) emerged as a two-dimensional (2D) electrical characterization technique based on atomic force microscopy. It is especially advantageous for devices with non-classical geometry requiring information into dopant distribution across more than one dimension. It can be also very "local" (when performed with a very fine tip), sensitive to interfaces and especially useful for measuring multi-junction devices [110].

The spreading resistance is measured by scanning the AFM tip under a high force (μN) across a semiconductor sample while applying a DC bias between the probe and the sample. The use of the high forces is essential to minimise probe contact resistance and decrease measurement noise, thereby making spreading resistance predominant in the total measured resistance. A typical SSRM setup is illustrated in Figure 3.7. A logarithmic amplifier is used to achieve a broad dynamic range for the measured current, enabling the analysis of a wide range of resistances (or doping concentrations) in a single measurement. At the end, a 2D map of the local spreading resistance is generated; offering spatial resolution determined by the tip's radius (can be less than 10 nm).

The readout of SSRM results is in log(ohm). Extracting the dopant profile from an SSRM analysis requires accurate calibrations through ad-hoc test samples and an appropriate quantification modelling [111, 112].

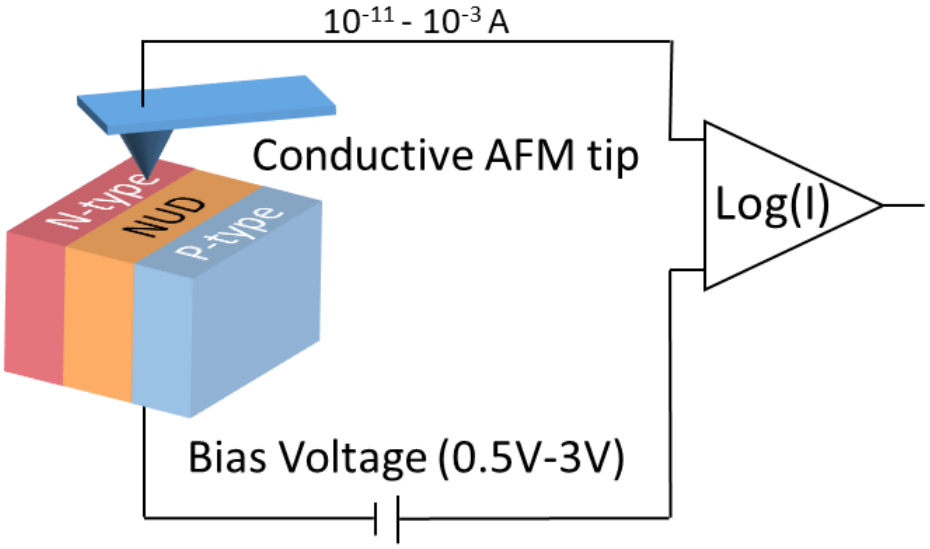


FIGURE 3.7: A schematic layout of a Scanning Spreading Resistance Microscopy (SSRM) setup

SSRM measurements were performed on a Bruker Atomic Force Microscope (AFM) – Dimension Icon with conductive AFM diamond tips (AD-40-AS - Adama). The samples are freshly cleaved before the measurement. A ≈300nm oxide was deposited on top of the layers before cleaving to protect the tip from falling from the edge of the sample cross-section. In the context of our research, the results did not deliver precisely quantified quantities, but only qualitatively reproducible result. For this research we only needed qualitative comparisons, and the technology delivered useful insights.

3.2.2 Material Characterization

3.2.2.1 Atomic Force Microscopy (AFM)

Atomic force microscopy (AFM) is the leading scanning probe microscopy technique with its much broader application areas giving a 3D nanoscale profiling of a surface. It operates by scanning a sharp tip (typically ≤10 nm) over the sample surface while measuring the interaction forces between the tip and the surface atoms or molecules of the sample [113]. The tip is mounted on a flexible cantilever, allowing it to move up and down in response to the forces acting on it. Interactions between the tip and the surface can lead to either attractive or repulsive forces, causing the cantilever to bend either positively or negatively if in contact, and to modify its resonance frequency when operated in *"non–contact"* mode. A position-sensitive photodetector, using a laser beam reflected from the backside of the cantilever, detects either the bendings, or

the change in resonant frequency. As the tip scans across the sample surface, it maintains a constant force/oscillation between itself and the surface by adjusting its height. Any movement of the cantilever, i.e. any features of the surface, alters the position of the reflected laser beam on the photodetector, allowing precise measurement of the cantilever deflection/change of resonances. By analysing the feedback data, AFM can generate detailed images of the surface features with atomic height resolution.

The samples are scanned, unless specified otherwise, with a silicon tip mounted on an aluminium-coated cantilever with a radius of $\leq$7 nm, a nominal resonance frequency of $\approx$70 KHz and a spring constant of 2 N/m (OLYMPUS OMCL-AC240TS). Unless stated otherwise, all AFM scans for this research are taken on a MultiMode AFM with a Veeco Nanoscope V control system in tapping mode or non-contact mode. A detailed description of the working principles of AFM in the tapping mode and more can be found in Voigtländer's book [114].

3.2.2.2 High-Resolution X-ray Diffraction (HRXRD)

High-resolution X-ray diffraction (HRXRD) is crucial for examining chemical composition, strain, defect density, and layer thickness. A typical setup involves an X-ray source emitting a wide spectrum beam, which is then refined by a monochromator. The refined beam interacts with the sample, and the resulting reflection is detected.

Diffraction occurs when specific phase relations are present among two or more waves (Bragg condition). This phenomenon emerges when an electromagnetic wave interacts with a periodic structure whose spacing closely matches the wavelength of the wave. In-phase waves lead to constructive interference while out-of-phase waves undergo destructive interference, cancelling each other. Analysis of the position, intensity, and width of diffraction peaks provides insights into the sample's structural properties.

XRD is a non-destructive method and can be applied in several forms depending on the material property to be examined. In this research we mostly used (1) X-ray rocking curves to measure the chemical composition, and when necessary (2) reciprocal space mapping (RSM) to analyse the amount of built-in compressive or tensile strain or relaxation of the films. In the rocking curve mode, the sample is rotated while the intensity of the diffracted X-rays is measured at various angles. For the reciprocal space maps, a full scan covering a range of angles and different Bragg conditions is often performed. HRXRD measurements were carried out in an X'Pert MRD system using Cu Kα_1 radiation with a wavelength of 1.54056Å.

3.2.3 Optical Characterization

3.2.3.1 Micro Photoluminance (μPL) Measurement

Photoluminance (PL) is an extensively used optical evaluation method for III-V semiconductors and their alloys, providing information on bandgap (E_g) as well as the impurity and defect states of the material.

In this thesis, μPL measurements are used for three purposes: (1) Gathering information about the Zn incorporation status of InP layers, (2) understanding the pureness of AlGaAs layers grown with and without a surfactant (TMSb) and (3) extracting the bandgap of ternary and quaternary alloys to analyze the crystal composition whenever needed.

The μPL measurements for this research were performed by Dr. John O'Hara in Quantum Optics Lab of Tyndall National Institute. In all cases, the PL resulted from above-band (2 eV) laser excitation, focused on the sample surface within either a 5 μm^2 or 20 μm^2 spot area. The spectra were obtained with 300 and 950 l/mm gratings and nitrogen-cooled Si CCD and InGaAs arrays. For low-temperature PL the samples were cooled in a closed-cycle Helium cryostat to around 10 K.

Chapter 4

Zn Concentration Profile of III-V Materials

In this chapter, the Zn dopant behaviour and its incorporation properties in III-V material structures are investigated. Firstly, the (asymmetric) Zn concentration profile of InP layers and other III-V materials, such as GaAs, InGaAs, AlInAs are examined, employing different SIMS scanning methodologies. Moreover, the electrical properties of Zn as a dopant in InP is examined, and this is followed by a solution to stop Zn diffusion. We also address Zn "back diffusion" across different substrates with a 0.4° misoriented towards (111)A and (111)B direction. In the last section, for completeness and comparison with the literature, PL measurements' results are investigated in doped layers, as well as in subsequent epitaxial layers.

Overall, we found with strong and systematic evidence that Zn behaves like a surfactant accumulating on the sample surface and gradually incorporate into the material even after we shut off the Zn source.

4.1 Asymmetric Zn concentration profile in III-V phosphide and arsenide layers

In this section, we will compare Zn concentration profile results obtained by three SIMS measurement approaches and discuss the different information obtained from these SIMS methodologies. In summary, the preferred measurement method for this research is the Zn(lowV). This notation is specifically used when comparing data with other methodologies; otherwise, it's

here simply denoted as Zn. The Zn(ULIE) method gives information about the ion complexes, i.e. ZnP_3 count for InP, which represents the active portion of the total Zn incorporated into the material. Conversely, the Zn(Class) approach, which is a broadly utilized industrial and academic approach, is only here conducted when comparing with the other methods, as this methodology has limited reliability for layers with different conductivity (See Chapter 3.2.1.1 for more comprehensive description for utilized SIMS methodologies).

To investigate the Zn diffusion behaviour in forward ('*forward-diffusion*') and backward ('*back-diffusion*') direction, we grew epitaxially a simple test structure by MOVPE. Here, the term "forward" refers to the direction of epitaxial growth, while "backward" denotes the opposite direction, toward the semiconductor substrate. This test structure features either a 200 nm or 500 nm layer of Zn-doped InP sandwiched between two nominally undoped (NUD) layers. The thickness of the top layer varied, ranging from a few hundred nanometres to 2000 nm, depending on the specific sample. Surprisingly, except for maybe Ref. [56], there are not many reports in the literature analysing comparable sample structures.

The samples are grown on InP semi-insulating and nominally perfectly oriented substrates (100±0.05°) at low pressure (80 mbar) by using purified N_2 as carrier gas at a thermocouple temperature of 715°C. The growth rate of InP was 0.91 μm/h and V/III (PH_3/In) ratio was 380. The ratio of PH_3/DEZn is 11600, and Zn/In ratio was 3.26%.

It is important to acknowledge that, our data does not allow us to distinguish the effects as arising from atomic Zn or its precursor. Therefore, in the subsequent discussions, 'Zn diffusion' will refer to both possibilities whenever a surfactant effect or other surface effects are involved.

Figure 4.1a shows the SIMS profile of InP(200 nm)/InP:Zn(200 nm)/InP(2 μm) (respectively from bottom to top) layers measured with the *Zn(lowV) methodology*. The oxygen (O) spike acts as a marker and indicates the InP substrate surface, or better the substrate/growth buffer interface. The zero nm on the x-axis of the SIMS graph shows the sample surface and the dotted lines (A-B) indicate the nominal boundaries between the Zn doped and NUD layers. Zn exhibits a surprising asymmetric dopant concentration profile and appears for ≈1500 nm, a shockingly long distance, into the NUD layer in the growth direction. Also, Zn concentration increases abruptly, for a ≈15nm narrow peak or so approximately corresponding to the Zn shut off region, at the interface between the doped and top NUD InP layer (Figure 4.1a, point A). The possibility of SIMS artefacts was investigated and excluded. The feature is reproducible across different samples, even if presently we do not have an explanation for its origin. Figure 4.1b

shows a similar Zn concentration profile for a different sample with the InP(200 nm)/InP:Zn(200 nm)/InP(500 nm) layers, again measured with the Zn(lowV) methodology. The sample in Figure 4.1b and the sample in Figure 4.1a have "diffusion times" (i.e. the interval between the moment after the Zn source is turned-on and end of the growth) of 1967 seconds and 7870 seconds, respectively.

Figure 4.1d shows the "shut-off" peak concentration comparison for the two samples. The x-axis was shifted so that the interface peaks coincide with each other for an easier comparison. A quantitative conclusion should not be drawn immediately because for such a narrow peak SIMS concentration calibration may not be accurate. However, it is clear that the full-width-half-maximum (FWHM) of the sample with the longer diffusion time (thicker cap layer) is wider, indicating that the peak itself is also diffusing.

The inset in Figure 4.1a shows a 'fast' SIMS measurement scan of the same structure also conducted with Zn(lowV) (again, more details on the measurement can be found in Chapter 3.2.1.1). The slow measurement has a very good depth resolution; however, it is not sensitive enough for the Zn concentration values below 1x10^{16} atoms/cm^3. Consequently, concentrations in this range are inaccurately measured under the "slow" methodology, leading to a decay rate faster than expected. In the low concentration regime, the curve is more correctly determined by a "fast" scan, which, on the other hand, is not accurate in the high concentration regions. The combination of fast and slow scans presented in Figure 4.1a form an exponential curve (i.e., a simple straight line in the log scale of the graphs). This suggests the presence of a Zn reservoir, contributing to the asymmetric forward Zn profile. A reservoir subject to consumption over time would typically exhibit an exponential decay pattern, as commonly discussed in physics textbooks. Importantly, this phenomenon cannot be solely attributed to simple diffusion within the InP matrix. Indeed, the observed concave curve or function (better visible in linear scale obviously) is in contradiction with conventional diffusion processes, which typically yield a convex profile [70].

It is important to emphasize that the samples are not oversaturated with Zn flow, Zn doping values are actually kept close to the saturation levels or below. We observed similar asymmetric curves and the interface peak at lower Zn concentration values. Figure 4.1c shows the total Zn concentration levels measured with the Zn(lowV) methodology for the InP(200 nm)/InP:Zn(500 nm)/InP(500 nm) layers. In this case, the Zn flow during doped layer growth is reduced by a factor of 10 compared to the samples in Figure 4.1a and Figure 4.1b and the thickness of

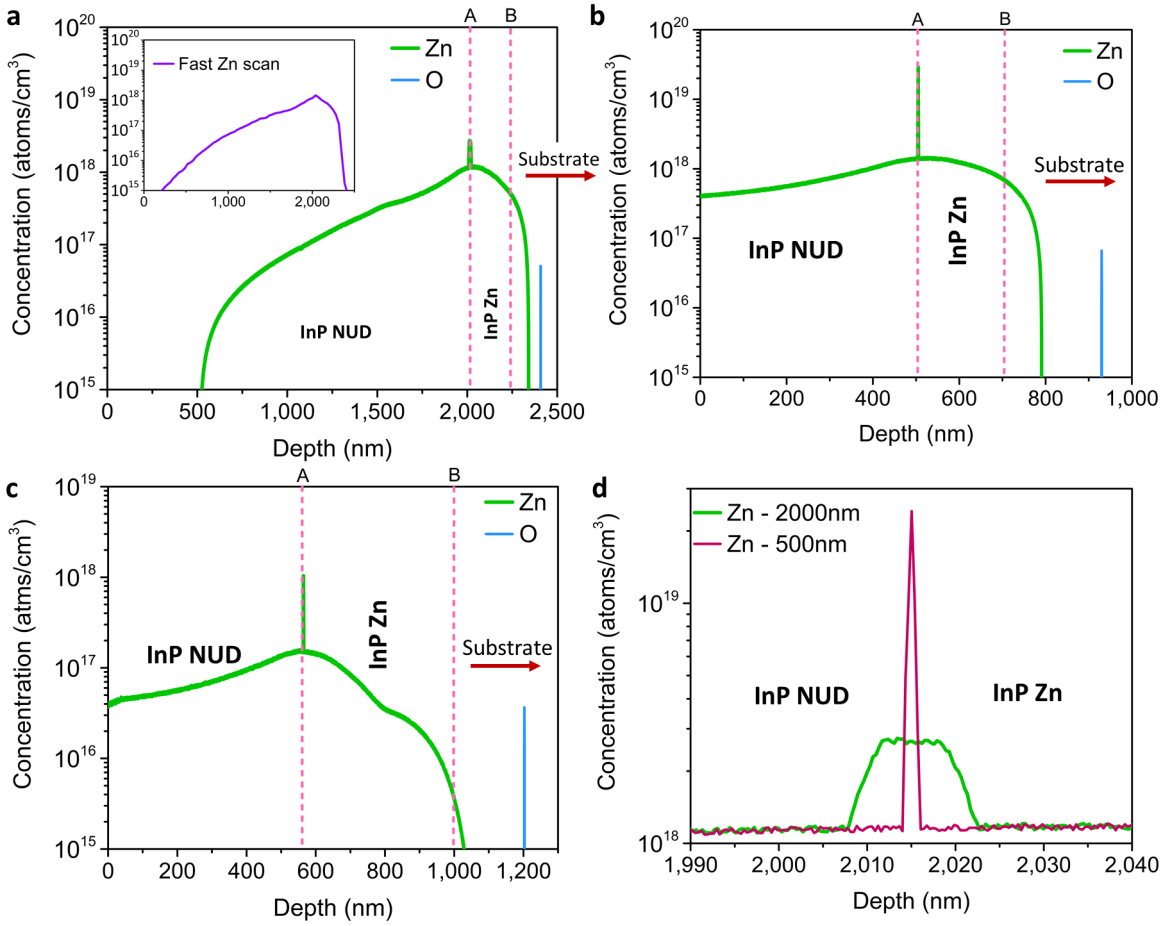


FIGURE 4.1: Measured SIMS profile of Zn concentration of MOVPE grown InP epitaxial layers. The substrate choices for these samples were nominally perfectly oriented Fe doped InP wafers. a) Total Zn concentration levels measured with the Zn(lowV) method of the InP(200 nm)/InP:Zn(200 nm)/InP(2 μm) (from bottom to top) layers. The inset figure shows SIMS measurement of the same sample with a faster scan, which allows a better resolution of the low concentration. b) Total Zn concentration levels measured with the Zn(lowV) method of the InP(200 nm)/InP:Zn(200 nm)/InP(500 nm) layers. c) Total Zn concentration levels measured with the Zn(lowV) method of the InP(200 nm)/InP:Zn(500 nm)/InP(500 nm) layers. The Zn flow during the doped layer growth is 10 times lower than the samples in (a) and (b). For (a), (b) and (c), zero nm on the x axis in the depth profiles is the final sample surface. The oxygen peak marks the sample substrate-to-epitaxial layer interface. The dotted lines (A-B) indicates the nominal boundaries between the Zn doped and nominally undoped (NUD) layers. The peak in the Zn profile at point A, at the interface between the intentionally doped/not doped interface is a real effect. d) A zoomed-in comparison of the peak concentration and shape of the samples in (a) and (b). The x-axis is shifted so the samples are aligned at the interface.

the Zn doped layer is increased to 500 nm (refer to Chapter 4.4 for another example of lower Zn doping concentration). Although a linear relationship between the dopant source and the incorporated doping concentration is typically expected, this is not always observed. The Zn doping concentration starts below 10^{16} and gradually increases above 10^{17}. A similar peak to those in Figure 4.1a and Figure 4.1b at approximately 500 nm depth (the expected place between NUD and doped layer), is observed. The doping concentration increases by a different

rate in the regions between 500 nm to 800 nm and 800 nm to 1000 nm and there is a "flattening" in the Zn concentration profile around 800 nm depth.

Figure 4.2b presents a comparison of SIMS data obtained from three different Zn scanning methods (see Chapter 3.2.1.1). The noticeable observation is the distinct behaviour of the Zn(lowV) profile, while the other two strongly diverge. The Zn(ULIE) profile exhibits minimal forward diffusion, and quickly decays with a convex profile outside the intentionally doped region symmetrically similar to the expected back diffusion profile.

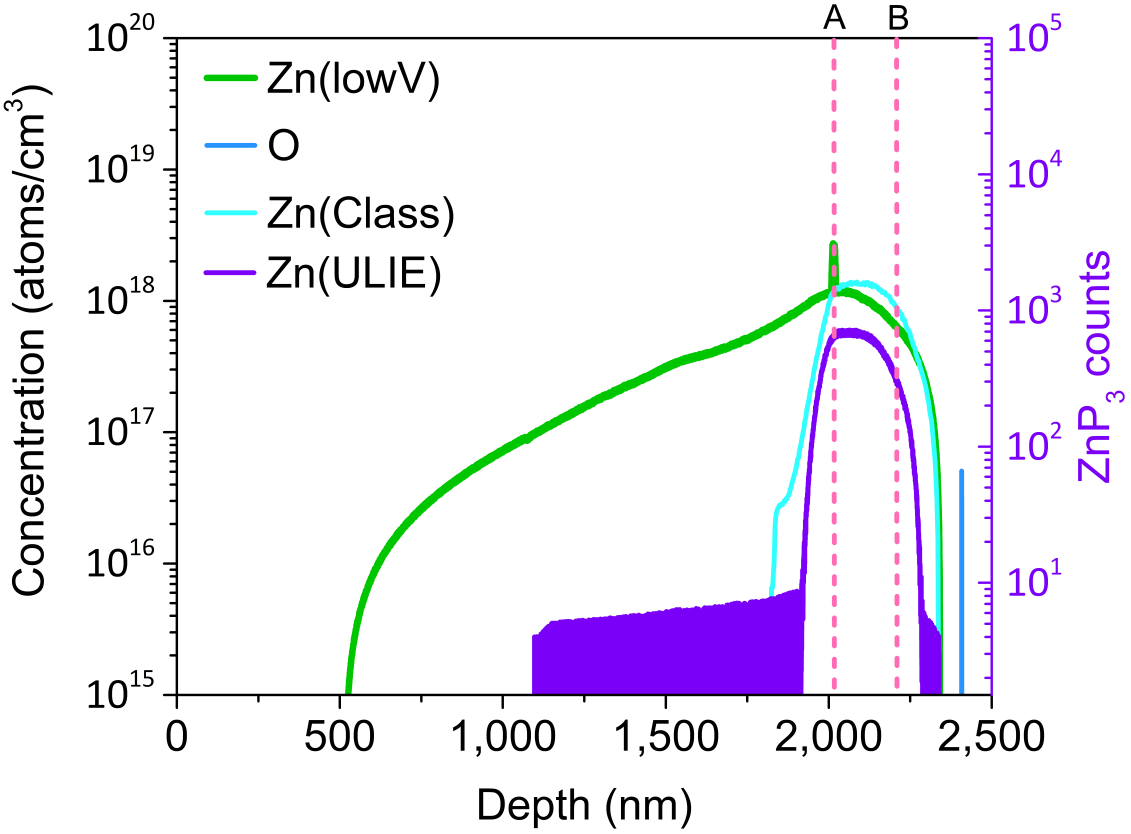


FIGURE 4.2: Comparison of the three different Zn methodologies applied on the sample shown in Figure 4.1a. The total Zn profile measured with Zn(lowV) (left x-axis) and the conventional Zn(Class) methodology (left x-axis). Zn(ULIE) measures the ZnP_3 complex ion (right x-axis).

In contrast, the Zn(Class) shows a rapid exponential decay, some maintaining an asymmetric pattern, but with a significantly faster decay. Noticeably, this discrepancy highlights sensitivity of each method to different forms of Zn species incorporated in the InP matrix. Specifically, one could expect the three techniques to be sensitive differently to substitutional Zn (i.e. zinc sitting on the indium atom location in the zincblende lattice and effectively doping), and other forms of incorporation (e.g. interstitial or forming a defect complex of another nature) [29].

Results from Ref. 106, which are limited to fully doped layers, suggest that Zn(ULIE) should correlate with the doping profile, leaving the Zn(lowV) to be measuring the sum of all other all other species and possibilities (including the active doping ones).

In MOVPE, 'reactor memory effect' refers to the phenomenon where remnants of previous growth processes persist in the reactor environment and effect subsequent growth runs. To, in general, understand the processes involved, and also to check and exclude the possibility of reactor memory effects from consideration, we have systematically grown comparable test structures with different material systems. Figure 4.3a and Figure 4.3b show the total Zn concentration levels measured via the Zn(lowV) method in two different semiconductor layer configurations: GaAs(200 nm)/GaAs:Zn(200 nm)/GaAs(500 nm) and InGaAs(200 nm)/InGaAs:Zn(200 nm)/InGaAs(500 nm), respectively. Notably, a consistent "faster" trend of exponential decay in forward-diffusion is observed for arsenides. This decay typically resolves at around 200 nm, a significantly shorter distance compared to our observations in InP layers.

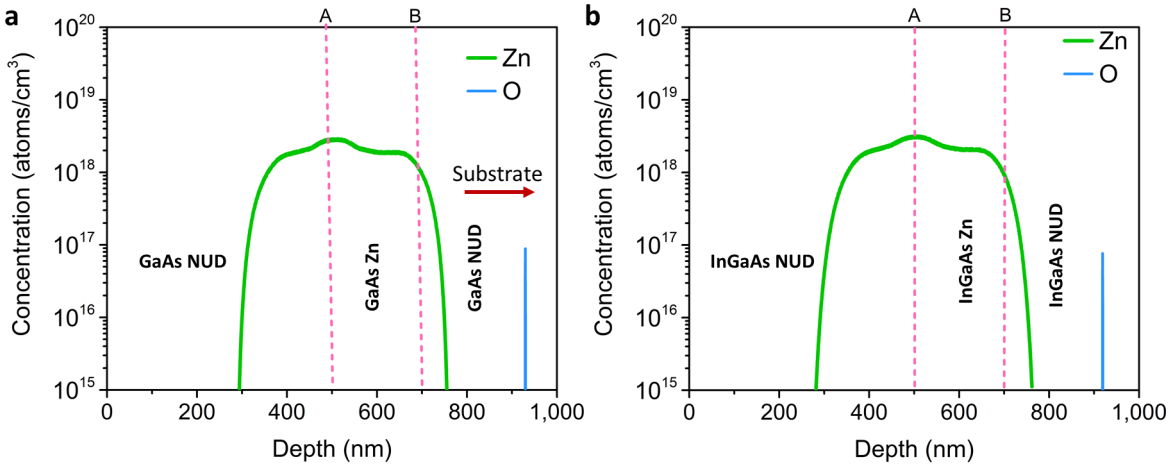


FIGURE 4.3: a) Total Zn concentration levels measured with the Zn(lowV) method of the GaAs(200 nm)/GaAs:Zn(200 nm)/GaAs(500 nm) (from bottom to top) layers. b) Total Zn concentration levels measured with the Zn(lowV) method of the InGaAs(200 nm)/InGaAs:Zn(200 nm)/InGaAs(500 nm) layers.

The observed Zn dopant profile in InP and other III-V materials, as well as our subsequent findings detailed in the following sections and Chapter 5, suggest that Zn precursors, either intact or partially decomposed, or atomic Zn accumulate on the sample surface during the growth of doped layer. This accumulated surface Zn, behaves like a Zn source and continue to incorporate into the epi-layers even after the Zn source has been shut off (instead of completely desorbing from the surface and ending into the exhaust). Moreover, the dependence of the different forward-diffusion lengths on the material system, suggest this to be a "material" related property, and not a reactor memory effect (such as, e.g. wall saturation and re-evaporation

which would largely be expected to be similar from run to run). To test this hypothesis further, we conducted a series of experiments in the following sections.

4.1.1 Switching from AsH_3 to PH_3

The active regions of many optical device structures on InP substrates mostly require the use of arsenide-based alloys such as InGaAs, AlInAs and/or AlInGaAs. In order to see the behavior of 'forward-diffusion' of Zn in these arsenide-based structures; we grew lattice matched InGaAs and AlInAs after Zn-doped InP layers. The SIMS results show a similar behaviour for InGaAs (Figure 4.4a) and AlInAs (Figure 4.5a). Zn is observed approximately 350 nm deeper into the NUD InGaAs and AlInAs layers before sharply decreasing. Additionally, the AlInAs layer exhibits an oxygen background of ≈7x10^{16} atoms/cm^3 in the AlInAs layer, which is typical for MOVPE grown aluminium-containing alloys [115]. A notable observation when comparing the Zn forward diffusion behaviors depicted in Figure 4.4b is that the Zn carry-over length is slightly longer (approximately 150 nm) when the Zn-doped layer is InP-based. It again indicates the material dependent surfactant behavior, i.e. Zn likes to accumulate more in InP than InGaAs.

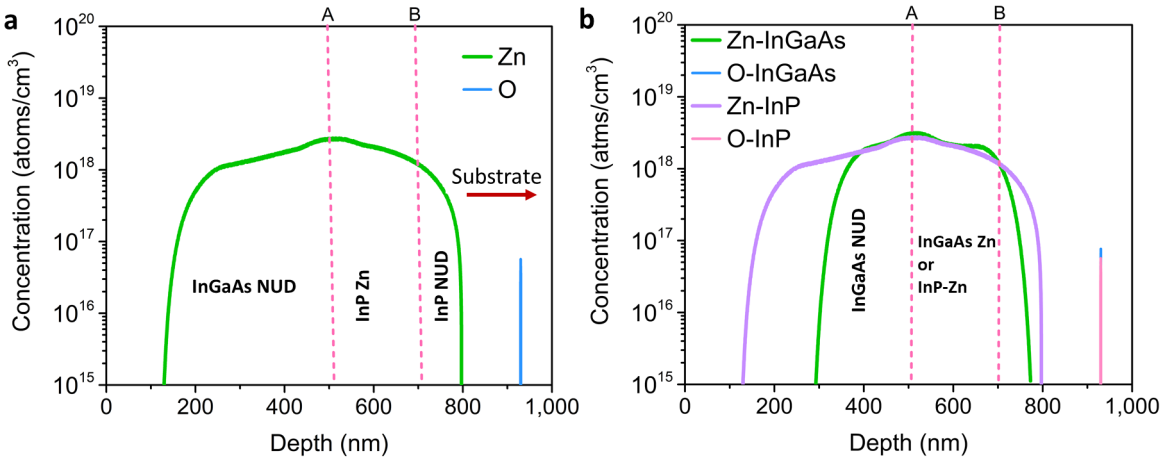


FIGURE 4.4: Differences in post growth tailing when switching from PH_3 to AsH_3. a) Measured SIMS profile of Zn concentration levels of InP(200 nm)/ InP:Zn(200nm)/ InGaAs(500 nm) (from bottom to top) epitaxial layers grown on nominally perfectly oriented InP wafer b) Comparing the Zn concentration profile of samples (a) and Figure 4.3b where the doped layer is InP or InGaAs. The Zn forward diffusion length is slightly longer (approximately 150 nm) when the Zn-doped layer is InP-based.

To further investigate the differences in Zn concentration between arsenic and phosphorus-based structures, we fabricated a similar structure using a different phosphorus alloy: InGaP(200 nm)/Zn:InGaP(200 nm)/InGaP(1 μm) on 0.2° misoriented towards (111)A crystallographic

plane GaAs wafer. The SIMS profile of this structure (Figure 4.5b) reveals a remarkably extended Zn post-growth tailing, exceeding 1000 nm, similar to that observed in InP. This suggests that the prolonged post-growth tailing is associated with phosphorus alloys, while arsenic-containing layers exhibit a diminished effect (even if still substantial). We observe again, that it is important to note that our data cannot distinguish whether this effect originates from differences in growth precursors (arsine vs phosphine) or simply variations in surface bonds (As vs P).

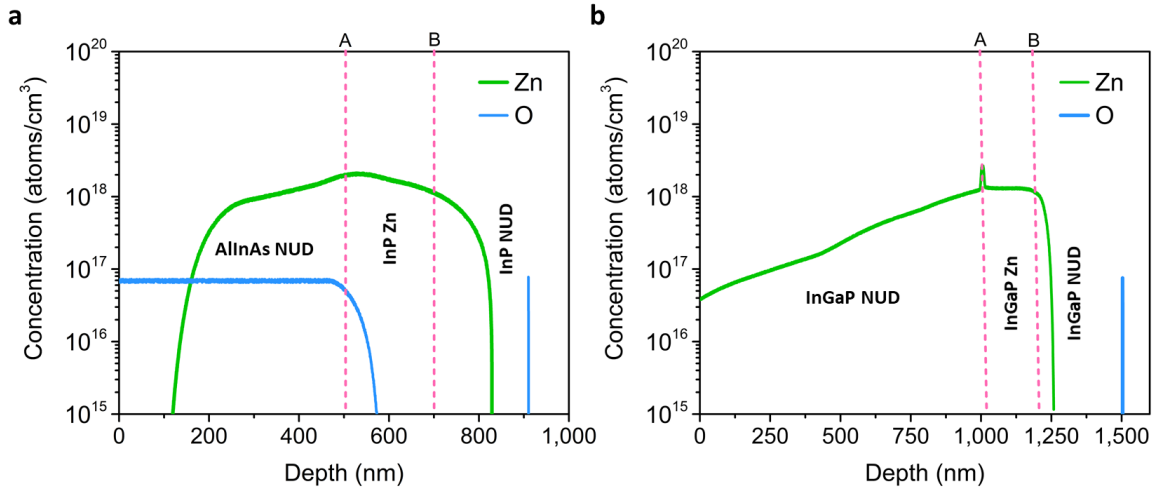


FIGURE 4.5: Measured SIMS profile of Zn concentration levels of a) InP (200nm)/InP:Zn (200 nm)/AlInAs (500 nm) epitaxial layers grown on nominally perfectly oriented InP wafer. b) InGaP (1 μm)/InGaP:Zn (200 nm)/InGaP (200 nm) grown on 0.2° misoriented towards (111)A crystallographic plane GaAs wafer.

4.2 Electrical characterization of Zn as a dopant

To investigate further the incorporation and ionization characteristics of Zn, particularly within the forward-diffusion region in the top NUD layer, we conducted analyses using SSRM, ECV profiling, and C-V Measurements (refer to Chapter 3 for more information). Specifically, we aimed to further analyse our findings with the Zn(ULIE) SIMS methodology discussed previously and shown in Figure 4.2, indicating that the Zn in the top NUD layer could not be substitutional and thus electrically inactive. Through this section, all the results are produced from InP:Zn(200 nm)/InP NUD(500 nm)/ InP:Si(100 nm) (from bottom to top) epi layers grown on a Zn doped (1-3x10^{18} cm^{-3}) perfectly oriented (100 ±0.1°) substrate, a p-i-n junction configuration, as shown in Figure 4.6d. The nominal doping intended for p-type (InP:Zn) and n-type is around 10^{17} cm^{-3} and 10^{19} cm^{-3}, respectively (please refer to Chapter 3.2.1.1 for

more details). This intentional doping asymmetry was crucial for conducting comprehensive C-V analysis.

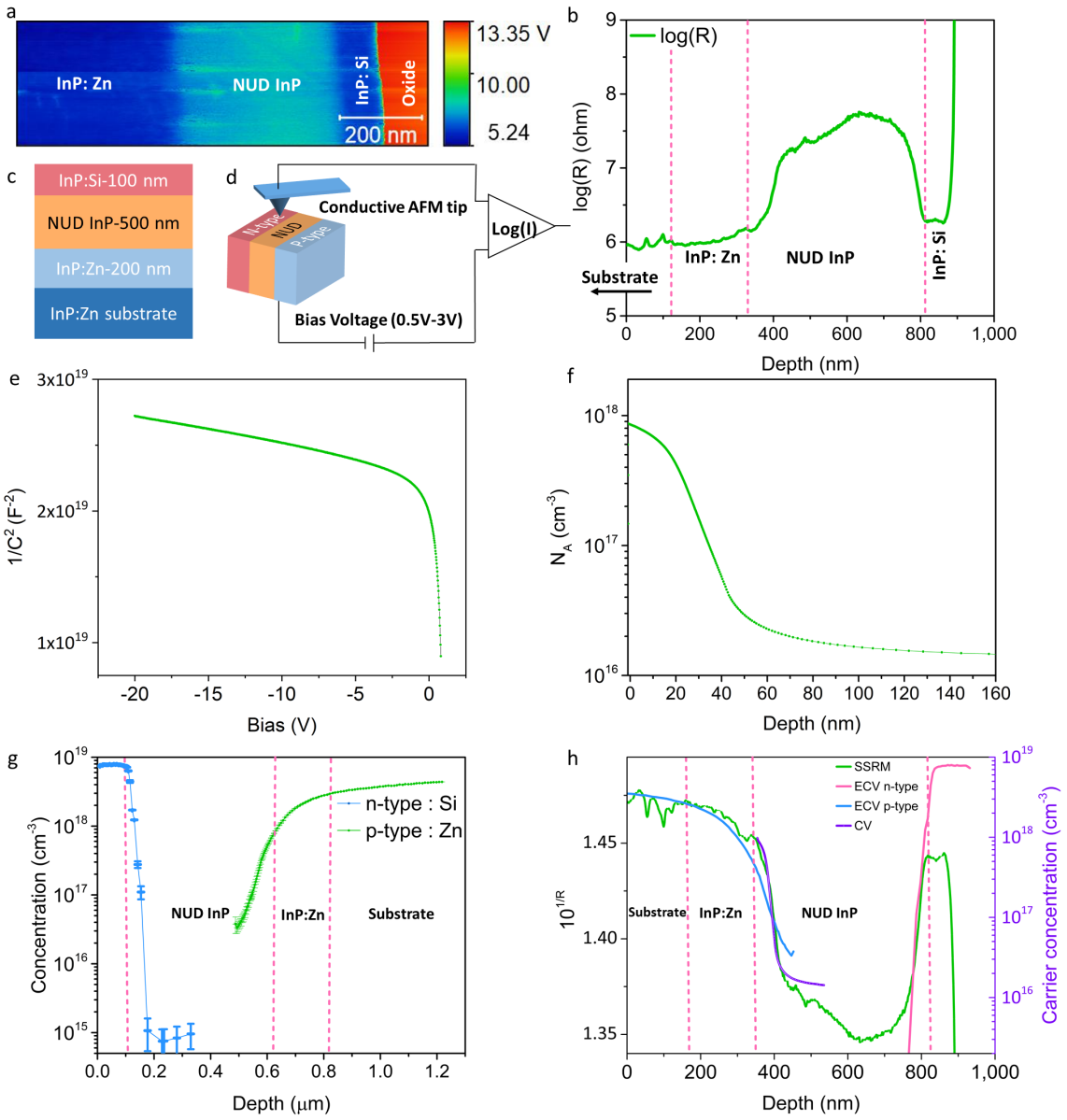


FIGURE 4.6: Electrical characterization of InP:Si/InP/InP:Zn layers grown on a nominally perfectly oriented Zn doped substrate. a) SSRM: 2D cross sectional resistance map obtained from a cleaved cross sectional sample surface b) Extracted resistance value of averaged lines through scan direction. The dotted lines indicate the nominal boundaries between the Zn doped, NUD and Si doped InP layers. c) Schematic of epi-structure d) Schematic of SSRM measurement setup e) CV measurements: The extracted $1/C^2$ curve from the device, with curvature indicating non-uniform doping f) Mott-Schottky analysis of (e), yielding the doping profile. g) ECV depth profiling of the sample h) compendium of the different techniques. To be able to obtain a clear comparison, SSRM profile is rescaled from log(R) to $10^{1/R}$. X-axis of ECV depth profile is also reversed so that it is aligned with the CV curve.

SSRM provides a qualitative assessment of local resistance, with low-resistance values corresponding to higher active dopants [111]. Figure 4.6a shows the SSRM signal obtained from a

2D cross-sectional scan across epitaxial layers as shown schematically in Figure 4.6c and Figure 4.6d on a specifically grown sample. Figure 4.6b shows the resistance versus distance plot extracted from an average of all the scan lines of the SSRM image. Inspections of Figure 4.6b reveals the presence of a relatively high-resistance layer, with a thickness similar to the NUD layer from the nominal design. Repeated measurements of the same samples through different cleaves yielded very similar qualitative outputs, albeit with quantitative differences (not shown here); therefore, we have not stated the doping levels. While the SSRM results do not allow for an accurate evaluation of the doping levels, Figure 4.6b implies that Zn forward-diffusion in the NUD InP layers is electrically inactive, thus explaining the significant differences in measured resistance.

A device structure was fabricated from the SSRM sample to allow C-V measurements as an additional test of the dopant properties in the NUD layer (refer to Chapter 3.2.1.2 for more details of fabrication process, measurement details and characterization). Figure 6e shows the extracted $1/C^2$ with curvature indicating a non-uniform doping. A Mott-Schottky analysis, as described by Equation 3.5, is conducted to calculate the doping profile, as shown in Figure 6f, revealing less than 100 nm of active Zn incorporation (forward-diffusion) into the NUD layer.

In Figure 4.6g, ECV results of the sample (structure depicted in Figure 4.6c) demonstrate a similar dopant profile, indicating that the forward Zn diffusion in the NUD layer appears electrically inactive. It is worth noting again the substrate used here is a Zn-doped InP substrate chosen for contacting purposes. Consequently, there might be (and there is) some Zn diffusion from the substrate into the epi-materials, i.e. the Zn doping concentration level is higher than the intended nominal value.

Figure 4.6e compares the curves obtained from C-V, ECV and SSRM techniques. To facilitate a clear comparison, the SSRM profile is rescaled log(R) to $10^{1/R}$, as the doping is inversely proportional with the resistance. Additionally, the x-axis of the ECV depth profile is reversed to align with the C-V curve. While our electrical measurement results do not perfectly match quantitatively, they demonstrate strong qualitative agreement. Our results are consistent with the active doping of Zn incorporation during intentional doping (and its "normal" diffusion remaining active and doping), while the floating excess Zn is not electrically active and incorporates in a different role than simply occupying group-III sites and bonding with the group-V element. Obviously, our results cannot distinguish between which of the possible "other forms" (e.g., interstitial, defect centres coupled or not to vacancies etc.). Nevertheless, tentatively, this

is coherent with the suggestion raised before and in Ref. 106 that the Zn(ULIE) SIMS scanning technology is only picking the active Zn content, while the others are also differently affected by the other form of Zn incorporation.

4.3 Suppressing the Zn forward-diffusion

Overall, it is evident that the additional incorporation of Zn, while not directly active as a dopant, remains an undesirable feature in most devices. This is because it has the potential to become activated during subsequent device processes or contribute the generation of trap and scattering centres for carriers while assisting non-radiative recombination. To eliminate its presence and indirectly test (again) the reactor memory effects, we explored a couple of alternatives.

First, we applied a simple growth interruption step after the intentionally doped layer, denoted as point A in the SIMS figures (e.g Figure 4.1a, Figure 4.7a), to check if we can clear the surface from the excess Zn. During the growth interruption, the TMIn (the indium source) flux was stopped, while the reactor was kept for 5 minutes at growth temperature and pressure, with a PH_3 and N_2 carrier gas overflow identical to the one used during growth. The rationale behind this is that the excess Zn would have a chance to evaporate (or decompose) from the surface during the growth interruption. On the other hand, if the phenomenon were due to the reactor memory effects, i.e., the excess Zn was coming from the reactor walls, the growth interruption would have increased the amount of Zn on the surface.

The SIMS result from this growth is shown in Figure 4.7a, revealing that Zn exhibits a strikingly shorter forward-diffusion length (around 170 nm) with no spike at the interface, when compared to the samples without a growth interruption (e.g. Figure 4.1). Although Zn still exhibits an asymmetric profile, with the back-diffusion shorter than the forward-diffusion length, the previously measured excess Zn accumulated on the sample surface is eliminated (at least partially) due to the growth interruption.

While adding this 5 min growth interruption step results in a significant reduction in the forward-diffusion phenomena, it does not yet constitute a comprehensive solution applicable to all MOVPE structures. It is possible that a substantially longer growth interruption would be necessary to further reduce the excess Zn with potential consequences in device quality in

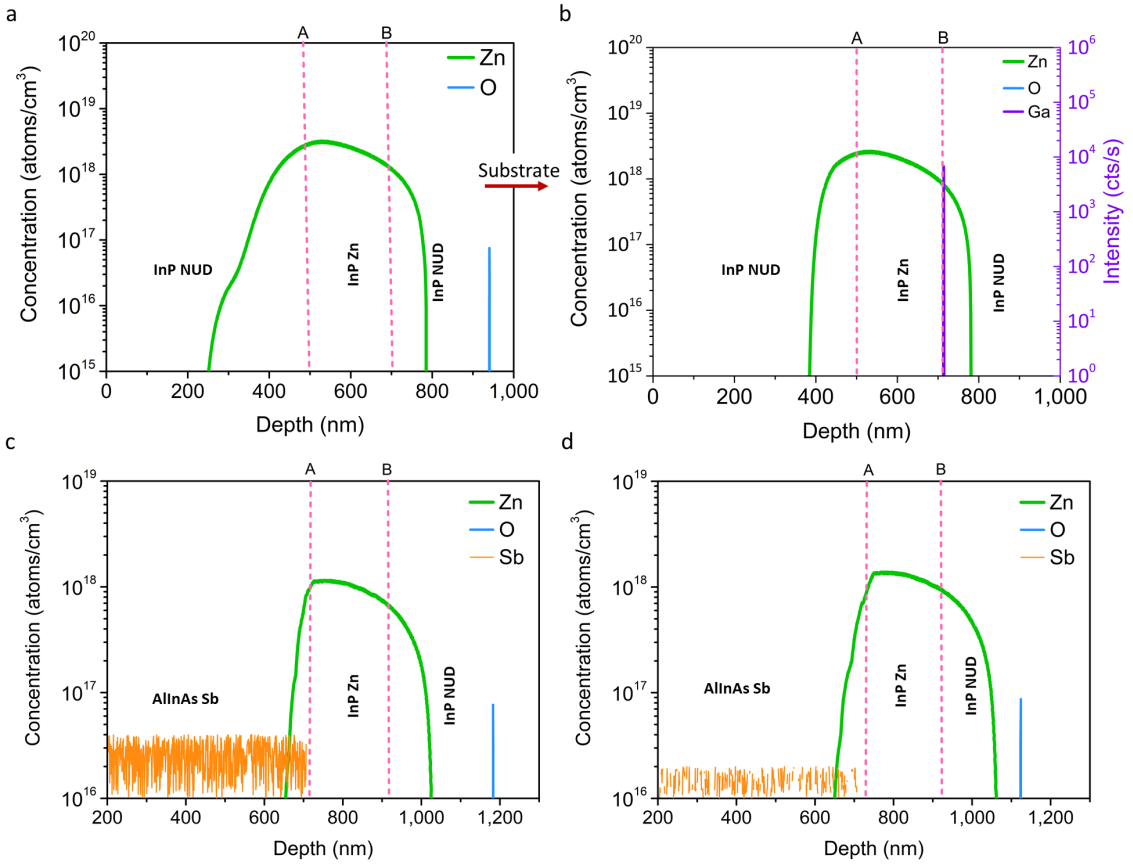


FIGURE 4.7: Effect of growth interruption on the Zn tailing a) 5 minutes growth interruption with PH_3 overflow reduces the post growth tailing to around 250 nm, measured with a slow Zn(lowV) scan. b) 5 minutes growth interruption with PH_3 and TMSb overflow reduces the post growth tailing to around 100 nm measured with a slow Zn(lowV) scan. An InGaP marker layer was added to identify the first undoped to doped interface and the back diffusion region. A-B markers and red lines are used here as in Figure 4.1. c) Sb assisted AlInAs layer is immediately started (No growth interruption is applied) after the Zn doped InP layer. d) Same structure and growth protocol with sample (c) with half Sb flow. Zn doping profile is almost identical, Sb incorporation is reduced ≈5 times of that in (c)

general. Therefore, we needed to investigate an additional option, guided by the following reasoning: if Zn is acting as a surfactant during growth, it might be possible (in the absence of a complete theoretical understanding) that introducing a different, well-known surfactant could compete on the surface with Zn, potentially suppressing its presence. Hence, we implemented an experiment where we performed a growth interruption under Sb, another well-known surfactant in the world of III-V materials [92].

In detail, during the 5 min growth interruption after the intentionally doped layer growth, only PH_3 and TMSb (Trimethylantimony, Sb precursor) were flowing through the reactor with N_2 as the carrier gas. The Sb source was then shut-off while the InP growth was restarted, as it is known that Sb incorporates (at these growth conditions) a few percent in InP. The SIMS result

in Figure 4.7b shows that the Zn forward-diffusion length is significantly shorter compared to the sample without TMSb flow during the growth interruption (Figure 4.7a). In this specific sample, the interface between the InP buffer and Zn-doped layer was delineated with a short pulse of InGaP during the epitaxial growth to facilitate the SIMS depth profile (in the graph, right x-axis represents the intensity of the Ga signal). No trace of Sb is detected in the sample by SIMS analysis.

The effect of utilizing TMSb on Zn forward-diffusion is examined in samples featuring AlInAs as the top layer with the SIMS results shown in Figure 4.7c and Figure 4.7d. Here, the lack of Sb incorporation (at variance to InP) allowed us to maintain the Sb source on throughout the post-doped region growth. Specifically, in both samples, the Sb-assisted AlInAs layers were started immediately after the intentionally doped InP:Zn layer without any growth interruption. The growth procedure was identical for the two growths with the only difference being that, we used ≈5 times less the amount of Sb flow in the sample presented in Figure 4.7d compared to that in Figure 4.7c. Generally, Zn suppression is more effective, albeit with slightly smaller Zn forward-diffusion and higher Sb incorporation observed in the sample shown in Figure 4.7c.

In addition to minimizing the Zn forward-diffusion, a significant observation is the absence of oxygen traces in the AlInAs layers (compared to samples in Figure 4.5a), which we will discuss in detail later in Chapter 6.

4.4 Zn Back Diffusion in Different Misoriented Substrates

The preparation of epitaxy-ready substrates involves slicing individual sections from a bulk crystal at a specified angle relative to the primary crystallographic plane. Regarding the InP (100) substrate, the crystallographic steps revealed after cutting can be finished ideally with either indium, known as A-steps, indicating a misorientation (miscut) of the substrate towards the (111)A planes, or phosphorus atoms, known as B-steps, indicating a misorientation (miscut) towards (111)B planes, or a combination of both [116, 117].

To have a better understanding of the effect of surface misorientation on the Zn forward and backward diffusion, we grew doped InP layers on three different InP substrates: intentionally misoriented by 0.4° towards the (111)A crystallographic plane (± 0.02°), intentionally misoriented by 0.4° towards (111)B crystallographic plane (± 0.02°) and nominally perfectly oriented. The last sample exhibits, as expected, a slight but random surface misorientation (± 0.02°).

We used a slightly lower Zn flow than previous experiments for these samples, aiming to a nominal doping of 5x10^{17} cm^{-3} (between the sample Figure 4.1a and Figure 4.1c) with a doping layer of 500 nm (Figure 4.8). The epi-layers on the perfectly oriented substrate also serve as an exploratory measure to test if we observe a comparable doping concentration profile to that seen in Figure 4.1c, given the intermediate doping level.

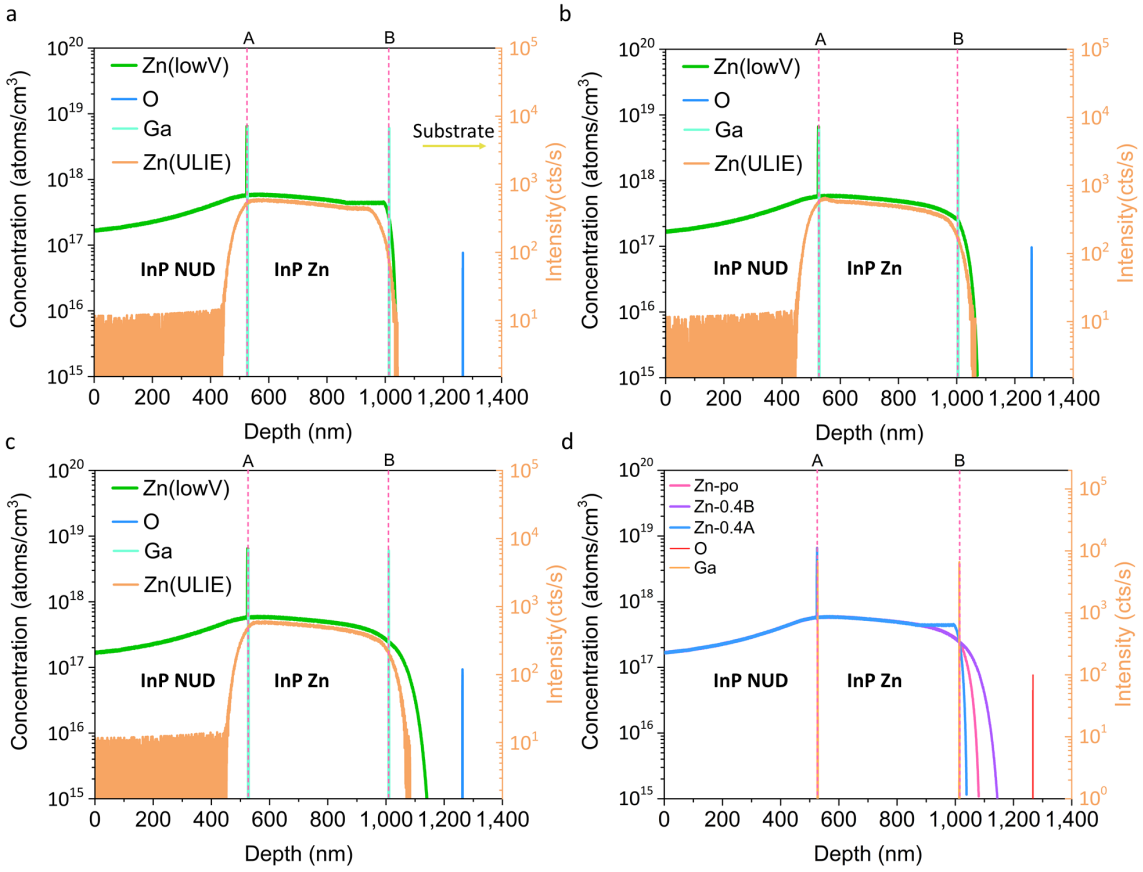


FIGURE 4.8: Effect of substrate misorientation on the background doping. InP/InP:Zn/InP layers grown on a a) 0.4° misoriented towards (111)A crystallographic plane, b) 0.4° misoriented towards (111)B crystallographic plane and c) nominally perfectly oriented d) comparison of all the samples, with the InGaP layer producing a Ga marker facilitating the graphs' alignment. A-B markers and red lines are used here as in Figure 4.1 to identify the InP Zn-doped layers.

For these samples, we marked the interfaces (between nominally undoped and intentionally doped layers) by introducing a very low concentration of Ga during the InP growth (for only 1 nm) to facilitate the analysis of the SIMS depth profile, as already discussed in the previous section (so we could unambiguously perform an alignment between different sample graphs). All the samples in this section were grown simultaneously.

The SIMS data (Figure 4.8, particularly Figure 4.8d) indicate that although there are no significant differences in forward diffusion, there is a notably higher backward diffusion of Zn in the sample misoriented towards the B-plane compared to the one misoriented towards the A-plane.

In the nominally perfectly oriented samples, the backward diffusion falls between A and B, as expected for a combination of A and B steps. This result was not expected, but we observe that it is coherent with the hypothesis that, during Zn incorporation, different paths can be present. Figure 4.8 suggests that these are influenced by the exact step organization [63] of the samples, with a somehow "cleaner" sample obtained when A-steps are present, while the B-misorientation results in more unwanted Zn species and incorporation.

4.5 Photoluminescence of the Doped Layers

For completeness, we conducted low-temperature (at 14 K) PL measurements to explore the impact of Zn doping on both the doped layers and subsequent epitaxial layers. In Figure 4.9c, samples that contain a Zn-doped layer, followed by a NUD InP cap, generally exhibited band-edge emission of free excitons (FX), shallow acceptor bound excitons (A^0X), and shallow acceptor (e/D-A^0) emission, along with its LO-phonon replicas (Figure 4.10) as discussed in the literature [118, 119]. Additionally, a distinct emission band, with a peak around 1405 meV and a Gaussian FWHM of approximately 8 meV, was consistently observed in all Zn-doped samples. This emission can be tentatively attributed to excitons bound to a deep-donor band (DDX) [120, 121]. At room temperature a low energy shoulder was observed (not shown), which was not present in any samples capped with additional NUD InP. Indeed, these features have not been observed even with the thinnest NUD caps of 200 nm.

In only doped samples (Figure 4.9a), because of the high concentration of dopants, the free excitonic emission characteristic of pure semiconductor is typically suppressed, and PL occurs primarily through relaxation to shallow acceptors. In fact, the radiative recombination is mainly between the aforementioned deep-donors and the shallow acceptors (DD-A^0). Moreover, in Figure 4.9d we show the excitation intensity dependence of the DD-A^0. A blueshift of 65 meV per decade of excitation fluence was observed, close to the 50 meV per decade previously observed for in-situ doped InP:Zn[122], and several times larger than that seen in Zn-diffused InP:Zn [122–124].

In Figure 4.9b it is seen that after a 200nm cap of NUD InP, the DD-A^0 emission is also no longer observed. Instead, the spectrum is dominated by e/D-A^0 and DDX emission. Further capping tends to recover the free exciton line of NUD InP, but the overall spectral trend is complicated, possibly by reduction of non-radiative recombination channels, as well as deeper

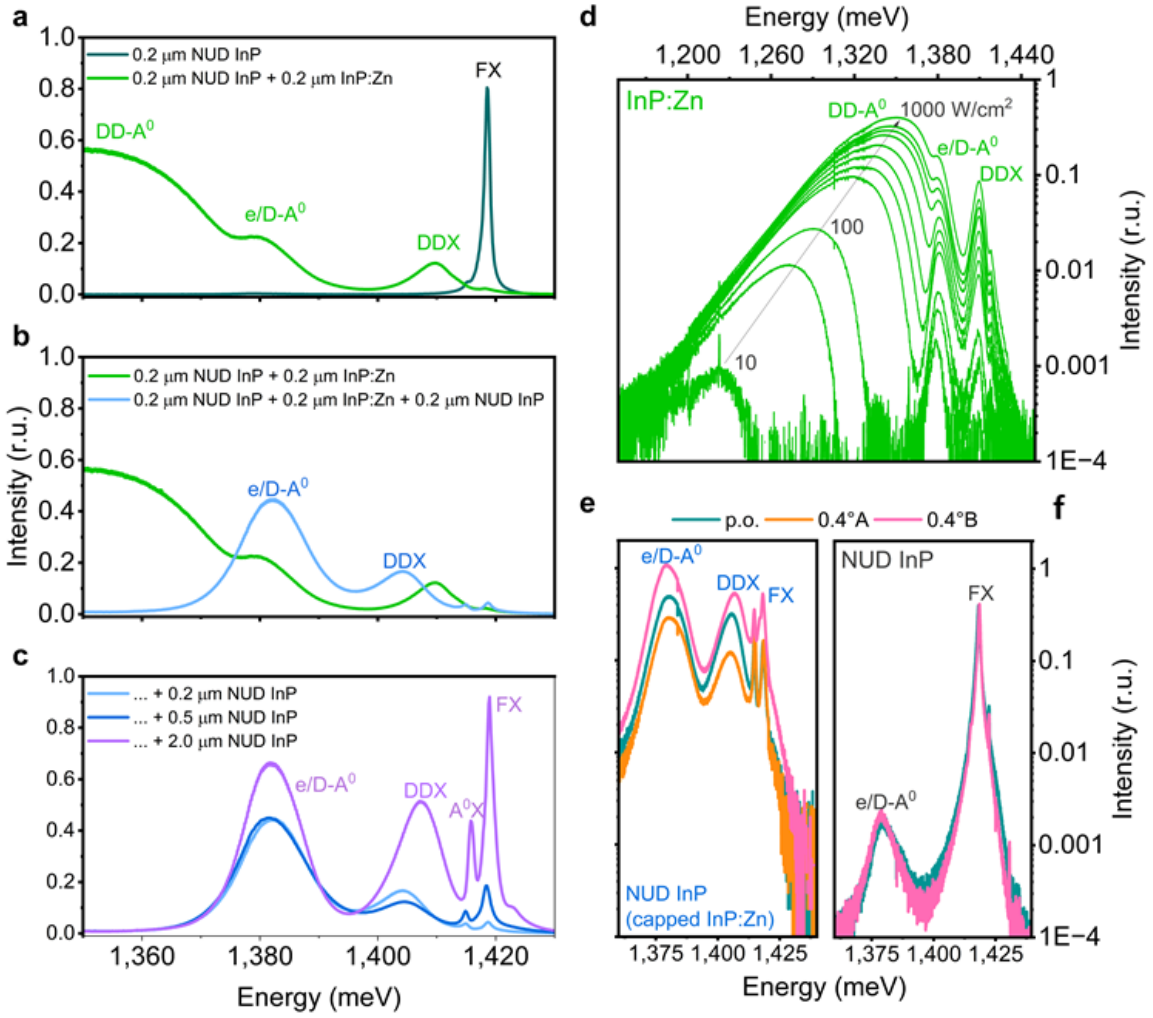


FIGURE 4.9: Low-temperature PL. (a)-(c) Changes in PL as a result of Zn doping and capping. NUD InP (black) spectrum taken at 10 W/cm^2, all others 1 kW/cm^2. (a) NUD InP (black) exhibits a strong free-excitonic (FX) peak only. This is suppressed in Zn-doped InP (green), which has a spectrum dominated by deep-donor to acceptor (DD-A^0) recombination. (b) After capping of InP:Zn by 200 nm of NUD InP (blue) the DD-A^0 emission is absent, and the spectrum is dominated by e/D- A^0 and DDX emission. (c) Further capping tends to recover the free-excitonic emission, but the e/D- A^0 and DDX PL remain. (d) The excitation intensity dependence of the DD- A^0 emission in an uncapped InP:Zn sample. A blueshift of 65 meV/decade is observed. (e) and (f): Effect of substrate misorientation on the PL. (e) In capped InP:Zn, the intensity is significantly higher for 0.4° misorientation towards (111)B, compared to nominal perfect orientation (p.o.), and less for 0.4° misorientation towards (111)A (250 W/cm^2). (f) In NUD InP no significant differences are observed (10 W/cm^2). r.u.: relative units.

penetration of photogenerated carriers in purer material. As such, both impurity-related and free-excitonic emission can increase simultaneously.

As can be seen in Figure 4.9c, the position of the DDX band can vary slightly from sample to sample, but always lies between the band-edge emission and the shallow acceptor band. To the best of our knowledge, this variation has not previously been reported. Thus, it seems

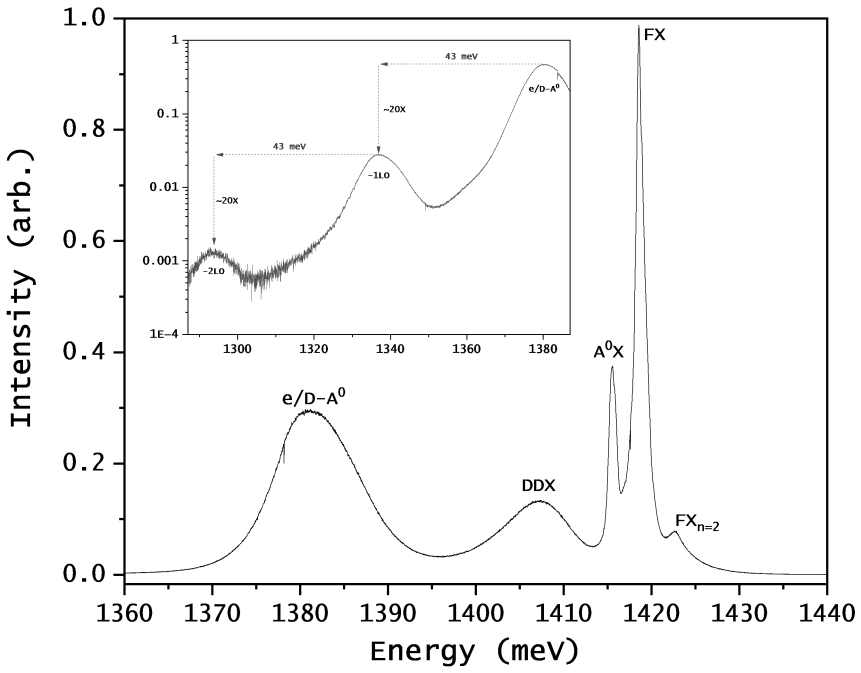


FIGURE 4.10: An example PL at 14 K. This sample consists of 200 nm Zn-doping followed by a 2 μm cap. Inset: LO-phonon replicas of the shallow acceptor band.

that the exact composition of the deep donor band might be sensitive to small changes in the growth conditions, and different complexes might be favoured under some conditions than others, although the exact nature of this behaviour is not understood, and should be the subject of further future investigations. In general, since we observe the unspecified deep-donor bound excitons in Ref. 120 and 121 and the deep-donor-to-acceptor emission of Ref. 122 (who probably also observed a DDX peak, although identified it only as band-edge emission), we can probably attribute these features to interstitial Zn or Zn complexes. Nevertheless, the analysed samples do not allow us to see a clear signature for a different Zn incorporation following the surfactant behaviour and these findings only suggest qualitative differences.

Nevertheless, extending our analysis to the selectively misoriented samples provides some surprises. It was consistently observed (see Figure 4.9e for representative spectra) that the impurity-related PL intensity was higher in substrates with 0.4° misoriented towards (111)B, compared to nominal perfect orientation, which in turn was higher than substrates with 0.4° misorientation towards (111)A. This was observed at both 14 K and at room temperature, and was only true for the Zn-doped samples – for undoped samples there was no significant difference (Figure 4.11). This behaviour seems to correlate with the different back-diffusion profiles, although it

is unlikely that the PL signal is mainly arising from the back-diffused region. This might be indicative of different types of incorporation in the NUD InP top layer depending on orientation, even if the levels of Zn and ZnP_3 appear to be the same in that region. On the other hand, the SIMS profiles showed similar forward Zn profiles in terms of Zn and ZnP_3 concentration in all samples irrespective of misorientation (Figure 4.8).

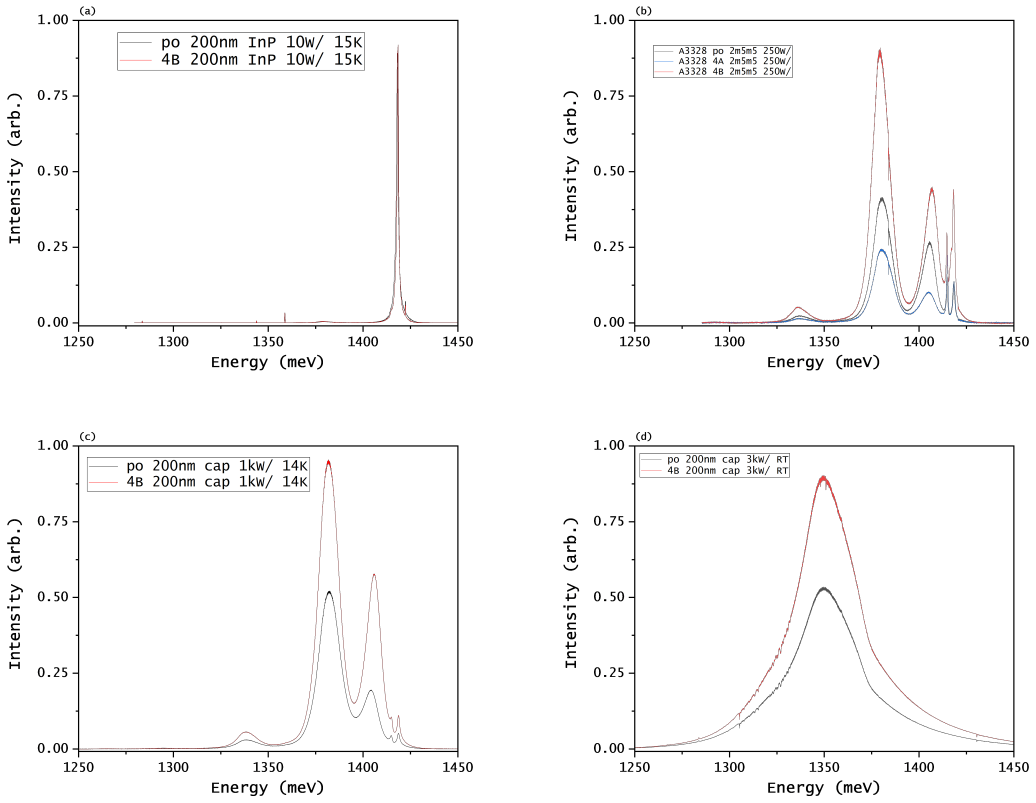


FIGURE 4.11: Effect of substrate misorientation on the PL for a) 200 nm Zn:InP layer grown on (100) perfectly oriented (po) and (100) 0.4° misoriented towards (111)B (4B) samples (15 K, 10 W/cm^2), b) samples shown in Figure 4.8 (14 K, 250 W/cm^2), c) samples (a) measured at 14 K taken with 1 kW/cm^2 and d) samples (a) measured at room temperature (295 K, 3 kW/cm^2) A similar difference in intensity is seen at low temperature (14 K, 1 kW/cm^2) and at room temperature (295 K, 3 kW/cm^2).

4.6 Discussion and Conclusion

In this chapter, the initial observation of several previously unreported Zn dopant behaviours in MOVPE was presented.

With clear and systematic evidences, a surfactant behaviour of Zn is observed for the first time. Analysis using SIMS reveals a Zn dopant profile that significantly different from what would

be expected solely from diffusion process, which typically yield a symmetric doping profile. Specifically, a Zn dopant concentration exceeding 10^{15} atoms/cm^3 is detected up to 1500 nm -an oddly large thickness- from where the doping flow ended in NUD layer. On the other hand, SIMS(ULIE), C-V and SSRM analysis indicate that the extended Zn presence in the NUD layers is predominantly electrically inactive, i.e., it does not incorporate substitutionally, and generates either interstitial, point defects, or possibly more complex multi atomic structures (e.g. a vacancy impurity scheme, or Zn-"other impurity" compounds). During the Zn-doped layer growth, the growth conditions (in their thermodynamic and kinetic aspects) favour the proper substitution of indium sites by Zn and stable bonding with phosphorus atoms. This certainly seems the dominating mechanism during the "doping" phase of our experiments, where the continuous supply of Zn appears to sustain the correct growth conditions for proper positioning of Zn atoms in the lattice and their activation as main incorporation mechanisms. However, once the Zn precursor is shut-off the incorporation mechanism seems to change immediately because of the change in the growth conditions (lack of Zn/Zn precursor supply), resulting in an incorporation process dominated by non active Zn. All these different incorporation pathways of Zn show that Zn can incorporate into the lattice in different ways and only some them result in dopant activation.

Another important implication of these observations is that the naive procedure for the calibration of Zn doping concentration usually adopted for SIMS measurement interpretations, such as simple standard ECV profiling or Hall measurements, are likely to deliver misleading results, as in general no correction has been applied to take into consideration the "non" doping Zn contribution when present. Indeed, calibration standard samples are used to map the measured intensity values in SIMS to doping concentration values by correlating the SIMS results with ECV or Hall measurements. Our results show that there is a possible path for error in this conventional approach as the inactive Zn dopant concentration is not captured in ECV or Hall measurements.

Comparable layers based on GaAs and InGaAs exhibit a shorter post-growth tail of approximately 200 nm. This suggests that the surfactant physics is dependent on the III-V compound type. This also points to the fact that the very long tailing in InP is not a reactor memory effect, as sometimes these results could be misinterpreted.

The observed incorporation profile suggest that either the intact or partially decomposed Zn

precursor, or atomic Zn, is still present on the epitaxy process even without Zn flow. Consequently, the Zn accumulated at the epi-surface is being gradually incorporated into the epitaxial layers even after the Zn source has been closed. In this context, it is worth to mention that, Gocalinska et al. previously demonstrated that Zn dopants notably influence the step organization of InP surface structures in MOVPE-grown InP layers, such as reducing step bunching [63]. This points to a relatively high concentration of Zn on the surface, likely exceeding the amount strictly necessary to obtain the required doping (which would be 4-5 orders of magnitude less than the indium atom density for example). These observations aligns with findings concerning another surfactant, tellurium (Te). Lee et al. found that Te decreased the surface roughness by eliminating step bunching in GaAs epitaxial layers [94]. Similarly to our case, some authors have shown that the presence of Te dopants in nominally undoped post-growth layers does not result from desorption or parasitic reactions from the walls (i.e. not a classical reactor memory effect) [95, 96].

It is also shown that, the effect can be suppressed and controlled. The most straightforward approach found that is to implement a 5-minute growth interruption protocol immediately after the growth of Zn doped layer through hydride exposure. A growth interruption with Sb, another surfactant of InP, and PH_3 effectively reduces the forward-diffusion distance to approximately 120 nm.

This can be an implication of a competition of surfactants over the InP surface where Sb wins over Zn. Additionally, the capability of suppressing the excess Zn signal also demonstrates that the various SIMS methodologies for detecting Zn are not “inherently” superior to one another but rather (and simply) sensitive to different Zn species generated during the incorporation processes.

As part of our results, we also observed that even a substrate misorientation as little as 0.4° could significantly affect back-diffusion. The reason for the significantly higher Zn back-diffusion in samples misoriented towards (111)B compared to (111)A is not entirely clear. One possibility is that samples miscut in the B direction could result in a higher defect density, which would result in higher Zn diffusion mediated by these defects. Indeed, the complexity of our results, including the effect of the substrate on the amount of "non active" Zn, suggest the presence of a variety of potential defect complexes, beyond the simple wrong site occupation or co-presence with vacancies. More complex arrangements involving the "coupling" of other impurities and vacancies to the Zn atom might be a better (speculative) explanation. In this context, the

different surface bonding configuration of A vs B steps might provide the different incorporation paths required for such "complexes" to be more or less favored. More experiments, capable of shedding light on defect analysis, including micro-photoluminescence, raman spectroscopy and/or thermal annealing experiments might help to understand this phenomenology better.

In the next chapter, a model combining the material incorporation mechanism with well-known diffusion laws to mimic the surfactant behavior will be presented.

Chapter 5

Theory of Zn Surfactant Behaviour

The preceding Chapter 4 discussed the Zn doping concentration profile derived from various techniques such as SIMS, C-V profiling, ECV and SSRM. Clear and systematic evidence has been presented indicating that Zn (or its precursors, whether intact or partially decomposed) behaves as a surfactant, by accumulating on the epi-surface during the intentional layer doping. This accumulated material on the surface gradually incorporates into the material after the Zn source has been shut off. This chapter investigates this surfactant behaviour further through theoretical modelling and suggests a simple numerical solution for the observed Zn dopant behaviour. In the subsequent sections, the numerical model is utilized to extract two distinct diffusion constants from InP samples grown on the 0.4° misoriented substrates in the A and B direction.

5.1 Theoretical model: Coupled equations

Building on our previous discussion, we modelled the Zn surfactant and diffusion processes assuming Zn can act as a surfactant, accumulating on the sample surface during the growth, and gradually incorporating into the layers after the Zn flow has been stopped. This implies a novel time-dependent numerical solution, at variance to the commonly found literature in the field which typically addresses only the simpler bulk dopant diffusion process. As discussed previously in Chapter 2, the Zn profile in the context of back diffusion can be well defined by Fick's second law of diffusion:

$$\frac{\partial c}{\partial t} = D\left(\frac{\partial^2 c}{\partial x^2}\right), \tag{5.1}$$

where D is the diffusion constant, c is the concentration value, t and x represent the time and space domain, respectively [125]. We combined the diffusion equations and material growth assuming that dopants are incorporating into the epi-layer from an accumulated Zn source floating on the sample surface.

The Zn concentration can be described by the following sets of equations (two coupled equations). The first is:

$$\frac{\partial c_S}{\partial t} = -\frac{c_S}{\tau_{iS}} + F - \frac{c_S}{\tau_{DS}}. \tag{5.2}$$

This is first-order equation (in time) of the concentration $c_S(t)$ of Zn atoms (or precursor/-partially decomposed precursor) floating on the surface of the grown epi-layer, and on the right-hand side there are the terms that change the concentration $c_S(t)$. The first term on the right-hand side is the incorporation term (minus sign, as it is removed from the surface) where τ_{iS} is the associated time constant representing the amount of Zn incorporating into the bulk from the surface. In other words, $\tau_{iS} = 1$ indicates that all the material floating on the surface incorporates into the bulk. The second term represents the deposition rate F that is given by the equation

$$F = \frac{1}{a^2 \tau_F}, \tag{5.3}$$

where a^2 is the area of the unit cell and τ_F is the associated time constant, representing the amount of Zn flowing through the chamber. F should be constant during the doped layer growth and equal to zero after the Zn flow is shut off because, in this case, the source (the amount of material (precursors) flowing through the chamber) is constant during the doped layer region. The third term in Equation 5.2 represents the desorption term from the surface, and τ_{DS} is the associated time constant.

The bulk equation is:

$$\frac{\partial c_B}{\partial t} = D\frac{\partial^2 c_B}{\partial z^2} + \frac{c_S}{\tau_{iS}} \tag{5.4}$$

This is a first-order equation (in time) of the concentration $c_B(t, z)$ of Zn atoms incorporated into the bulk material, and on the right-hand side, it has the terms that cause the concentration to change. The first term on the right-hand side is the diffusion term with D as the diffusion constant,

$$D = \frac{a^2}{\tau_D}, \tag{5.5}$$

where a^2 is the area of a unit cell, assuming that diffusion occurs by nearest-neighbor hopping. The second term of Equation 5.4 is the same as the first term of Equation 5.2.

5.2 Numerical modelling

In this section, we present the numerical solution developed to simulate the Zn concentration profile. A Crank-Nicholson algorithm is adapted to numerically solve the diffusion equations with the material incorporation mechanism [126]. This involves adjusting the boundary conditions at each time step to account for the accumulated material on the sample surface. MATLAB R2019b is used as the simulation/modelling environment.

The diffusion equation shown in Equation 5.1 is a partial differential equation (PDE), which is a mathematical equation that involves multiple independent variables and their partial derivatives. Here, $C(x,t)$, representing the concentration of Zn atoms, is the unknown function to be solved for, where x denotes a spatial coordinate and t indicates time. In our case, the space component is one-dimensional with the diffusion coefficient D determining how fast C changes in time [125, 126].

The choice of numerical method significantly influences various aspects of the solution process. For instance, the accuracy of the approximation, the complexity involved in developing and debugging the solution method, as well as the speed of the code, are all affected. In this thesis, we implemented a finite difference method (specifically, Crank-Nicolson scheme) over finite element or finite volume method to numerically solve the diffusion equation primarily due to its simplicity, ease of implementation and little computational memory requirements when compared to the other methods [126, 127].

5.2.1 Finite difference methods

Finite difference methods are utilized to obtain approximate solutions for unknown functions (such as $C(x,t)$) in PDEs using discrete points at a finite set of x and t. In other words, the unknown function is identified by a discrete approximation, such that the numerical solution will only be known at a finite number of points in the physical domain. Approximations to the governing differential equation are obtained by replacing all continuous derivatives by discrete

$$\frac{\partial C}{\partial x} = \lim_{\Delta x \to 0} \frac{C(x) - C(x - \Delta x)}{\Delta x}. \tag{5.6}$$

The first step in any finite difference method is discretization, achieved by constructing a mesh with points across a domain in which the equation to be solved. The distance between points

in time, Δt, and the distance between points in space, Δx, are the two key parameters of the discretization (as shown in Figure 5.1a). In general, increasing the number of points in the mesh increases the resolution and accuracy of the numerical solution.

The mesh in Figure 5.1a is a schematic representation of the numerical solution and Figure 5.1b shows the changes in the concentration function over time.

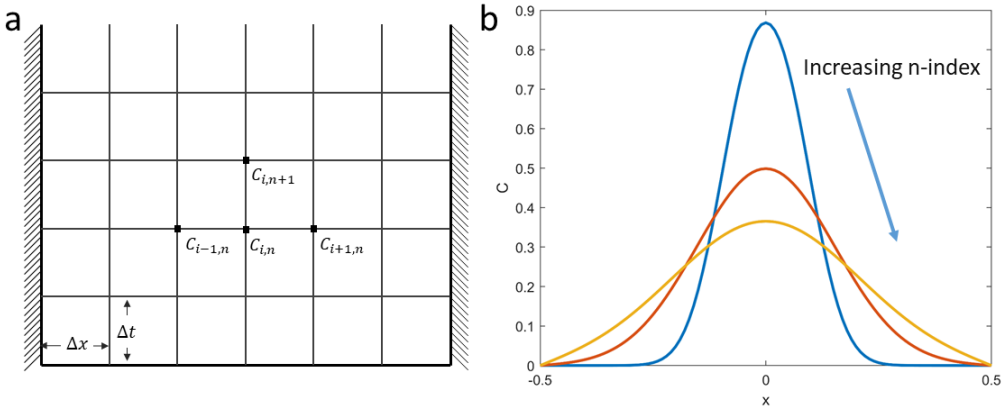


FIGURE 5.1: Illustration of the finite difference method. a) The mesh is the set of locations where the discrete solution is computed. Each n-index corresponds to a time step and each i-index corresponds to position (depth) into the material. b) The evolution of the concentration function in time.

Defining the Mesh: In our scenario, the epitaxial layers are discretized into cells with a width of Δx (or dx in the code), where i represents the spatial index. The growth time is discretized with a step size of Δt (or dt in the code), where n represents the time index.

The concentration function $C(x,t)$, as defined with the diffusion equation $\frac{\partial C(x,t)}{\partial t} = D\frac{\partial^2 C(x,t)}{\partial x^2}$, will be approximated in the domain $0 \leq x \leq L$ and $0 \leq t \leq t_{\max}$. The spatial points (x_i) are uniformly distributed within the interval $0 \leq x \leq L$ such that

$$x_i = (i-1)\Delta x, \quad i = 1, 2, \ldots, N_x\,, \tag{5.7}$$

where N_x total spatial nodes, including boundary points. Thus, when L and N_x is given, the spacing between x_i can be calculated as

$$\Delta x = \frac{L}{N_x - 1} \tag{5.8}$$

or when N_x and Δx are given, the domain length L can be calculated by

$$L = \Delta x(N_x - 1). \tag{5.9}$$

We preferred to use latter one (Equation 5.9) in our code (Listing 5.1).

Similarly, the time points t_n are uniformly spaced within the interval $0 \leq t \leq t_{\max}$ so that

$$t_n = (n-1)\Delta t, \quad n = 1, 2, \ldots, N_t\,, \tag{5.10}$$

where N_t is the number of time steps separated by the distance Δt [128]

$$\Delta t = \frac{t_{\max}}{N_t - 1}. \tag{5.11}$$

Listing 5.1 shows the Matlab code snippet used in the preparation of the simulation grid with the provided variables used to simulate the concentration profile depicted in Figure 5.3a.

```
%%%%%%%setting and initializing the parameters
tmax = floor(3000/2); % end time
dx = 0.2541e-7;  % spacing in x
dt = 1/20;     % spacing in t
nx = 10000;    % number of nodes in x
nt = tmax/dt+1; % number of timesteps
l = dx*(nx-1); % length of domain in x

%%setting up the mesh
x = linspace(0,l,nx);
t = linspace(0,tmax,nt);
```

LISTING 5.1: MATLAB code snippet for setting up the mesh. The values are the variables used to simulate the concentration profile in Figure 5.3a.

After discretization and forming the mesh, the C_i^n values are calculated through an iteration process.

There are two types of finite difference methods depending on the handling of the time stepping and iteration process: explicit and implicit. In an explicit finite difference scheme, such as forward time-centered space (FTCS) scheme, the concentration at time $n+1$ is explicitly dependent on the concentration at time n. Implicit methods, such as backward time-centered space (BTCS), find the solution by using both the concentration at time n and $n-1$.

When choosing a finite difference method scheme, the stability plays an important role. Stability, in this context, refers that minor errors or disturbances in the initial conditions do not lead

to exponentially growing errors in the solution over time [129]. A numerical solution becomes unstable when the values of C at the nodes oscillate or grow beyond the limits defined by the initial and boundary conditions [126].

Derivatives in the diffusion equation (Equation 5.1) can be approximated by Taylor's series expansions as follows [130–132]:

Forward difference in time,

$$\frac{\partial C}{\partial t} = \frac{C_i^{n+1} - C_i^n}{\Delta t} + \mathcal{O}(\Delta t), \tag{5.12}$$

backward difference in time,

$$\frac{\partial C}{\partial t} = \frac{C_i^n - C_i^{n-1}}{\Delta t} + \mathcal{O}(\Delta t), \tag{5.13}$$

and central difference in space,

$$\frac{\partial C}{\partial x^2} = \frac{C_{i-1}^n - 2C_i^n + C_{i+1}^n}{\Delta x^2} + \mathcal{O}(\Delta x^2). \tag{5.14}$$

The terms $\mathcal{O}(\Delta t)$, $\mathcal{O}(\Delta t^2)$, $\mathcal{O}(\Delta x)$, and $\mathcal{O}(\Delta x^2)$ represent the order of local truncation error, i.e., the order of accuracy. This error comes from truncating the Taylor series. After neglecting the truncation errors to simplify the equations, the following finite difference schemes can be obtained. Specifically, these schemes include the FTCS method, which is explicit in nature, the BTCS method, an implicit approach, and the Crank-Nicholson scheme, also implicit. Each of these approaches differs in their handling of time and spatial derivatives. Figure 5.2 represents the computational units used to implement each method.

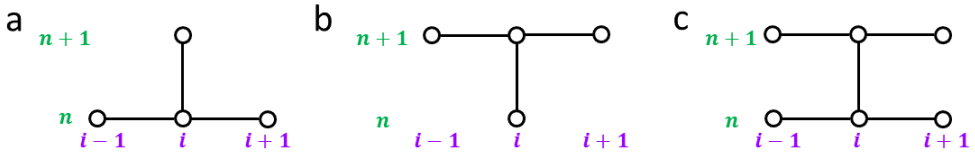


FIGURE 5.2: Computational molecules used in different finite difference methods. a) Forward time- Centred Space b) Backward time- Centred Space and c) Crank-Nicholson. The n-index represents the discretised time points and i-index corresponds to the discretised spatial points.

- **Forward Time, Centered Space (FTCS) Method:**

The FTCS scheme is formulated by replacing the time derivative $\partial C/\partial t$ (of Equation 5.1) with a forward difference approximation (Equation 5.12) and the second-order spatial derivative $\partial^2 C/\partial x^2$ (of Equation 5.1) with the central difference approximation (Equation 5.14). Thus,

Equation 5.1 becomes

$$\frac{C_i^{n+1} - C_i^n}{\Delta t} = D\frac{C_{i-1}^n - 2C_i^n + C_{i+1}^n}{\Delta x^2} \tag{5.15}$$

which can be rearranged to solve for C_i^{n+1} as

$$C_i^{n+1} = C_i^n + D\Delta t\frac{C_{i-1}^n - 2C_i^n + C_{i+1}^n}{\Delta x^2}. \tag{5.16}$$

The implementation of the FTCS scheme is very straightforward, making it easy to apply. Each value of C_i^{n+1} can be solved independently. Computationally, the entire solution can be handled in two nested iterative loops: an outer loop iterates over all time steps and an inner loop that iterates over all the spatial nodes. However, the stability of the FTCS method depends on the choice of Δt and Δx. To ensure stability, these numbers should be selected carefully meeting the stability requirement of [133].

$$\lambda = \frac{D\Delta t}{\Delta x^2} < \frac{1}{2}. \tag{5.17}$$

- **Backward Time, Centered Space (BTCS) Method:**

The BTCS scheme is expressed by substituting the time derivative $\partial C/\partial t$ (of Equation 5.1) with backward difference approximation (Equation 5.13) and the second order spatial derivative $\partial^2 C/\partial x^2$ (of Equation 5.1) with the central difference approximation (Equation 5.14). Thus, Equation 5.1 becomes

$$\frac{C_i^n - C_i^{n-1}}{\Delta t} = D\frac{C_{i-1}^n - 2C_i^n + C_{i+1}^n}{\Delta x^2}. \tag{5.18}$$

Here, Equation 5.18 cannot be easily rearranged to obtain a simple algebraic formula, as in Equation 5.15 and Equation 5.16, to compute C_i^n from its neighbors C_{i-1}^n, C_{i+1}^n, and C_i^{n-1}. To see the system of equations more clearly, Equation 5.18 can be rearranged to the following form with C^n terms on the left-hand side and C^{n-1} terms on the right-hand side:

$$-\frac{D}{\Delta x^2}C_{i-1}^n + \left(\frac{1}{\Delta t} + \frac{2D}{\Delta x^2}\right)C_i^n - \frac{D}{\Delta x^2}C_{i+1}^n = \frac{1}{\Delta t}C_i^{n-1}. \tag{5.19}$$

The Equation 5.19 can be expressed in the matrix form as

$$\begin{bmatrix} b_1 & c_1 & 0 & 0 & 0 & 0 \\ a_2 & b_2 & c_2 & 0 & 0 & 0 \\ 0 & a_3 & b_3 & c_3 & 0 & 0 \\ 0 & 0 & \ddots & \ddots & \ddots & 0 \\ 0 & 0 & 0 & a_{N-1} & b_{N-1} & c_{N-1} \\ 0 & 0 & 0 & 0 & a_N & b_N \end{bmatrix} \begin{bmatrix} C_1 \\ C_2 \\ C_3 \\ \vdots \\ C_{N-1} \\ C_N \end{bmatrix} = \begin{bmatrix} d_1 \\ d_2 \\ d_3 \\ \vdots \\ d_{N-1} \\ d_N \end{bmatrix} \tag{5.20}$$

with the coefficients of the interior nodes

$$\begin{aligned} a_i &= \frac{D}{\Delta x^2}, \\ b_i &= \frac{1}{\Delta t} + \frac{2D}{\Delta x^2}, \\ c_i &= -\frac{D}{\Delta x^2}, \\ d_i &= \frac{1}{\Delta t} C_i^{(n-1)}, \end{aligned} \tag{5.21}$$

where $i = 2, 3, \ldots, N-1$ [126].

The BTCS scheme is implicit. Thus, the implementation of this scheme requires solving a system of equations at each time iteration. Not only does this introduce complexity in the code development process, but it also involves a higher computational load per time step compared to the FTCS scheme. However, the BTCS scheme has one remarkable benefit over FTCS scheme: it has unconditional stability in solving the diffusion equation and it is as accurate as the FTCS scheme [131]. Therefore, with some extra effort, the BTCS scheme offers a robust computational framework, particularly useful when the flexibility is required in selecting different step sizes for time (Δt) and space (Δx) that do not meet the criteria in Equation 5.17.

- **Crank-Nicholson method:**

In the Crank-Nicholson method, the left hand side of the diffusion equation (Equation 5.1), $\partial C/\partial t$, is approximated by using the backward time difference as in BTCS scheme. The right hand side of the diffusion equation (Equation 5.1), $\partial^2 C/\partial x^2$, is approximated by the average of the central difference scheme evaluated at the current and previous time step. This leads to

the following representation of Equation 5.1:

$$\frac{C_i^n - C_i^{n-1}}{\Delta t} = \frac{D}{2}\left(\frac{C_{i-1}^n - 2C_i^n + C_{i+1}^n}{\Delta x^2} + \frac{C_{i-1}^{n-1} - 2C_i^{n-1} + C_{i+1}^{n-1}}{\Delta x^2}\right). \tag{5.22}$$

It is important to note that, at the right hand side of Equation 5.22, the values of C from time step n and $n-1$ appear. Equation 5.22 can be rearranged so that the values of C at time n are on the left and the values of C at time $n-1$ on the right. Thus, the equation becomes

$$\begin{aligned} -\frac{D}{2\Delta x^2}C_{i-1}^n + \left(\frac{1}{\Delta t} + \frac{D}{\Delta x^2}\right)C_i^n - \frac{D}{2\Delta x^2}C_{i+1}^n \\ = \frac{D}{2\Delta x^2}C_{i-1}^{n-1} + \left(\frac{1}{\Delta t} - \frac{D}{\Delta x^2}\right)C_i^{n-1} + \frac{D}{2\Delta x^2}C_{i+1}^{n-1}. \end{aligned} \tag{5.23}$$

The matrix form of the equation is identical to the Equation 5.20 but with different coefficients:

$$\begin{aligned} a_i &= -\frac{D}{2\Delta x^2}, \\ b_i &= \frac{1}{\Delta t} + \frac{D}{\Delta x^2}, \\ c_i &= -\frac{D}{2\Delta x^2}, \\ d_i &= \frac{1}{\Delta t}C_i^{n-1} - a_i C_{i-1}^{n-1} + (a_i + c_i)C_i^{n-1} - c_i C_{i+1}^{n-1}. \end{aligned} \tag{5.24}$$

where $i = 2, 3, \ldots, N-1$ [126].

It is worth noting that the coefficients a_i, b_i, and c_i for the Crank-Nicholson scheme in Equation 5.24 differ from their counterparts in the BTCS scheme (Equation 5.21) by a factor of two, and d_i differs significantly with extra appearances of C^{n-1} terms.

Algorithmically, the BTCS and Crank-Nicholson schemes are quite similar. The Crank-Nicholson scheme is also implicit and unconditionally stable for solving the diffusion equation. Besides, it is not significantly more challenging to implement than the BTCS scheme. While both FTCS and BTCS schemes have a temporal truncation error of $\mathcal{O}(\Delta t)$, the Crank-Nicholson scheme exhibits a second order temporal truncation error, $\mathcal{O}(\Delta t^2)$ [134], indicating a significantly smaller temporal truncation error compared to the BTCS scheme. Therefore, when the time accurate solutions are desired, the Crank-Nicholson scheme becomes more favourable.

To numerically simulate the Zn concentration profiles, we opted for the Crank-Nicholson algorithm due to its unconditional stability and high accuracy when applied to the diffusion equation.

Finite difference methods require a set of boundary conditions. In our case, the boundary conditions were always changing due to the accumulation of the materials on the sample surface. Next section will discuss how the boundary conditions are calculated.

5.2.2 Settiong up the boundary conditions

In the growth direction (the direction opposite to the substrate) the tailing of Zn concentration is modelled based on the hypothesis that Zn (or the precursor DEZn) acts as a surfactant accumulating on the surface layer and gradually continues to incorporate into InP after the Zn source has been shut off. We used a finite difference approach combining diffusion equations and material growth to model the incorporation of dopants to the epi-layer from an accumulated Zn concentration on the surface.

The boundary conditions were calculated by simulating the growth process. We defined four matrices: send matrix (S_n), incorporation matrix (I_n), evaporation matrix (E_n), and accumulation matrix (A_n), to represent the amount of Zn dopant involved in each time step. These matrices are one-dimensional and computed within the same iteration process (except S_n) over time. The same computational domain $0 \leq t \leq t_{\max}$ for the time steps t_n calculated in Equation 5.10 and computed in Listing 5.1 is used for the iteration process. These matrices can be described as follows:

Send matrix (S_n): The same amount of dopant source, S, flows through the reactor in every time step dt during the doping layer growth. The S_n values are equal to zero after the doped layer growth is finished. Thus, S_n can be expressed by the following step function:

$$S_n = \begin{cases} S, & 0 \leq t_n \leq t_{\text{doping}} \\ 0, & t_{\text{doping}} \leq t_n \leq t_{\max} \end{cases}, \tag{5.25}$$

where S is a constant representing the dopant source flow and t_{doping} represents the time step when the doping is finished.

Incorporation matrix (In): Only a fraction of the available dopants is assumed to incorporate into the material, determined by the incorporation constant ci.

Evaporation matrix (En): A proportion of the dopants present in the reactor is assumed to be lost to the vacuum, determined by the evaporation constant ce.

Accumulation Matrix (An): This matrix represents the concentration of dopants that accumulate on the surface, which may subsequently be incorporated into the material or lost to the vacuum. The initial accumulation at $t = 0$ is assumed to be zero, $A_1 = 0$.

These matrices connected with the following relationships;

$$I_n = ci \times (S_n + A_n), \tag{5.26}$$

where ci is the incorporation constant.. It is the ratio of dopants incorporated into the material to all the dopants that were available to be incorporated.

$$E_n = ce \times A_n, \tag{5.27}$$

where ce is the evaporation constant. It is the ratio of dopants lost (desorbed and evaporated) to the vacuum to all dopants that were accumulated on the surface.

$$A_{n+1} = S_n + A_n - I_n - E_n, \tag{5.28}$$

where the accumulation of dopants at the next time step A_{n+1} is calculated from the values of A_n, S_n, I_n, and E_n at the current time step.

Listing 5.2 is the MATLAB code snippet used in the computation of the growth matrices discussed above variables used to simulate the concentration profile depicted in Figure 5.3a.

```
%%%%%%%setting and computing the material growth
dopthickness = 250; %doped layer thickness/nm
diffthickness = 2257;  %total epi thickness/nm
senda = dopthickness/diffthickness/(n_t/t_end);%number of time steps of doped layer
send = calculateSendTime(senda,S,n_t); %send matrix
accum  =ones(1,n_t); %accummulation matrix
incorp = zeros(1,n_t); %incorporation matrix
evap = zeros(1,n_t); %evaporation matrix
c_i = 0.00065; %incorporation constant
c_e = 0.0001; %evaporation constant

%computing the acummulation, incorporation and evaporation matrices
for i = 1:n_t
    incorp(i)= c_i*(send(i) + accum(i));
```

```
    evap(i)= c_e*accum(i);
    accum(1+i) = send(i)+accum(i)-evap(i)-incorp(i);
end
```

LISTING 5.2: MATLAB code snippet for computing the send, incorporation, evaporation and accumulation matrices. The values are the variables used to simulate the concentration profile in Figure 5.3a.

If we come back to the finite difference method, the first boundary condition $C^n_{i=L}$ is zero for all j (no dopant in the material at the maximum depth of interest, $i = L$). The second boundary condition $C^n_{i=0}$ is the dopant concentration incorporated into the material from the surface at each time step. It uses the corresponding values from the incorporation matrix, I, for each n. We calculate C^n_i value from C^{n-1}_i values but shift them by one i-index (except the boundary condition $C^n_{i=0}$ values) to model the growth. Listing 5.3 is the MATLAB code snippet used for calculating the concentration, the second for-loop inside the snippet shows how the boundary conditions are updated.

```
%coefficients for the tridiagonal system
a = (-dc/2/dx^2)*ones(n_x,1);     %subdiagonal a: coefficients of phi(i-1)
c = a;                           %superdiagonal c: coefficients of phi(i+1)
b = (1/dt)*ones(n_x,1)-(a+c);    %diagonal b: coefficient of phi(i)
b(1) = 1; c(1) = 0;              %fix coefficients of boundary nodes
b(end) = 1; a(end) = 0;
[e,f] = tridiagLU(a,b,c);

%Loop over time step
for m=2:n_t

    % Right hand side includes time derivative and CN terms
    d = U(:,m-1)/dt - [0; a(2:end-1).*U(1:end-2,m-1); 0] + [0;
    (a(2:end-1)+c(2:end-1)).*U(2:end-1,m-1); 0] - [0; c(2:end-1).*U(3:end,m-1); 0];
    d(1) = incorp(m); d(end) = 0; % overwrite BC values
    U(:,m) = tridiagLUsolve(d,a,e,f,U(:,m-1)); % solve the system

    %shift the axis and update boundary condions
    for n=0:n_x-2
        U(n_x-n,m) = U(n_x-n-1,m); %shift axis by one index
        U(1,m)=incorp(m);  %update the boundary condition
```

```
    end
end
```

LISTING 5.3: MATLAB code snippet for calculating the concentration value with Crank-Nicholson algorithm. This code is adapted from the code provided in Reference [126]

Varying the model parameters, allowed us to find a set of parameters which agreed with the experimental curves.

Indeed, Figure 5.3 shows that the simulated dopant concentration profile agrees well with the SIMS results. The mismatch between simulated results and SIMS results, which increases as we go further on the forward-diffusion tail, is attributed to the accuracy of SIMS analysis below 10^{16} atoms/cm^3 (which we did not correct for). The calculated/fitted diffusion constant for that sample/simulation is 2x10^{-14} cm^2/s.

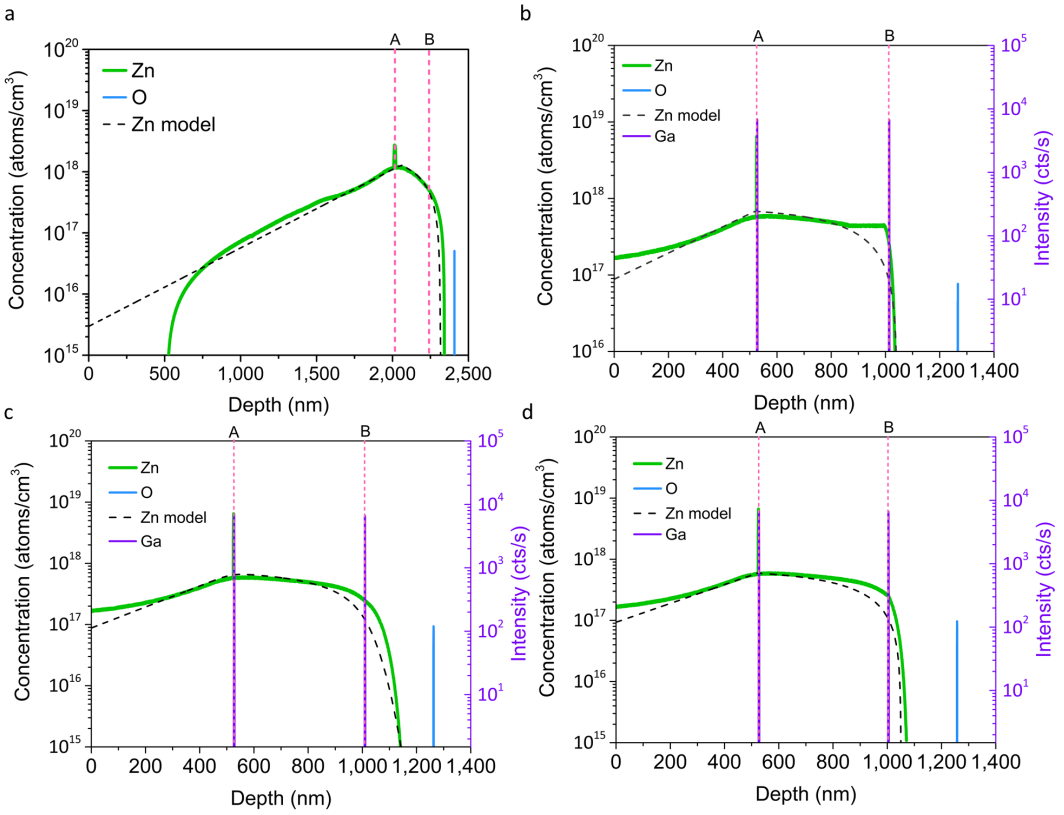


FIGURE 5.3: Modelled Zn concentration profile of InP epitaxial layers compared with measured data. a) Modelling of the measured sample in Figure 4.1a using a single diffusion constant model. The model agrees well with the measured Zn profile. Modelling of Zn profile grown on b) a substrate with 0.4° misoriented towards (111)A crystallographic plane (Figure 4.8a) and c) a substrate with 0.4° misoriented towards (111)B crystallographic plane (Fig 4.8c) by using a single diffusion constant model. d) Modelling of Zn profile grown on nominally perfectly oriented substrate (Fig. 4.8b) by using a double diffusion model with the diffusion constant extracted from (b) and (c).

There are a set of model parameters that give a similar fitting profile with the same diffusion constant (Figure 5.4 and Table 5.1), which limits the quantitative interpretation of our modelling. However, this phenomenology is expected. For example, if we consider our equations related to A_n (Equation 5.28), I_n (Equation 5.26), and E_n (Equation 5.27), it gives the following relationship: $A_{n+1} = S_n(1 - ci) + A_n(1 - ce - ci)$. Thus, when ce and ci much smaller than 1, no major difference can be seen. Despite being a semi-qualitative numerical model, it gives important insights into the surfactant phenomenology.

The diffusion constant in the A direction D_A (Figure 5.3b) and in the B direction D_B (Figure 5.3c) are calculated/fitted to be 1×10^{-16} cm^2/s and 1.2×10^{-13} cm^2/s, respectively. The nominally perfectly oriented sample in Figure 5.3d is modeled using two diffusion constants (See next section).

Case	Sent Concentration	Incorporation constant (ci)	Evaporation constant (ce)
(a)	2.2×10^{18}	1.6×10^{-3}	1×10^{-6}
(b)	2.5×10^{18}	1.5×10^{-3}	1×10^{-5}
(c)	2.2×10^{19}	2×10^{-4}	1.4×10^{-3}
(d)	2.2×10^{20}	2×10^{-5}	1.7×10^{-3}
(e)	2.2×10^{21}	2×10^{-6}	1.7×10^{-3}
(f)	2.2×10^{22}	2×10^{-7}	1.7×10^{-3}

TABLE 5.1: The changed fitting parameters for the sample in Figure 4.1a while dt, dx and dC are kept constant.

5.2.3 Two-diffusion constants

In a nominally perfectly oriented sample, a slight misorientation of any combination of A and B direction can be randomly present across the sample. So, a combination of Fick's second law with two different diffusion constants for the A and B directions can be used to model the perfectly oriented sample with the equation:

$$\frac{\partial c}{\partial t} = D_A \frac{\partial^2 c_A}{\partial x^2} + D_B \frac{\partial^2 c_B}{\partial x^2}, \tag{5.29}$$

where D_A, D_B, c_A, and c_B are respectively the diffusion constant in the A direction, the diffusion constant in the B direction, concentration values for A plane, and concentration values for B plane.

Diffusion constants as derived from our simulations, when misorientation is considered, are remarkably different for A and B directions.

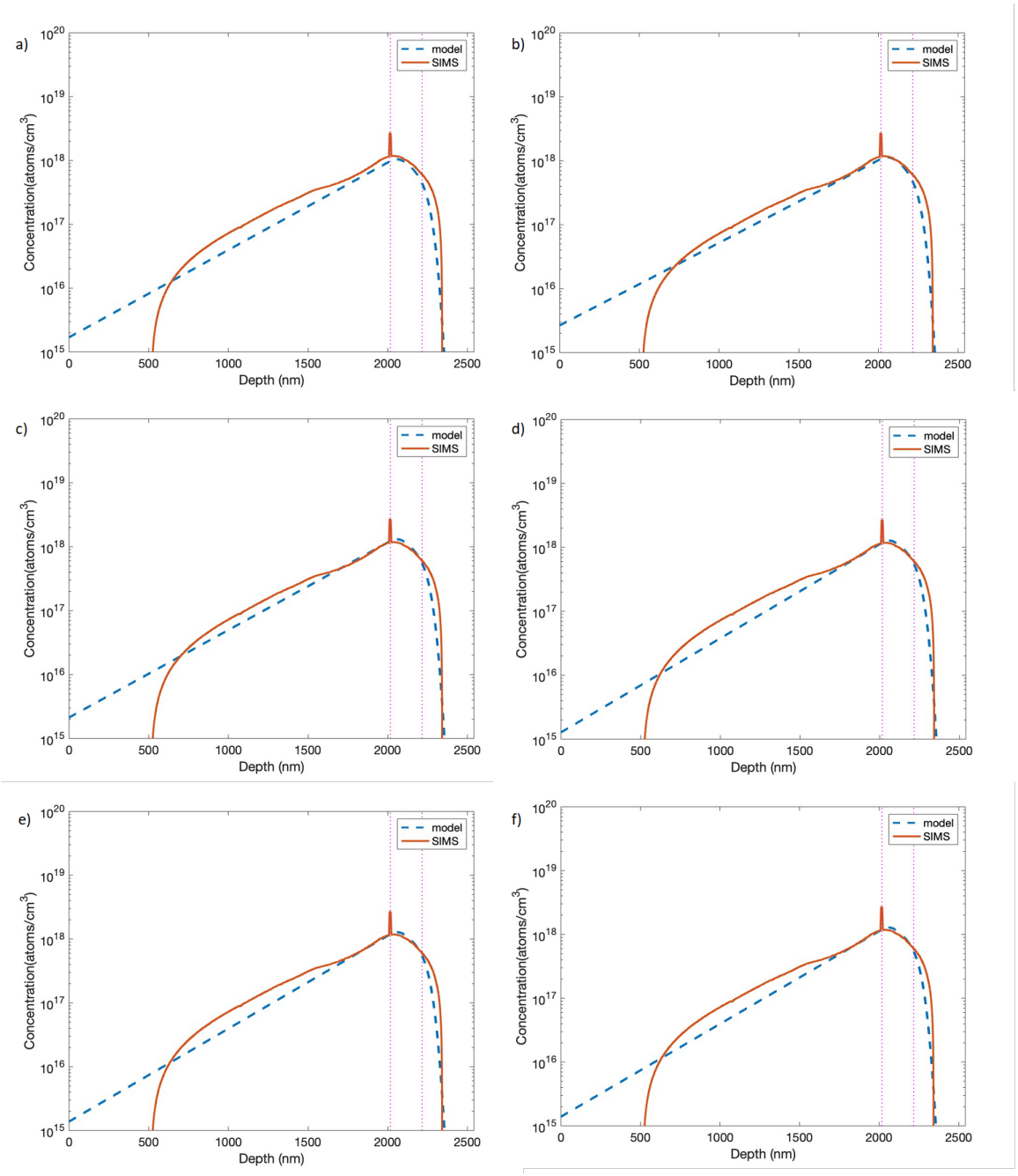


FIGURE 5.4: Simulating the sample in Figure 5.3a by changing the fitting parameters. The details of the changed parameters for a), b), c), d), e) and f) are given in the Supplementary Table 5.1.

The diffusion constants in the A direction (D_A) and in the B direction (D_B), as shown in Figure 5.3b and Figure 5.3c respectively, are calculated as 1×10^{-16} cm^2/s and 1.2×10^{-13} cm^2/s, respectively. The nominally perfectly oriented sample in Figure 5.3d could also be modeled using two diffusion constants (Equation 5.29) and could be fitted equally assuming a specific ad-hoc ratio of the two misorientation components found above.

5.3 Discussion and Conclusion

In this chapter, building upon the comprehensive analysis of the Zn doping concentration profile presented in Chapter 4, we further investigated the surfactant behavior of Zn through a theoretical model and the application of a numerical solution. The coupled equations and the numerical model developed based on the surfactant behavior of Zn dopant, such that dopants accumulate on the sample surface during the doped layer growth and are incorporating to the epi-layer from an accumulated Zn source floating on the sample surface.

For numerical modelling, a Crank-Nicholson algorithm is adapted by combining the material incorporation mechanism with the well-known diffusion equations. We obtained simulation results in a well agreement with the experimental findings.

We also extracted two different diffusion constants from InP samples grown on the 0.4° misoriented substrates in the A and B direction. The diffusion constant for B plane, D_B, is higher than the diffusion constant for A plane, D_A, around 100 times. Using the diffusion constants D_A and D_B we successfully modelled the dopant profile of Zn in InP layers grown on a nominally perfectly oriented substrate.

In general, these findings supports the idea of surfactant behavior, offering some valuable insights into the intricate dynamics of the doping of Zn in InP.

Chapter 6

Suppressing Oxygen Incorporation in Aluminium Containing Alloys

The last two chapters addressed one of the issues that remained unresolved for more than four decades in MOVPE, the long-range "diffusion" of the Zn impurities into the intrinsic layers during (and post) epitaxy. We showed, between other things and with clear and systematic evidence that Zn behaves like a surfactant.

In this chapter, we address (largely as an unintentional "side effect" of previous research) oxygen incorporation during epitaxial growth, particularly in aluminium-containing alloys, which is another long-standing issue, and is also of significant technological interest. This chapter is solely dedicated to the methodology to suppress oxygen incorporation in aluminium-containing alloys. The chapter starts with a brief introduction on the topic, followed by our findings on removing oxygen in AlInAs assisted by Sb, and reducing the oxygen in AlGaAs layers, also presented with some preliminary cross-sectional AFM analysis. With the experimental results we have obtained, we present a baseline study towards understanding the oxygen incorporation pathways and how it is affected with the introduction of Sb.

6.1 Introduction

III-V alloys play a crucial role in various everyday applications and industrial semiconductor devices like lasers , optical modulators, solar cells and high electron mobility transistors, serving

as the primary building blocks of optics and electronics applications [1, 35]. Extrinsic impurities, such as silane, germane, carbon monoxide and dioxide, oxygen, and water, in these alloys are believed to have a detrimental effect on device performances. Chief among these is the oxygen incorporation issue, which is generally addressed in the literature as problematic for device performances, especially in Aluminum containing alloys. This was generally attributed to the high dissociation energy of the bond between oxygen and aluminum [35, 36, 135]. The undesirable presence of oxygen is often associated with the formation of deep-level traps, significantly amplifying the non-radiative recombination rate within the material as a result, and leading to decrease of the photoluminescence and electroluminescence efficiency and deterioration of the carrier mobility [34–36].

Oxygen present in the growth environment (even in the low pressure MOVPE reactors with a partial pressure of at least 10^{-7} Torr coming from the purified carrier gas), residual impurities in the process gases (e.g. AsH_3, H_2, N_2,..) used during growth and impurities in the metal-organic sources in the form of alkoxides (e.g., $Al(CH_3)_2OCH_3$) are attributed as the main sources for oxygen incorporated into the Aluminium alloys [115, 136]. It is worth observing that, in principle (and ignoring growth temperature effects such as re-evaporation), there should be enough oxygen available in any MOVPE rector from these sources to fully oxidize a full monolayer in less than a second. Nevertheless, the observed dopant-like levels of oxygen incorporation (ranging between 10^{17} to 10^{19} atoms/cm^{-3}) in the literature are still only a fraction of what they are expected to be if one considers that a "full" oxidation could deliver densities in the 10^{22} [36–40]. We call this conundrum as the "Oxygen Paradox".

We mention here that another relatively puzzling phenomenon is the short lifetime of AlAs layers, upon exposure to air (oxygen). Indeed, AlAs (100) oxidizes "immediately", lasting only a few seconds [137]. However, this behavior can be improved and largely suppressed by the simple addition of only a small concentration of Ga, even less than 1%, creating an Al rich AlGaAs alloy [138]. While we will not address this last issue here, we hope that the improved understanding that our work could deliver, will help also improving our understanding.

There are number of reports studying the oxygen incorporation the aluminium layers (which is also observed in molecular-beam epitaxy (MBE) systems), with some of proposing theories to explain underlying mechanism behind it. Kakinuma et al. suggested that the observed increase in oxygen content with increasing aluminum concentration in AlGaAs is likely attributed to surface processes that involve the mitigation and trapping of oxygen at aluminum-rich sites,

particularly the -Al–Al- site [36]. Several studies also showed an increase in oxygen concentration by increasing the Al content of AlGaAs [37, 40, 139]. High growth temperatures believed to supress the incorporation of oxygen by increasing probability of its desorption from the surface [35, 40]. In addition, when the V/III ratio is low, more oxygen incorporation is observed [140, 141]. However, little can be found in the literature on the actual details of oxygen incorporation pathways, and on the reason why the MOVPE surface processes somehow actually (and surprisingly) largely suppress oxygen incorporation.

In this study, our primary focus was on reducing/removing the oxygen content in AlInAs and AlGaAs layers by introducing a surfactant, Sb, during their growth. The rationale behind it lies in the surfactant properties of Sb in III-V MOVPE, which are known to alter the surface kinematics and thermodynamics during the growth, also potentially altering the oxygen incorporation pathways. The very first studies came naturally as side products of our Zn work as it can be easily understood.

Indeed, what we observed is a significant influence of Sb on the oxygen content in these materials. In the Sb assisted AlInAs layers, no trace of oxygen is detected, i.e., either there is no oxygen or, better, the oxygen is well below the SIMS detection limit (below $\approx 10^{15}$-10^{16} atoms/cm^{-3}). Furthermore, introducing Sb as surfactant lead to a significant reduction in oxygen levels also within AlGaAs layers, decreasing from $\approx 10^{17}$ to $\approx 10^{16}$ atoms/cm^{-3}. Moreover, cross-sectional AFM images of AlGaAs layers shows a surprisingly different oxidation characteristics over time for between the AlGaAs and AlGaAs:Sb layers grown at 700°C. We underline that the Sb levels detected in the materials analysed were dopant like, and that these results cannot be linked to a simple change in the "alloy" analysed.

6.1.1 Removing Oxygen in AlInAs with Sb

To investigate the effect of Sb usage during AlInAs layer growth, we grew simple test epi-structures by MOVPE. These structures featured AlInAs layers grown with and without Sb. The SIMS results shown in Figure 6.1 has the sample structure as follows: InP substrate, followed by a 200 nm undoped InP buffer layer, 200 nm Zn doped InP layer, a 500 nm AlInAs:Sb layer and 200 nm undoped AlInAs layer. The top 200 nm undoped AlInAs layer is added to observe the difference in oxygen incorporation with AlInAs:Sb layer in the same growth run. We have already discussed Zn part in Chapter 4 (in Figure 4.7). Here, we will only discuss the oxygen part of the story. The samples are grown at 715°C thermocouple temperature with V/III

(AsH_3/(TMIn+TMAl)) ratio of 120. The growth conditions are kept same in both samples, only the sample in Figure 6.1b has much less Sb flow (i.e. the TMSb/TMAl ratio was 0.42) compared to the sample in Figure 1a (i.e. the TMSb/TMAl ratio was 2.34). Also after growing the sample in Figure 6.1a, the flows were minorly corrected for Al and In so that AlInAs layers in the sample in Figure 6.1b is better lattice matched to InP (AlInAs is lattice matched to InP with 48% Al and 52% In).

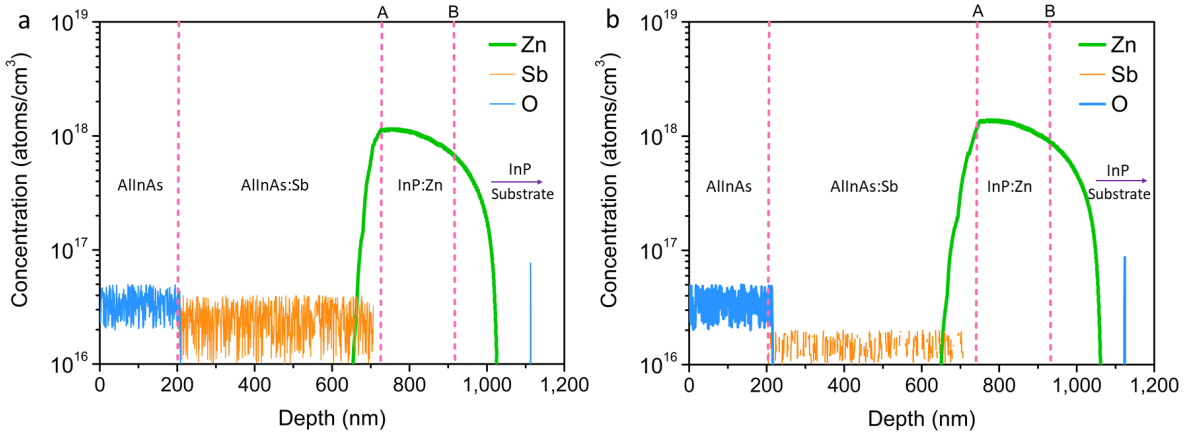


FIGURE 6.1: Effect of Sb addition on the oxygen incorporation of AlInAs layers (same samples showed in Figure 4.7). Sb assisted AlInAs layer is immediately started after the Zn doped InP layer. a) No oxygen trace is recorded in the layers where Sb is present. b) Same structure and growth protocol with sample (a) with lower Sb flow. The oxygen peak marks the sample substrate-to-epitaxial layer interface. The dotted lines indicates the nominal boundaries between the layers.

The oxygen incorporation in AlInAs layers and Sb incorporation in AlInAs:Sb layers are around doping levels. In both samples, oxygen is remarkably not present when TMSb is used, but returns as soon as TMSb has been shut-off.

Figure 6.2 shows the Al and In percentage measured by SIMS for the same samples shown in Figure 6.1. Usually, when growing alloys at the same conditions, we observe a run-to-run reproducibility rate within $\leq$1% variation in composition. However, consistency is expected within the same run for layers employed with the same conditions. Surprisingly, the alloy composition (Al/In ratio) of AlInAs is a bit different for AlInAs and Sb assisted AlInAs layers within the same sample as summarised in Table 6.1. It is important to note that, when the lattice is strained the SIMS calibrations might not be accurate; however, it still offers a qualitative comparison. To compare the Al and In concentration change by Sb, it is best to compare the samples individually as we corrected the flows to be lattice matched in the sample in Figure 6.1b. It is clear that, the introduction of Sb alters the growth dynamics, leading to small compositional variations. In both samples, Al percentage is slightly increased when Sb is used.

AlInAs:Sb				AlInAs		
Sample	**Al%**	**In%**	**Sb (atm/cm^3)**	**Al%**	**In%**	**O (atm/cm^3)**
6.1a	52.3	47.7	2×10^{16}	49.9	50.1	2×10^{16}
6.1b	49.2	50.8	1×10^{16}	48.5	51.5	2×10^{16}

TABLE 6.1: Summary of the Al and In percentage as well as Sb and Oxygen incorporation of the samples in Figure 6.1 (and also Figure 6.2)

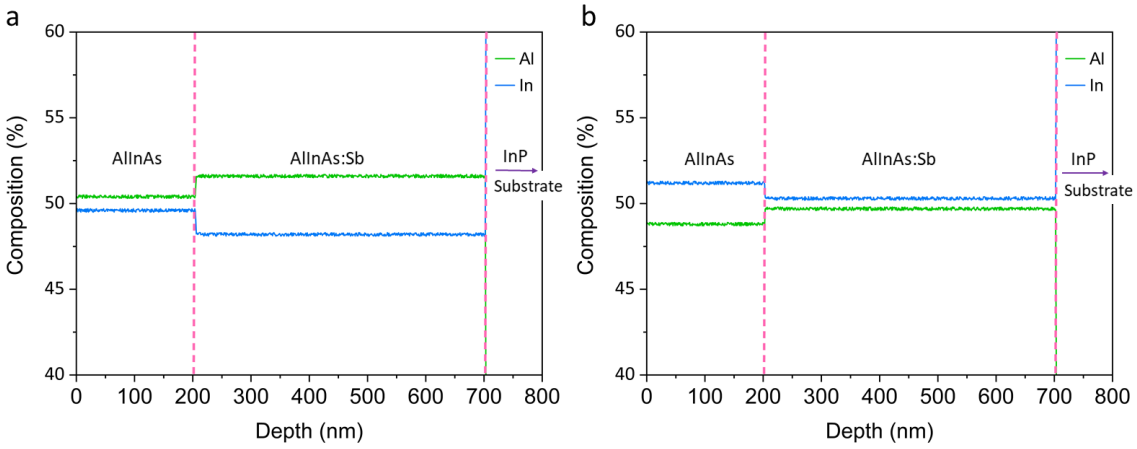


FIGURE 6.2: SIMS analysis showing the Al and In percentage of AlInAs layers of samples a) in Figure 6.1a and b) in Figure 6.1b.

6.1.2 Oxygen Reduction in AlGaAs with Sb

Similarly, simple test structures were grown by MOVPE, to investigate the effect of using Sb on oxygen incorporation within AlGaAs layers. The SIMS results shown in Figure 6.3 have the following sample structure: starting with a GaAs (100) substrate by a 0.2° miscut towards (111)A plane, followed by a 100 nm undoped GaAs buffer layer, 200 nm nominally $Al_{0.5}Ga_{0.5}As$ layer, 5 nm GaAs, 200 nm nominally $Al_{0.5}Ga_{0.5}As$:Sb layer and a 5 nm GaAs de-oxidation cap. The 5 nm GaAs is added between AlGaAs and Sb assisted AlGaAs layers to facilitate SIMS depth profiling. The samples are grown with a V/III (AsH_3/III) ratio of 120 and TMSb/III ratio of 1. The only difference between these two samples was the growth temperature, which was 700° and 750° for samples in Figure 6.3a and Figure 6.3b, respectively.

Table 6.2 provides a summary of the Al and Ga percentages, as well as the oxygen and Sb compositions of the AlGaAs layers corresponding to the sample shown in Figure 6.3. For both samples, the oxygen concentration in the AlGaAs layers is significantly decreased when Sb is used.

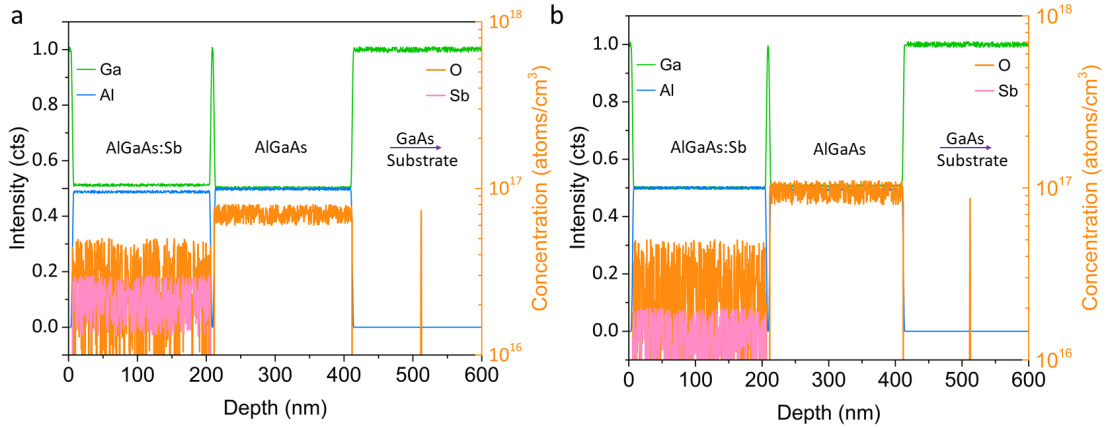


FIGURE 6.3: SIMS depth profiling of AlGaAs:Sb/AlGaAs/GaAs layers. To facilitate the depth profiling a 5 nm GaAs has been grown between AlGaAs and AlGaAs:Sb layers. a) The layers are grown at 700°C thermocouple temperature. b) Same structure grown with same conditions as in (a) expect the temperature was increased to 750°C thermocouple.

It is important to note that a higher oxygen concentration is observed when growth temperature is higher. However, we should not draw a definitive conclusion regarding a temperature-dependent relationship with oxygen concentration based solely on the data from these two samples. Nevertheless, this observation might open the issue if the oxygen incorporation may partly originate from the reactor environment rather than the gallium source (TMGa), but in the lack of clear incorporation pathways dependence on the many parameters involved, e.g. step organization, misorientation and many others, it remains an open issue.

As expected, lower Sb incorporation is observed when the temperature is higher due to the increase on the probability of its desorption from the surface. The introduction of Sb induces minimal changes in the alloy composition. At 700°C, the Al composition is slightly lower in the Sb-assisted layer, while at 750°C, the Al composition shows a slight increase.

	AlGas:Sb				**AlGaAs**		
Sample	**Al%**	**Ga%**	**Sb (atm/cm^3)**	**O (atm/cm^3)**	**Al%**	**Ga%**	**O (atm/cm^3)**
6.3a	48.8	51.2	2.15×10^{16}	2.7×10^{16}	49.8	50.2	7.03×10^{16}
6.3b	50.0	50.0	1.2×10^{16}	2.54×10^{16}	49.3	50.7	9.58×10^{16}

TABLE 6.2: Summary of the Al and Ga percentage as well as Sb and Oxygen incorporation of the samples in Figure 6.3 for comparison.

The AFM images in Figure 6.4a and Figure 6.4b show the surface morphology of the AlGaAs samples grown at 750°C and 700°C, respectively. These images are performed in tapping mode at room temperature in air. The surface organization changes by changing the temperature. A smooth surface morphology characterised by clear step flow structure is observed at the sample grown at 750°C (6.4a). A hillock formation surface structure is observed at the sample grown

at 700°C, which is less desirable 6.4b.

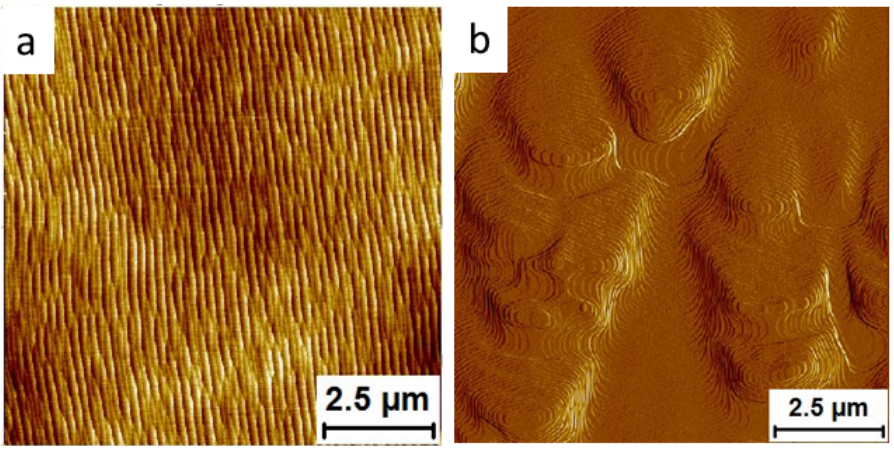


FIGURE 6.4: AFM images showing the surface morphology of samples shown in a) Figure 6.3b, grown at 750°C, showing a step flow surface organization and b) Figure 6.3a, grown at 700°C, showing an hillock formation surface structure.

The oxide growth was investigated on a cleaved [1$\bar{1}$0] facet of AlGaAs/AlGaAs:Sb structures which was grown at 700°C by AFM in peak-force tapping mode at room temperature in air and shown in Figure 6.5. This assessment is achieved by measuring the height of regions by AFM at different times upon cleaving.

The AFM images in Figure 6.5 shows that, after 20 hours, the oxidized AlGaAs layer sits approximately 0.1 nm higher than the neighbouring AlGaAs:Sb layer and approximately 0.5 nm higher than the adjacent GaAs layer/substrate (Figure 6.5). Both the AlGaAs and AlGaAs:Sb layers exhibit remarkably smooth surfaces, with a roughness of around 0.1 nm. However, notable differences in surface appearance are observed between the two layers, especially, 20 hours post-cleaving. Previously, Reinhardt et al. reported on a study investigating the formation of oxide layers over time on $Al_xGa_{1-x}As$ layers (x varying from 0.12 to 0.72) through AFM height measurements. Their findings demonstrated a correlation between the heights of the oxide layers and the Al content within the alloy, that as the Al content increases the oxide formation is higher [139]. However here, the Al compositional change due to Sb is quite low and it is unlikely to cause such a difference. Further investigations is needed to understand the underlying mechanism behind this phenomenology. A possibility, is that the reduced oxidation of the layers grown by Sb assisted epitaxy, actually contain a reduced number of sites for starting the oxidation processes, i.e. a reduced number of lattice defects of sort.

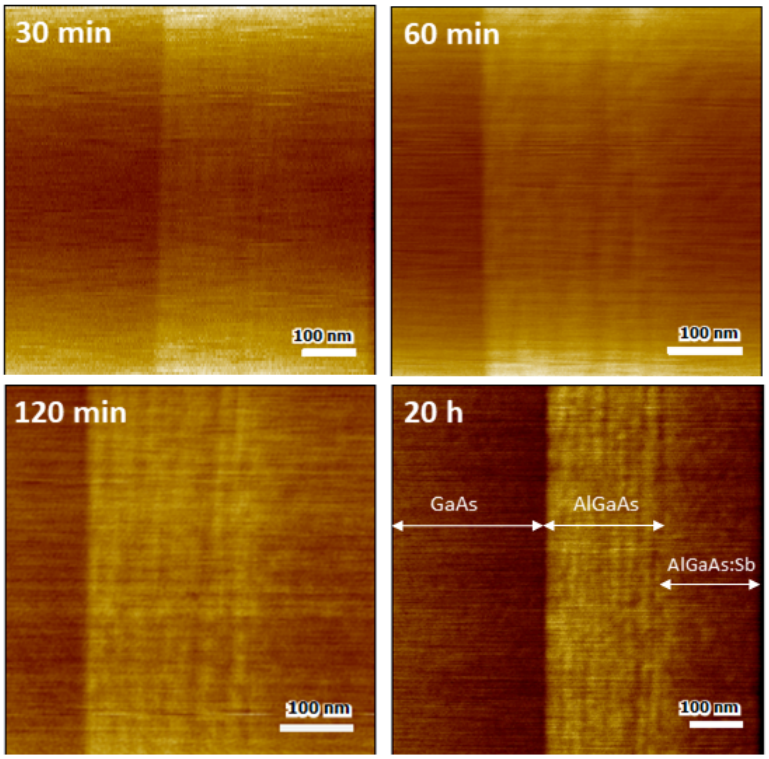


FIGURE 6.5: Cross-sectional AFM images of layers shown in Figure 6.3a. The sample is prepared by cleaving, and AFM probe is scanned over cleavage on $[1\bar{1}0]$ facet perpendicular across the epi-layers in peak-force mode in air at times 30 min, 60 min, 120 min and 20 hours post-cleaving. AlGaAs layers and AlGaAs:Sb layers exhibit different oxidation behaviors; notably, over time, the AlGaAs layer demonstrates a higher height and roughness compared to the AlGaAs:Sb layer.

6.2 Summary and Conclusion

In this chapter, we have shown preliminary investigations of oxygen incorporation and how that changes by using Sb, a surfactant, in III-V MOVPE, in both AlInAs and AlGaAs alloys, which is an issue of substantial technological significance.

We found that the introduction of Sb in AlInAs layers leads to the effective removal of oxygen, either completely or to such low levels that it falls below our SIMS detection limit. Furthermore, we observed a remarkable reduction in oxygen concentration in the AlGaAs layers assisted by Sb.

Overall, employing Sb during the growth of the aluminum-containing alloys can be used as a promising strategy for reducing oxygen content. Additionally, our experimental findings serve as a foundation for exploring the pathways of oxygen incorporation and examining the impact of introducing Sb. Further experiments and theoretical analysis are necessary to have a complete understanding of the subject and its impact on device performance, particularly its potential

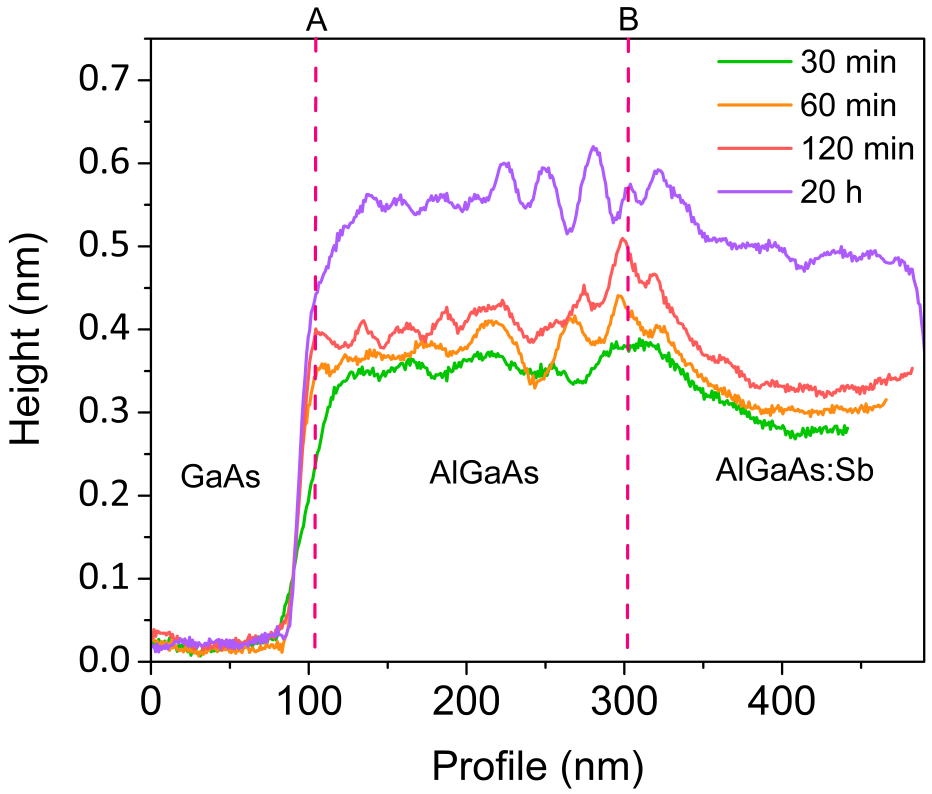


FIGURE 6.6: Height line scans generated from the AFM images in Figure 6.5 at times 30 min, 60 min, 120 min and 20 hours post-cleaving. For each time step, the lines are extracted from averaged lines across the whole image. The dotted lines (A-B) denote the nominal boundaries between GaAs-AlGaAs and AlGaAs:Sb layers. X axes are shifted so that the layers coincide with each other.

in resolving issues associated with oxygen-related problems.

We also observe that our work should be considered the beginning of a broader work aimed at understanding the oxygen paradox. Clearly incorporation pathways for oxygen are a function of multiple variables. Our work has started mapping out those variables, and will continue in the near future, testing for example AlAs behaviour, which in itself seems to be coming with features of its own, and might also be an easier system for ab-initio modelling. It is in general our intention to promote the need for a stronger understanding of these issues, which will necessarily involve a significant ab-initio modelling effort accompanied by more experimental work.

Chapter 7

Conclusion and Future Work

The objective of this thesis work was to tackle two critical technological challenges that have persisted for a very long time: 1) Long-range leakage of Zn and 2) oxygen incorporation in aluminum containing alloys. We accomplished this objective by investigating simple yet novel experimental epi-structures through mainly SIMS, complemented with electrical and theoretical analysis, thereby allowing us for a clear interpretation of the results. A great effort put into this thesis, to obtain a comprehensive insight into the complex physical processes at the atomistic level responsible for the material incorporation. In some parts, there is still work that needs to be done, but overall, the current state is clear and throughout.

7.1 Zn surfactant effects

We reported on Zn surfactant behavior with clear and systematic observations for the first time.

All the samples are epitaxially grown in a MOVPE horizontal reactor at low pressure using N_2 as the carrier gas at 715°C thermocouple.

Zn concentration profiles of MOVPE grown InP structures with a thin Zn doped layer sandwiched between two undoped layers were analyzed by three different SIMS methodology; Zn(Class), Zn(lowV), and Zn(ULIE), all providing different information. To summarize, Zn(Class) utilizes Cs^+ ions for sputtering and $CsZn^+$ detection, offering high-count rates and fast scanning capabilities, although the mechanism behind $CsZn^+$ formation remains not fully understood. Zn(lowV) employs reduced voltages for $CsZn^+$ detection, overcoming potential measurement artifacts associated with the classical approach, while Zn(ULIE) utilizes ultra-low impact energies

to probe the chemical state, specifically targeting the active part of the total Zn incorporated into the material via the ZnP_3 complex ion.

Opposite to the growth direction (back-diffusion), Zn shows a typical diffusion profile aligned with Fick's diffusion laws. However, in the growth direction (forward-diffusion), a Zn dopant concentration greater than 10^{15} atoms/cm^3 was recorded up to a startling ≈1500 nm into the NUD layers (when measured with Zn(lowV)). This observed peculiar asymmetric Zn profile cannot be explained by diffusion alone. Additionally, Zn has a peak concentration of 10^{19} atoms/cm^3 at the interface between the doped and not intentionally doped InP layers; SIMS artefacts were excluded and the feature is reproducible across multiple samples, although we do not have an explanation for it.

For Zn to be electrically active in the lattice, a substitutional incorporation into the III group lattice site is necessary. However, the electrical characterization -such as ECV, C-V and SSRM- results as well SIMS(ULIE) analysis all in a qualitative agreement that, the extended 1500 nm Zn is mostly electrically inactive. In other words, Zn does not incorporate substitutionally in that region and generates either interstitial or point defect structures.

Similar structure with GaAs and InGaAs based layers, again showed an asymmetric dopant profile with no peak at the interface and less profound post-growth tail of around 200 nm. This observation suggest that the surfactant behavior is dependent on the III-V compound, while also confirming that the observed phenomenon is not a reactor memory effect. InGaP based layers, shows a remarkably extended Zn post-growth tailing, similar to that observed in InP. This indicates that the extended post-growth tailing is linked to phosphorus alloys, whereas layers containing arsenic show a reduced effect, albeit still significant.

The observed incorporation profile suggest that either the Zn precursor, whether intact or partially decomposed, or atomic Zn remains present on the epitaxial surface even without the Zn precursor flow. Consequently, this accumulated Zn at the surface is being gradually incorporated into the epitaxial layers, after the Zn flow has been closed. This phenomenon is very similar to findings reported for other surfactant dopants in MOVPE, such as Te and Bi [95, 96]. Furthermore, in a prior publication, Gocalinska et al. demonstrated, without explicitly labelling Zn as a surfactant, that Zn dopants significantly influence the step organization of InP surface structure in MOVPE-grown InP layers by significantly reducing step bunching [63]. This characteristic aligns with the properties commonly associated with surfactants in MOVPE.

We observed that this post-growth tailing can be suppressed and controlled. Implementing a 5-minute growth interruption protocol immediately after the growth of the Zn-doped layer via hydride exposure, PH_3 in that case, significantly reduces the Zn post-growth tailing (up to 250 nm). Additionally, a growth interruption with Sb, another surfactant of MOVPE, and PH_3 successfully mitigate the post-growth tail distance up to ≈120 nm. In other words, the growth interruption is more effective when assisted with Sb, indicating a competition of surfactants over the InP surface which Sb is winning over Zn. This capability of suppressing the excess Zn also indicates that, the different SIMS methodologies for detecting Zn are not one better than another, but simply are sensitive to different Zn species generated during the incorporation processes.

Following these systematic experimental analyses conducted, we modeled Zn surfactant and diffusion processes by combining the material incorporation with diffusion equations, assuming that dopants are incorporating into the epi-layer from an accumulated Zn source floating on the sample surface. For numerical modelling a Crank-Nicholson algorithm is adapted. Our simulations are in a well agreement with the experimental findings.

We observed background diffusion for InP samples grown on the 0.4° misoriented substrates in the A and B directions. The diffusion constants in the A direction, D_A, and in the B direction, D_B, are calculated as 1×10^{-16} cm^2/s and 1.2×10^{-13} cm^2/s, respectively. Using the diffusion constants D_A and D_B, we successfully modeled the dopant profile of Zn in InP layers grown on a nominally perfectly oriented substrate. Additionally, photoluminescence data showed some correlation with sample misorientation.

The things that needs further investigation and some of the potential future research directions are listed below:

- Investigating the origin of the interface peak between NUD and Zn-doped InP. Technically, there should not be any interface between the two layers, since it is just InP on InP. In addition to that, the peak mysteriously disappeared for other material systems, except InGaP.
- The reason for Zn being inactive (and the fact that it is still affecting the laser performance) in the post-growth tailing needs further study. Indeed, in a previous attempt to make an inverted laser, zinc's role was critical. Without a zinc blocking layer, laser emission was absent, and even with it, lasing performance was weak [13].

- In this work, we only examined the back diffusion for 0.4° misoriented substrates in the A and B directions. Further research is needed to investigate the Zn back-diffusion across a range of various misoriented samples.

- An inverted laser with n-on-p architecture needs to be grown and fabricated, with the proposed "growth interruption procedure" to prevent the Zn leakage into the active layers of the device. Our preliminary results represent a huge step forward themselves. However, during the fabrication steps of the device, some other doping diffusion effects might need controlling.

- This thesis is complete and comprehensive in terms of providing clear and systematic evidence on Zn surfactant properties in III-V materials grown by MOVPE. However, in general, an improved theoretical understanding of the surface chemistry pathways to incorporation during MOVPE is necessary.

7.2 Oxygen Incorporation in Aluminum Containing Alloys

This part of the thesis is emerged largely as an unintentional "side-effect" of Zn study, specifically, while experimenting the effect of Sb on Zn post-growth tail in AlInAs layers. In that sense, our results on this study are still preliminary yet promising with some previously unreported results. We showed that oxygen incorporation in Aluminum containing alloys can be efficiently suppressed in MOVPE, in strong similarity to the Zn case.

AlInAs test structures including AlInAs and Sb assisted AlInAs layers were grown and analyzed by SIMS. We observed that the introduction of Sb in AlInAs layers effectively remove oxygen, either entirely or to levels undetectable by SIMS.

Similarly, AlGaAs test structures were grown with AlGaAs and Sb assisted AlGaAs layers. SIMS results on that layers indicate a substantial reduction in oxygen incorporation within the AlGaAs:Sb layers, approximately five times or more. A cross sectional AFM analysis is performed over cleavage on $[1\bar{1}0]$ facet of the AlGaAs/AlGaAs:Sb layers. After 20 hours upon cleaving, the oxidized AlGaAs layer sits approximately 0.1 nm higher than the neighbouring AlGaAs:Sb layer and approximately 0.5 nm higher than the adjacent GaAs layer/substrate.

Future Work

- Overall, more understanding of this issue is needed with strong theoretical modeling accompanied by more experimental work.
- Introducing Sb into other aluminum materials, such as AlAs, will help to understand the phenomenology better, as AlAs is known for its very high oxidation levels.
- The effect of reducing/removing Sb in the aluminum alloys should be tested in some quantum well structures to see whether the phenomenology is improving the optical output.
- Further investigation needs to be done to understand the reason behind the phenomenology observed in the cross-sectional AFM images of the AlGaAs/AlGaAs:Sb layers.

Bibliography

[1] G. B. Stringfellow, *Organometallic vapor-phase epitaxy: theory and practice*. Elsevier, 1999.

[2] M. Razeghi, "The MOCVD challenge: A survey of GaInAsP-InP and GaInAsP-GaAs for photonic and electronic device applications," 2010.

[3] S. N. S. Nakamura, "GaN growth using GaN buffer layer," *Japanese Journal of Applied Physics*, vol. 30, no. 10A, p. L1705, 1991.

[4] S. Arafin and L. A. Coldren, "Advanced InP photonic integrated circuits for communication and sensing," *IEEE Journal of Selected Topics in Quantum Electronics*, vol. 24, no. 1, pp. 1–12, 2017.

[5] S. B. Yoo, "New trends in photonic switching and optical networking architectures for data centers and computing systems," *Journal of Optical Communications and Networking*, vol. 15, no. 8, pp. C288–C298, 2023.

[6] Q. Cheng, M. Glick, and K. Bergman, "Optical interconnection networks for high-performance systems," in *Optical fiber telecommunications VII*, pp. 785–825, Elsevier, 2020.

[7] P. Capper, S. Irvine, and T. Joyce, "Epitaxial crystal growth: methods and materials," *Springer Handbook of Electronic and Photonic Materials*, pp. 1–1, 2017.

[8] H. Kum, D. Lee, W. Kong, H. Kim, Y. Park, Y. Kim, Y. Baek, S.-H. Bae, K. Lee, and J. Kim, "Epitaxial growth and layer-transfer techniques for heterogeneous integration of materials for electronic and photonic devices," *Nature Electronics*, vol. 2, no. 10, pp. 439–450, 2019.

[9] M. Marx, S. Nordmann, J. Knoch, C. Franzen, C. Stampfer, D. Andrzejewski, T. Kümmell, G. Bacher, M. Heuken, H. Kalisch, and A. Vescan, "Large-area MoS_2 deposition via MOVPE," *Journal of Crystal Growth*, vol. 464, pp. 100–104, 2017.

[10] J. Mo, S. El Kazzi, W. Mortelmans, A. N. Mehta, S. Sergeant, Q. Smets, I. Asselberghs, and C. Huyghebaert, "Importance of the substrate's surface evolution during the MOVPE growth of 2D-transition metal dichalcogenides," *Nanotechnology*, vol. 31, no. 12, p. 125604, 2020.

[11] A. Grundmann, C. McAleese, B. R. Conran, A. Pakes, D. Andrzejewski, T. Kümmell, G. Bacher, K. B. K. Teo, M. Heuken, H. Kalisch, and A. Vescan, "MOVPE of large-scale MoS_2/WS_2, WS_2/MoS_2, WS_2/graphene and MoS_2/graphene 2D-2D heterostructures for optoelectronic applications," *MRS Advances*, vol. 5, pp. 1625–1633, 2020.

[12] M. Osiński, J. Furioli, B. Hammons, J. Banas, H. Hou, and K. L. Lear, "Vertical cavity lasers on p-doped substrates," 1997.

[13] S. P. Duggan, H. Yang, N. P. Kelly, L. Caro, M. Dernaika, M. Shayesteh, A. Gocalinska, K. Thomas, E. Pelucchi, B. Corbett, and F. H. Peters, "P-substrate InP-based 1.5 μm lasers using an internal carbon-doped layer to block p-dopant diffusion," *Microwave and Optical Technology Letters*, vol. 60, no. 10, pp. 2363–2367, 2018.

[14] M. Glade, J. Hergeth, D. Grützmacher, K. Masseli, and P. Balk, "Diffusion of Zn acceptors during MOVPE of InP," *Journal of crystal growth*, vol. 108, no. 3-4, pp. 449–454, 1991.

[15] B. Tuck and A. Hooper, "Diffusion profiles of zinc in indium phosphide," *Journal of Physics D: Applied Physics*, vol. 8, no. 15, p. 1806, 1975.

[16] N. Otsuka, M. Kito, M. Ishino, Y. Matsui, and F. Toujou, "Control of double diffusion front unintentionally penetrated from a Zn doped InP layer during metalorganic vapor phase epitaxy," *Journal of applied physics*, vol. 84, no. 8, pp. 4239–4247, 1998.

[17] A. Höglund, C. Castleton, and S. Mirbt, "Diffusion mechanism of Zn in InP and GaP from first principles," *Physical Review B*, vol. 77, no. 11, p. 113201, 2008.

[18] A. Nelson and L. Westbrook, "A study of p-type dopants for InP grown by adduct MOVPE," *Journal of Crystal Growth*, vol. 68, no. 1, pp. 102–110, 1984.

[19] I. Lyubomirsky, V. Lyahovitskaya, and D. Cahen, "Dopant accumulation during

substitutional–interstitial diffusion in semiconductors," *Applied Physics Letters*, vol. 70, no. 5, pp. 613–615, 1997.

[20] D. Liang, G. Roelkens, R. Baets, and J. E. Bowers, "Hybrid integrated platforms for silicon photonics," *Materials*, vol. 3, no. 3, pp. 1782–1802, 2010.

[21] L. Marigo-Lombart, A. Rumeau, C. Viallon, A. Arnoult, S. Calvez, A. Monmayrant, O. Gauthier-Lafaye, R. Rosales, J. A. Lott, H. Thienpont, *et al.*, "High frequency operation of an integrated electro-absorption modulator onto a vertical-cavity surface-emitting laser," *Journal of Physics: Photonics*, vol. 1, no. 2, p. 02LT01, 2019.

[22] S. Kakimoto and H. Watanabe, "Threshold currents of 1.3-μm bulk, 1.55-μm bulk, and 1.55-μm MQW DFB p-substrate partially inverted buried heterostructure laser diodes," *IEEE journal of quantum electronics*, vol. 34, no. 3, pp. 540–547, 1998.

[23] J. J. Plant, P. W. Juodawlkis, R. K. Huang, J. P. Donnelly, L. J. Missaggia, and K. G. Ray, "1.5-μm InGaAsP-InP slab-coupled optical waveguide lasers," *IEEE Photonics Technology Letters*, vol. 17, no. 4, pp. 735–737, 2005.

[24] K. Kurishima, T. Kobayashi, H. Ito, and U. Gösele, "Control of Zn diffusion in InP/InGaAs heterojunction bipolar transistor structures grown by metalorganic vapor phase epitaxy," *Journal of applied physics*, vol. 79, no. 8, pp. 4017–4023, 1996.

[25] N. Otsuka, M. Ishino, and Y. Matsui, "Stability of Zn doping profile in modulation-doped multiple quantum well structure," *Journal of applied physics*, vol. 80, no. 3, pp. 1405–1413, 1996.

[26] S. G. Chu, R. Logan, M. Geva, and N. Ha, "Concentration dependent Zn diffusion in inp during metalorganic vapor phase epitaxy," *Journal of applied physics*, vol. 78, no. 5, pp. 3001–3007, 1995.

[27] Y. Huang, J.-H. Ryou, and R. D. Dupuis, "Control of Zn diffusion in InP/InAlGaAs-based heterojunction bipolar transistors and light emitting transistors," *Journal of crystal growth*, vol. 310, no. 19, pp. 4345–4350, 2008.

[28] K. Kazmierski and B. de Cremoux, "Double zinc diffusion fronts in InP: correlation with models of varying charge transfer during interstitial-substitutional interchange," *Japanese journal of applied physics*, vol. 24, no. 2R, p. 239, 1985.

[29] S. Chu, R. Logan, M. Geva, N. Ha, and R. Karlicek, "Substitutional, interstitial, and neutral zinc incorporation into InP grown by atmospheric pressure metalorganic vapor phase epitaxy," *Journal of applied physics*, vol. 80, no. 6, pp. 3221–3227, 1996.

[30] R. Logan, S. Chu, M. Geva, N. Ha, and C. Thurmond, "Zinc incorporation into InP grown by atmospheric pressure metalorganic vapor phase epitaxy," *Journal of applied physics*, vol. 79, no. 3, pp. 1371–1377, 1996.

[31] S. Chu, R. Logan, and M. Geva, "Zinc incorporation and diffusion in InP during AP-MOCVD growth," *Compound Semiconductor Power Transistors II and: State-of-the-Art Program on Compound Semiconductors (SOTAPOCS XXXII)*, vol. 2000, p. 247, 2000.

[32] C. Blaauw, F. Shepherd, and D. Eger, "Secondary ion mass spectrometry and electrical characterization of Zn diffusion in n-type inp," *Journal of applied physics*, vol. 66, no. 2, pp. 605–610, 1989.

[33] M. C. Silva, J. Zucker, L. Carrion, C. Joyner, and A. Dentai, "Growth optimization for pn junction placement in the integration of heterojunction bipolar transistors and quantum well modulators on inp," *IEEE Journal of selected topics in quantum electronics*, vol. 6, no. 1, pp. 26–30, 2000.

[34] S. Heckelmann, D. Lackner, C. Karcher, F. Dimroth, and A. W. Bett, "Investigations on $al_xga_{1x}as$ solar cells grown by MOVPE," *IEEE Journal of Photovoltaics*, vol. 5, no. 1, pp. 446–453, 2014.

[35] R. K. Willardson, E. R. Weber, G. B. Stringfellow, and M. G. Craford, *High Brightness Light Emitting Diodes*. Academic Press, 1998.

[36] H. Kakinuma, M. M. M. Mohri, and M. A. M. Akiyama, "Characterization of oxygen and carbon in undoped AlGaAs grown by organometallic vapor-phase epitaxy," *Japanese journal of applied physics*, vol. 36, no. 1R, p. 23, 1997.

[37] J. Van Deelen, G. Bauhuis, J. Schermer, and P. Larsen, "Influence of growth parameters on the composition and impurity levels of intrinsically carbon doped AlxGa1 – xAs," *Journal of crystal growth*, vol. 284, no. 1-2, pp. 28–38, 2005.

[38] M. Hata, H. Takata, T. Yako, N. Fukuhara, T. Maeda, and Y. Uemura, "The effects of oxygen impurity in TMA on AlGaAs layers grown by MOVPE," *Journal of crystal growth*, vol. 124, no. 1-4, pp. 427–432, 1992.

[39] K. Tsai, C. Lee, K. Chang, H. Chen, and J. Tsang, "Influence of oxygen on the performance of GaAs/AlGaAs quantum well infrared photodetectors," *Journal of applied physics*, vol. 76, no. 1, pp. 274–277, 1994.

[40] M. Kondo, N. Okada, K. Domen, K. Sugiura, C. Anayama, and T. Tanahashi, "Origin of nonradiative recombination centers in AlGaInP grown by metalorganic vapor phase epitaxy," *Journal of electronic materials*, vol. 23, pp. 355–358, 1994.

[41] H. M. Manasevit, "Single-crystal gallium arsenide on insulating substrates," *Applied Physics Letters*, vol. 12, no. 4, pp. 156–159, 1968.

[42] H. Manasevit and W. I. Simpson, "The use of metal-organics in the preparation of semiconductor materials: I. epitaxial gallium-v compounds," *Journal of the Electrochemical Society*, vol. 116, no. 12, p. 1725, 1969.

[43] H. Manasevit, F. Erdmann, and W. Simpson, "The use of metalorganics in the preparation of semiconductor materials: IV. the nitrides of aluminum and gallium," *Journal of the Electrochemical Society*, vol. 118, no. 11, p. 1864, 1971.

[44] H. Manasevit and W. Simpson, "The use of metalorganics in the preparation of semiconductor materials: V. the formation of In-group V compounds and alloys," *Journal of The Electrochemical Society*, vol. 120, no. 1, p. 135, 1973.

[45] S. Irvine and P. Capper, *Introduction to Metalorganic Vapor Phase Epitaxy*, ch. 1, pp. 1–18. John Wiley Sons, Ltd, 2019.

[46] L. Giling, "Gas flow patterns in horizontal epitaxial reactor cells observed by interference holography," *Journal of The Electrochemical Society*, vol. 129, no. 3, p. 634, 1982.

[47] G. Stringfellow, "Organometallic vapor-phase epitaxial growth of III-V semiconductors," in *Semiconductors and Semimetals*, vol. 22, pp. 209–259, Elsevier, 1985.

[48] L. Sun, G. Yuan, L. Gao, J. Yang, M. Chhowalla, M. H. Gharahcheshmeh, K. K. Gleason, Y. S. Choi, B. H. Hong, and Z. Liu, "Chemical vapour deposition," *Nature Reviews Methods Primers*, vol. 1, no. 1, p. 5, 2021.

[49] T. J. Mountziaris and K. F. Jensen, "Gas-phase and surface reaction mechanisms in MOCVD of GaAs with trimethyl-gallium and arsine," *Journal of The Electrochemical Society*, vol. 138, no. 8, p. 2426, 1991.

[50] G. Stringfellow, "Fundamentals of vapor phase epitaxial growth processes," in *AIP Conference Proceedings*, vol. 916, pp. 48–68, American Institute of Physics, 2007.

[51] E. Pelucchi, S. T. Moroni, V. Dimastrodonato, and D. D. Vvedensky, "Self-ordered nanostructures on patterned substrates: Experiment and theory of metalorganic vapor-phase epitaxy of V-groove quantum wires and pyramidal quantum dots," *Journal of Materials Science: Materials in Electronics*, vol. 29, pp. 952–967, 2018.

[52] U. W. Pohl, *Epitaxy of semiconductors*. Springer, 2020.

[53] C. Kittel, *Introduction to solid state physics*. John Wiley & sons, inc, 2005.

[54] E. F. Schubert, *Doping in III-V semiconductors*. E. Fred Schubert, 2015.

[55] G. Stringfellow, "The role of impurities in III/V semiconductors grown by organometallic vapor phase epitaxy," *Journal of Crystal Growth*, vol. 75, no. 1, pp. 91–100, 1986.

[56] E. Schubert, C. Pinzone, and M. Geva, "Phenomenology of Zn diffusion and incorporation in InP grown by organometallic vapor-phase epitaxy (OMVPE)," *Applied physics letters*, vol. 67, no. 5, pp. 700–702, 1995.

[57] E. Veuhoff, H. Baumeister, J. Rieger, M. Gorgel, and R. Treichler, "Comparison of Zn and Mg incorporation in MOVPE InP/GaInAsP laser structures," *Journal of electronic materials*, vol. 20, pp. 1037–1041, 1991.

[58] M. Razeghi and J. Duchemin, "Growth and characterization of InP using metalorganic chemical vapor deposition at reduced pressure," *Journal of Crystal Growth*, vol. 64, no. 1, pp. 76–82, 1983.

[59] J. J. Yang, R. P. Ruth, and H. M. Manasevit, "Electrical properties of epitaxial indium phosphide films grown by metalorganic chemical vapor deposition," *Journal of Applied Physics*, vol. 52, no. 11, pp. 6729–6734, 1981.

[60] S. Chichibu, M. Kushibe, K. Eguchi, M. Funemizu, and Y. Ohba, "High concentration Zn doping in InP grown by low-pressure metalorganic chemical vapor deposition," *Journal of applied physics*, vol. 68, no. 2, pp. 859–861, 1990.

[61] J. Mahony, P. Mascher, and W. Puff, "On the contribution of vacancy complexes to the saturation of the carrier concentration in zinc doped InP," *Journal of applied physics*, vol. 80, no. 5, pp. 2712–2719, 1996.

[62] C. Castleton and S. Mirbt, "Structure of the [Zn_{In}-V_P] defect complex in Zn-doped InP," *Physical Review B*, vol. 68, no. 8, p. 085203, 2003.

[63] A. Gocalinska, M. Manganaro, E. Pelucchi, and D. Vvedensky, "Surface organization of homoepitaxial InP films grown by metalorganic vapor-phase epitaxy," *Physical Review B*, vol. 86, no. 16, p. 165307, 2012.

[64] M. Ludowise, "Metalorganic chemical vapor deposition of III-V semiconductors," *Journal of Applied Physics*, vol. 58, no. 8, pp. R31–R55, 1985.

[65] J. J. Yang, W. I. Simpson, and L. A. Moudy, "Electrical properties of Zn in metalorganic chemical vapor deposition $Ga_{1-x}Al_xAs$," *Journal of Applied Physics*, vol. 53, no. 1, pp. 771–773, 1982.

[66] J. Crank, *The mathematics of diffusion*. Oxford university press, 1979.

[67] T. Tan, U. Gösele, and S. Yu, "Point defects, diffusion mechanisms, and superlattice disordering in gallium arsenide-based materials," *Critical Reviews in Solid State and Material Sciences*, vol. 17, no. 1, pp. 47–106, 1991.

[68] D. Shaw, "Diffusion in semiconductors," *Springer Handbook of Electronic and Photonic Materials*, pp. 1–1, 2017.

[69] A. Willoughby, "Atomic diffusion in semiconductors," *Reports on Progress in Physics*, vol. 41, no. 10, p. 1665, 1978.

[70] H. Mehrer, *Diffusion in solids: fundamentals, methods, materials, diffusion-controlled processes*, vol. 155. Springer Science & Business Media, 2007.

[71] H. Huntington and F. Seitz, "Mechanism for self-diffusion in metallic copper," *Physical Review*, vol. 61, no. 5-6, p. 315, 1942.

[72] H. B. Huntington, "Self-consistent treatment of the vacancy mechanism for metallic diffusion," *Physical Review*, vol. 61, no. 5-6, p. 325, 1942.

[73] C. Zener, "Ring diffusion in metals," *Acta Crystallographica*, vol. 3, no. 5, pp. 346–354, 1950.

[74] K. C. Pandey, "Diffusion without vacancies or interstitials: a new concerted exchange mechanism," *Physical review letters*, vol. 57, no. 18, p. 2287, 1986.

[75] F. Frank and D. Turnbull, "Mechanism of diffusion of copper in germanium," *Physical Review*, vol. 104, no. 3, p. 617, 1956.

[76] U. Gösele, W. Frank, and A. Seeger, "Mechanism and kinetics of the diffusion of gold in silicon," *Applied physics*, vol. 23, pp. 361–368, 1980.

[77] T. Tan, "Point defects and diffusion in semiconductors," in *Handbook of Solid State Diffusion, Volume 1*, pp. 239–319, Elsevier, 2017.

[78] Y. C. Shin, B. J. Kim, D. H. Kang, Y. M. Kim, and T. G. Kim, "Investigation of Zn diffusion by SIMS and its effects on the performance of AlGaInP-based red lasers," *Semiconductor science and technology*, vol. 21, no. 1, p. 35, 2005.

[79] P. Enquist, J. Hutchby, and T. De Lyon, "Growth and diffusion of abrupt zinc profiles in gallium arsenide and heterojunction bipolar transistor structures grown by organometallic vapor phase epitaxy," *Journal of applied physics*, vol. 63, no. 9, pp. 4485–4493, 1988.

[80] G. Van Gurp, T. Van Dongen, G. Fontijn, J. Jacobs, and D. Tjaden, "Interstitial and substitutional Zn in InP and InGaAsP," *Journal of applied physics*, vol. 65, no. 2, pp. 553–560, 1989.

[81] U. Gösele and F. Morehead, "Diffusion of zinc in gallium arsenide: a new model," *Journal of Applied Physics*, vol. 52, no. 7, pp. 4617–4619, 1981.

[82] G. Baysinger, L. I. Berger, R. Goldberg, H. Kehiaian, K. Kuchitsu, G. Rosenblatt, D. Roth, and D. Zwillinger, "CRC handbook of chemistry and physics," *National Institute of Standards and Technology*, 2015.

[83] T. F. Kuech, "Metal organic vapor phase epitaxy chemical kinetics," in *Handbook of Crystal Growth*, pp. 869–907, Elsevier, 2015.

[84] S. Jun, R. Lee, C. Fetzer, J. Shurtleff, G. Stringfellow, C. Choi, and T.-Y. Seong, "Bi surfactant control of ordering and surface structure in GaInP grown by organometallic vapor phase epitaxy," *Journal of Applied Physics*, vol. 88, no. 7, pp. 4429–4433, 2000.

[85] J. Massies and N. Grandjean, "Surfactant effect on the surface diffusion length in epitaxial growth," *Physical Review B*, vol. 48, no. 11, p. 8502, 1993.

[86] F. D. Newman, M. A. Stan, S. L. Murray, and C. S. Murray, "Tellurium surfactant effects in the growth of lattice mismatched $InAs_xP_{1-x}$ by metal organic vapor-phase epitaxy," *Journal of crystal growth*, vol. 272, no. 1-4, pp. 650–657, 2004.

[87] T. Sato, M. Mitsuhara, R. Iga, S. Kanazawa, and Y. Inoue, "Influence of Sb surfactant on carrier concentration in heavily Zn-doped InGaAs grown by metalorganic vapor phase epitaxy," *Journal of crystal growth*, vol. 315, no. 1, pp. 64–67, 2011.

[88] B. Zvonkov, I. Karpovich, N. Baidus, D. Filatov, S. Morozov, and Y. Y. Gushina, "Surfactant effect of bismuth in the MOVPE growth of the InAs quantum dots on GaAs," *Nanotechnology*, vol. 11, no. 4, p. 221, 2000.

[89] I. Markov, "Kinetics of nucleation in surfactant-mediated epitaxy," *Physical Review B*, vol. 53, no. 7, p. 4148, 1996.

[90] A. Gocalinska, M. Manganaro, and E. Pelucchi, "Suppression of threading defects formation during Sb-assisted metamorphic buffer growth in InAs/InGaAs/InP structure," *Applied Physics Letters*, vol. 100, no. 15, 2012.

[91] M. Copel, M. Reuter, E. Kaxiras, and R. Tromp, "Surfactants in epitaxial growth," *Physical review letters*, vol. 63, no. 6, p. 632, 1989.

[92] J. Shurtleff, S. Jun, and G. Stringfellow, "Surfactant effects on doping of GaAs grown by organometallic vapor phase epitaxy," *Applied Physics Letters*, vol. 78, no. 20, pp. 3038–3040, 2001.

[93] R. Heckingbottom, G. Davies, and K. Prior, "Growth and doping of gallium arsenide using molecular beam epitaxy (MBE): Thermodynamic and kinetic aspects," *Surface Science*, vol. 132, no. 1-3, pp. 375–389, 1983.

[94] S. Lee and G. Stringfellow, "Influence of tellurium doping on step bunching of GaAs (001) vicinal surfaces grown by organometallic vapor phase epitaxy," *Applied physics letters*, vol. 73, no. 12, pp. 1703–1705, 1998.

[95] I. García, I. Rey-Stolle, B. Galiana, and C. Algora, "Analysis of tellurium as n-type dopant in GaInP: Doping, diffusion, memory effect and surfactant properties," *Journal of crystal growth*, vol. 298, pp. 794–799, 2007.

[96] T. Orzali, A. Vert, R. T. Lee, A. Norvilas, G. Huang, J. L. Herman, R. J. Hill, and S. S. P. Rao, "Heavily tellurium doped n-type InGaAs grown by MOCVD on 300 mm Si wafers," *Journal of crystal Growth*, vol. 426, pp. 243–247, 2015.

[97] V. Dimastrodonato, L. Mereni, R. Young, and E. Pelucchi, "AlGaAs/GaAs/AlGaAs quantum wells as a sensitive tool for the movpe reactor environment," *Journal of crystal growth*, vol. 312, no. 21, pp. 3057–3062, 2010.

[98] F. Stevie, *Secondary ion mass spectrometry: applications for depth profiling and surface characterization*. Momentum Press, 2015.

[99] K. Schaepe, H. Jungnickel, T. Heinrich, J. Tentschert, A. Luch, and W. E. Unger, "Secondary ion mass spectrometry," in *Characterization of nanoparticles*, pp. 481–509, Elsevier, 2020.

[100] R. G. Wilson, F. A. Stevie, and C. W. Magee, "Secondary ion mass spectrometry: a practical handbook for depth profiling and bulk impurity analysis," 1989.

[101] M. Gauneau, R. Chaplain, and A. Rupert, "Application of cesium primary beam to the characterization of iii. v semiconductors by SIMS," *Le Journal de Physique Colloques*, vol. 45, no. C2, pp. C2–119, 1984.

[102] A. Adriaens, C. Ferauge, and F. Adams, "Quantification of impurities in brass using secondary ion mass spectrometry: a comparison of matrix effects for CsM+ clusters and M+ ions," *International journal of mass spectrometry and ion processes*, vol. 151, no. 1, pp. 63–68, 1995.

[103] E. W. Thomas and A. Torabi, "SIMS analysis using ejected CsX+ ions," *Nuclear Instruments and Methods in Physics Research Section B: Beam Interactions with Materials and Atoms*, vol. 73, no. 2, pp. 214–220, 1993.

[104] P. P. Michałowski, M. Anayee, T. S. Mathis, S. Kozdra, A. Wójcik, K. Hantanasirisakul, I. Jóźwik, A. Piątkowska, M. Możdżonek, A. Malinowska, R. Diduszko, E. Wierzbicka, and Y. Gogotsi, "Oxycarbide MXenes and MAX phases identification using monoatomic layer-by-layer analysis with ultralow-energy secondary-ion mass spectrometry," *Nature Nanotechnology*, vol. 17, no. 11, pp. 1192–1197, 2022.

[105] P. P. Michałowski, "Probing a chemical state during ultra low impact energy secondary ion mass spectrometry depth profiling," *Journal of Analytical Atomic Spectrometry*, vol. 34, no. 10, pp. 1954–1956, 2019.

[106] A. Wójcik, W. Kolkowski, I. Pasternak, W. Strupiński, S. Kozdra, and P. P. Michałowski, "Electrically active and hydrogen passivated Zn in GaAs/AlGaAs specifically distinguished

during secondary ion mass spectrometry depth profiling," *Journal of Analytical Atomic Spectrometry*, vol. 36, no. 1, pp. 178–184, 2021.

[107] S. M. Sze, *Semiconductor devices: physics and technology*. John wiley & sons, 2008.

[108] D. K. Schroder, *Semiconductor material and device characterization*. John Wiley & Sons, 2015.

[109] P. Blood, "Capacitance-voltage profiling and the characterisation of iii-v semiconductors using electrolyte barriers," *Semiconductor Science and technology*, vol. 1, no. 1, p. 7, 1986.

[110] P. Eyben, D. Degryse, and W. Vandervorst, "On the spatial resolution of scanning spreading resistance microscopy: experimental assessment and electro-mechanical modeling," in *AIP Conference Proceedings*, vol. 788, pp. 264–269, American Institute of Physics, 2005.

[111] P. Eyben, M. Xu, N. Duhayon, T. Clarysse, S. Callewaert, and W. Vandervorst, "Scanning spreading resistance microscopy and spectroscopy for routine and quantitative two-dimensional carrier profiling," *Journal of Vacuum Science & Technology B: Microelectronics and Nanometer Structures Processing, Measurement, and Phenomena*, vol. 20, no. 1, pp. 471–478, 2002.

[112] P. De Wolf, T. Clarysse, and W. Vandervorst, "Quantification of nanospreading resistance profiling data," *Journal of Vacuum Science & Technology B: Microelectronics and Nanometer Structures Processing, Measurement, and Phenomena*, vol. 16, no. 1, pp. 320–326, 1998.

[113] S. N. Magonov and M.-H. Whangbo, *Surface analysis with STM and AFM: experimental and theoretical aspects of image analysis*. John Wiley & Sons, 2008.

[114] B. Voigtländer, *Scanning probe microscopy: Atomic force microscopy and scanning tunneling microscopy*. Springer, 2015.

[115] T. Kuech, D. Wolford, E. Veuhoff, V. Deline, P. Mooney, R. Potemski, and J. Bradley, "Properties of high-purity $Al_xGa_{1-x}As$ grown by the metalorganic vapor-phase-epitaxy technique using methyl precursors," *Journal of applied physics*, vol. 62, no. 2, pp. 632–643, 1987.

[116] H. Döscher, K. Möller, P. Vogt, P. Kleinschmidt, and T. Hannappel, "GaP (100) and InP (100) surface structures in the MOVPE ambient," in *IPRM 2011-23rd International Conference on Indium Phosphide and Related Materials*, pp. 1–4, IEEE, 2011.

[117] K. Raghavachari, Q. Fu, G. Chen, L. Li, C. Li, D. Law, and R. Hicks, "Hydrogen adsorption on the indium-rich indium phosphide (001) surface: A novel way to produce bridging In- H- In bonds," *Journal of the American Chemical Society*, vol. 124, no. 50, pp. 15119–15124, 2002.

[118] I. Pelant and J. Valenta, *Luminescence spectroscopy of semiconductors*. OUP Oxford, 2012.

[119] T. P. Pearsall, "Properties, processing and applications of indium phosphide," 2000.

[120] R. Benzaquen, M. Benzaquen, S. Charbonneau, P. Poole, T. S. Rao, C. Lacelle, A. Roth, and R. Leonelli, "Evidence from electrical transport and photoluminescence spectroscopy of a band of localized deep donors in high-purity n-type InP grown by chemical-beam epitaxy," *Physical Review B*, vol. 50, no. 23, p. 16964, 1994.

[121] R. Benzaquen, S. Charbonneau, R. Leonelli, and A. Roth, "Photoluminescence transient-decay study of the deep-donor bound-exciton-emission band in high-purity InP," *Physical Review B*, vol. 53, no. 7, p. 3627, 1996.

[122] Y. Moon, S. Si, E. Yoon, and S. J. Kim, "Low temperature photoluminescence characteristics of Zn-doped InP grown by metalorganic chemical vapor deposition," *Journal of applied physics*, vol. 83, no. 4, pp. 2261–2265, 1998.

[123] E. Montie and G. Van Gurp, "Photoluminescence of Zn-diffused and annealed InP," *Journal of applied physics*, vol. 66, no. 11, pp. 5549–5553, 1989.

[124] J. Hsu, C. Juang, B. Lee, and G. Chi, "Photoluminescence studies of interstitial Zn in InP due to rapid thermal annealing," *Journal of Vacuum Science & Technology B: Microelectronics and Nanometer Structures Processing, Measurement, and Phenomena*, vol. 12, no. 3, pp. 1416–1418, 1994.

[125] W. A. Strauss, *Partial differential equations: An introduction*. John Wiley & Sons, 2007.

[126] G. W. Recktenwald, "Finite-difference approximations to the heat equation," *Mechanical Engineering*, vol. 10, no. 01, 2004.

[127] J. H. Ferziger, M. Perić, and R. L. Street, *Computational methods for fluid dynamics*. springer, 2019.

[128] J. M. Cooper, *Introduction to partial differential equations with MATLAB*. Springer Science & Business Media, 2012.

[129] J. C. Strikwerda, *Finite difference schemes and partial differential equations*. SIAM, 2004.

[130] W. F. Ames, *Numerical methods for partial differential equations*. Academic press, 2014.

[131] R. J. LeVeque, *Finite difference methods for ordinary and partial differential equations: steady-state and time-dependent problems*. SIAM, 2007.

[132] M. Adak, "Comparison of explicit and implicit finite difference schemes on diffusion equation," in *Mathematical Modeling and Computational Tools: ICACM 2018, Kharagpur, India, November 23–25*, pp. 227–238, Springer, 2020.

[133] K. W. Morton and D. F. Mayers, *Numerical solution of partial differential equations: an introduction*. Cambridge university press, 2005.

[134] H. P. Langtangen, "Truncation error analysis," 2015.

[135] W. G. Breiland, M. E. Coltrin, J. R. Creighton, H. Q. Hou, H. K. Moffat, and J. Y. Tsao, "Organometallic vapor phase epitaxy (OMVPE)," *Materials Science and Engineering: R: Reports*, vol. 24, no. 6, pp. 241–274, 1999.

[136] H. Terao and H. Sunakawa, "Effects of oxygen and water vapour introduction during MOCVD growth of GaAlAs," *Journal of Crystal Growth*, vol. 68, no. 1, pp. 157–162, 1984.

[137] D. L. Huffaker, D. G. Deppe, K. Kumar, and T. Rogers, "Native-oxide defined ring contact for low threshold vertical-cavity lasers," *Applied Physics Letters*, vol. 65, no. 1, pp. 97–99, 1994.

[138] K. D. Choquette, K. Geib, H. Chui, B. Hammons, H. Hou, T. Drummond, and R. Hull, "Selective oxidation of buried AlGaAs versus AlAs layers," *Applied Physics Letters*, vol. 69, no. 10, pp. 1385–1387, 1996.

[139] F. Reinhardt, B. Dwir, and E. Kapon, "Oxidation of GaAs/AlGaAs heterostructures studied by atomic force microscopy in air," *Applied physics letters*, vol. 68, no. 22, pp. 3168–3170, 1996.

[140] T. Kuech, R. Potemski, F. Cardone, and G. Scilla, "Quantitative oxygen measurements in OMVPE $Al_xGa_{1-x}As$ grown by methyl precursors," *Journal of electronic materials*, vol. 21, pp. 341–346, 1992.

[141] M. Kamada, H. Ishikawa, S. Miwa, and G. E. Stillman, "The effects of oxygen on the electronic and optical properties of AlInAs layers lattice-matched to InP substrates grown by atmospheric-pressure metal-organic chemical vapor deposition," *Journal of applied physics*, vol. 73, no. 8, pp. 4004–4008, 1993.